A Thesis Submitted for the Degree of PhD at the University of Warwick

Permanent WRAP URL:
http://wrap.warwick.ac.uk/133344

Topological Models of Swarming

by

Jason Moghal Lewis

Thesis

Submitted to the University of Warwick

for the degree of

Doctor of Philosophy

Centre for Complexity Science

September 2018

Contents

Acknowledgments

I would like to convey my heartfelt thanks to everyone I have met during my time at the University of Warwick and who have helped me complete this journey.

Thank you so much to my supervisor Prof. Matthew Turner for introducing me to the more biological side of physics and the richness of the problems therein, for the many engaging discussions in front of the whiteboard (in which an hour meeting suddenly becomes three!) and for reminding me that its also important to let off some steam from time to time.

I am so grateful to all of Warwick Complexity and MathSys. I could not have hoped for more welcoming place to study, and to the people I have met during my time there who made unbearable days in front of the computer bearable. Also thank you everyone in Warwick Soft Matter for the opportunity to listen to and learn from so many bright minds. And thus, a special thanks to the intersection of those two groups, especially those with whom I share a supervisor, for the countless discussions and coffees/beers.

I would like to dedicate this work to my father, Jeffrey Lewis, who taught me to be curious and think. And I would like to express a lifetime of thanks to my family, especially my mother Nasreen, my sister Shareen, my auntie Parveen, my uncle Mude, and to those no longer here. Thank you for all your support and for your unwavering faith in me.

And my eternal gratitude to my partner in life, Helen. None of this would have been possible without the love and support you have given me every day of the past 5 years. You are my light and I love you.

I would finally like to thank anyone who reads this thesis, especially my examiners Drs. Marco Polin and Rastko Sknepnek for their time and patience.

Declarations

This thesis is submitted to the University of Warwick in support of my application for the degree of Doctor of Philosophy. The content of this thesis is my own work, unless stated otherwise. The work presented was carried out by the author under the supervision of Prof. Matthew Turner at the University of Warwick. No part of the thesis has been submitted for a degree at any other institution. The concept of the model presented in Chapter 3 was conceived in a Master's dissertation by myself at the University of Warwick, as indicated in the text. The ideas presented there have been built on substantially in that chapter of this thesis.

Part of this thesis has been published by the author:

- Jason M Lewis and Matthew S Turner, "Density distributions and depth in flocks", *Journal of Physics D: Applied Physics*, 50(49):4003, 2017.

Abstract

We study the collective behaviour of animal aggregations, swarming, using theoretical models of collective motion. Focusing on bird flocking, we aim to reproduce two main aspects of real world aggregations: cohesion and coalignment. Following the observation that interactions between birds in the flock does not have a characteristic length-scale, we concentrate on topological, metric-free models of collective motion. We propose and analyse three novel models of swarming: two based on topological interactions between particles, which define interacting neighbours based on Voronoi tessellation of the group of particles, and one which uses the visual field of the agent. We explore the problem of cohesion, bounding of topological flocks in free space, by introducing the mechanism of neighbour anticipation. This relies on going towards the inferred future position of an individuals neighbours and results in providing the bounding forces for the group. We also address the issue of unrealistic density distributions in existing metric-free models by introducing a homogeneous, tunable motional bias throughout the swarm. The proposed model produces swarms with density distributions corresponding to empirical data from flocks of Starlings. Furthermore, we show that for a group with a visual information input and individuals moving so as to seek marginal opacity that alignment and group cohesion can be induced without the need for explicit aligning interaction rules between group members. For each of the proposed models a comprehensive analysis of characteristics and behaviour under different parameter sets is performed.

List of Symbols

Symbols

Roman

b	Particle radius	m
f	Bounding function	–
$\underline{r}_i$	Position of particle i	m
t	Time	s
$\underline{u}_i$	Velocity fluctuation of particle i	$\mathrm{m\,s^{-1}}$
$\underline{v}_i$	Velocity of particle i	$\mathrm{m\,s^{-1}}$
v_0	Fixed movement speed of particles	$\mathrm{m\,s^{-1}}$
A	Swarm area	$\mathrm{m^2}$
B_i	Set of neighbours of particle i in a given configuration	–
C	Correlation function	–
G	Binder's cumulant	–
I	Number of particles per solid angle	$\mathrm{sr^{-1}}$
L	Linear swarm size	m
N	Number of particles in system	–
P	Swarm polarisation	–
T	Total number of time steps for simulation	–
T_{eq}	Number of time steps discarded at beginning of simulation	–
$\underline{V}$	Group velocity	$\mathrm{m\,s^{-1}}$
$\mathcal{N}_i$	Number of neighbours of i (i.e. the size of B_i)	–
$\mathcal{R}(\theta)$	Two-dimensional unitary rotation matrix by polar angle θ	–
$\mathcal{V}_i$	Visual field of particle i	–

Greek

γ	Turning angle	rad
δt	Size of discrete time step	t
η	Strength of noise parameter	–
θ	Polar angle $\in [-\pi, \pi)$	rad
κ	Topological depth	–
λ	Strength of motional bias on edge	–
$\underline{\hat{\xi}}$	Randomly oriented unit vector	m
ρ	Density of group (in d dimensions)	$\mathrm{kg\,m}^{-d}$
ρ_{init}	Initial density of group (in d dimensions)	$\mathrm{kg\,m}^{-d}$
τ	Time scale parameter used in interaction rules	t
χ_P	Variance of time-averaged polarisation	–
$\underline{\Delta}$	Neighbour distribution anisotropy direction	m
ΔI	Visual anisotropy	–
Ω	Opacity	–

Chapter 1

Introduction

1.1 Collective animal behaviour

1.1.1 Swarming in nature

The collective behaviour of animal aggregations, known as swarming, can be observed throughout nature across many length scales and taxa. It is an ubiquitous natural phenomena that continues to fascinate and inspire both the scientific community and the general public. Many will have looked to the skies and witnessed the dynamic aerial displays of a large flock of birds[1] observing the group move in unison, fragment and coalesce with remarkable apparent ease and aptitude. Remarkably this complex and highly coordinated behaviour is not thought to arise from centralised control. Rather the system is believed to exhibit self-organisation as the behaviour of each individual combines to produce diverse emergent properties of the whole group that could only arise from the interactions of its many interacting components.

There are many forms of collective behaviour, from the synchronisation of firefly luminescence [10], to the *wall of death* observed in many heavy metal concerts [86]. The work in this thesis concerns primarily socially-motivated swarming such as the flocking of birds [28, 30, 49], fish shoaling [71, 79, 80], mammal herding [25, 37], to insect swarming [11, 69]. As mentioned, human crowds can display this sort of collective trait [29, 41, 42] and loud-music is not always required. A frequently observed example is the formation of lanes in stations and shopping centres [40]. Various systems of collective animal behaviour are presented in figure 1.1. The emergence of global orientational order in groups of moving animals is arguably the most striking consequence of this type of social behaviour [69, 95]. In these systems

---

[1] This is certainly the case near the University of Warwick and the Midlands in general.

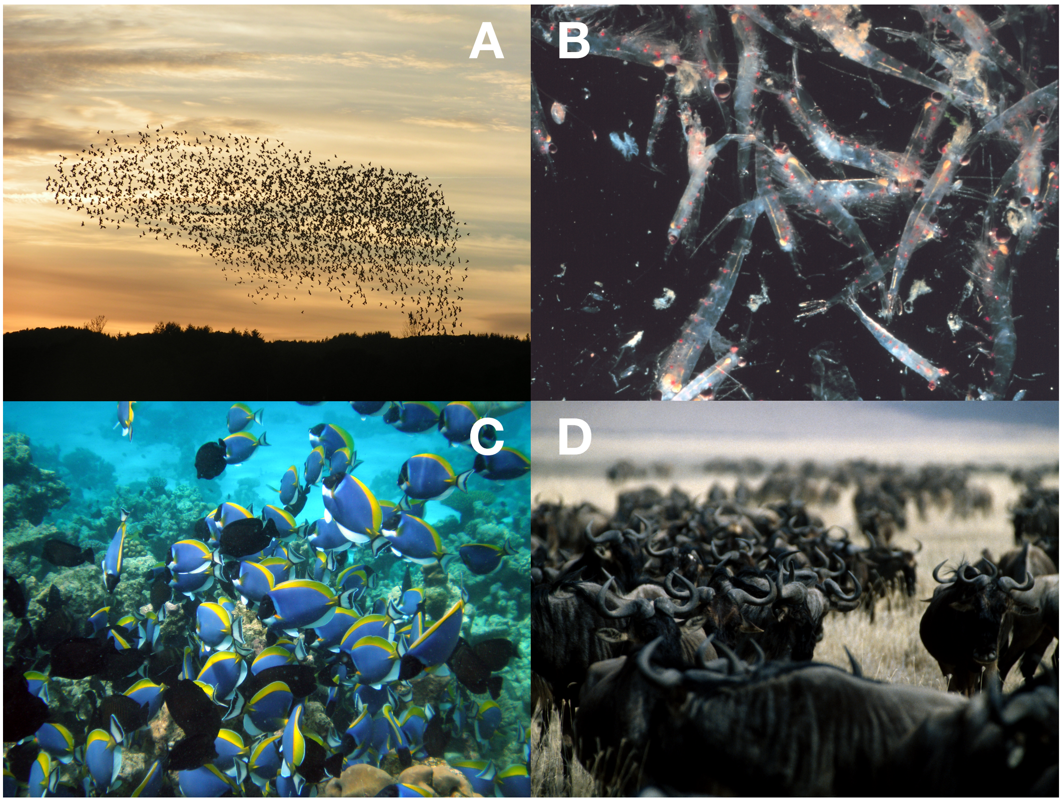

Figure 1.1: Examples of collective animal behaviour. (A) Large murmuration of migrational Starlings near roost at dusk in Denmark. (B) Swarming krill near the Gulf of Farallones in the Pacific Ocean. (C) Shoaling of surgeonfish near Maldives. (D) Herding of wildebeest at the Ngorongoro Crater in Tanzania. Images from Wikimedia Commons [23].

coherent motion is generated by local rules manifesting global order [12, 65].

1.1.2 Motivations for group formation

Often the first question which comes to mind when one observes a large group of animals, particularly if their morphology or dynamics is especially curious, is why it has formed. From a purely myopic perspective, being near others is often a hindrance, as there is increased competition for food and an energetic cost involved with seeking and moving towards an already established group and indeed with orienting oneself with respect to its often dynamic structure. However considering that this behaviour has not only evolved, but has done so in so many natural systems, there must be significant evolutionary advantages associated with being part of a group. It must encourage either propagation of the aggregating species or increased chances of its survival.

Mating

Regarding propagation, from a purely probabilistic perspective it should easier for an individual to find a mate if part of a group. This could certainly encourage aggregating behaviour to evolve as individuals who choose to form groups will benefit from increased numbers over those who do not [94]. Indeed a number of studies identify increased mating activity associated with swarming [26, 107].

Anti-predation

Regarding survival, one could in fact argue that, collecting many individuals together in the same location is counterproductive to the groups chances of survival, as they present a very noticeable target to any nearby predators [71]. Considering that many of the species that swarm the most frequently are prey species, one must conclude that there are benefits to aggregation that outweigh this risk, as well as the aforementioned energetic costs. There are a number of hypothesised anti-predation strategies which could account for this, the ones we cover below are most frequently considered in the literature.

Selfish herd hypothesis This assumes that individuals take action to improve their safety non-altruistically. The safest location for them is therefore in the centre of a group, essentially placing a wall of other group members between themselves and any threats [38]. This could certainly account for the geometry of many two-dimensional groups, with group formation via clustering.

Confusion effect This suggests that individuals can "overload" the capability of a predator to succeed by making it prohibitively difficult to track individuals within the group, and hence reduce the success of any attack [50]. For species in which individuals are small and visually similar, the formation of a dense group with a dynamic outer layer, such as in fish schools and bird flocks, could make this effect very strong [53]. Indeed it has been shown recently via simulation that this effect is sufficient to evolve swarming behaviour [70].

Increased vigilance This identifies an increased response to threat by being in a large group, as information about the environment can be monitored by many group members simultaneously. This is also known as the "many eyes" hypothesis and describes an increased vigilance associated with being part of a group [57, 85]. Considering bird flocks in particular, for which it has been shown that information transfer across the group could be especially fast for highly aligned groups [1, 20].

Encounter dilution Finally, from simple probability considerations, in a larger group the chance of being a target diminishes [85, 100]. This is especially so, for example in a very large flock of Starlings, which individually look very similar to one another (low prey oddity [53]), so an specific individuals risk is distributed across all individuals in the group and therefore becomes very low[2]. This may also reduce the predation by parasites [63].

Energetic

Previously mentioned was the energetic cost of being part of an animal aggregation. This is associated with orienting oneself "correctly" within the group: that is, reacting to a dynamic environment of neighbours and preventing collisions. There are however cases where there is an energetic benefit of being part of a moving group, specifically when in a fluid. A common example includes the "V" shape observed in flocks of geese that is thought to result from individuals orienting themselves behind the tip of the wing of the bird in front in order to catch the up-draft created in the fluid and decrease the energy needed to fly, allowing them to migrate over longer distances [58]. This utilisation of frontal neighbour vortices has recently been shown to also be possible in fish schools [45, 101]. The key factor here is the use of energy dissipating in the medium the group is moving though. Another example is the peloton observed in competitive cycling. Riders can reduce their drag by "slip-streaming" other competitors, even to as little as 5% of the individual drag [9, 81].

Other

Other benefits from aggregation can be increased heat retention [35], such as in penguin huddles [105], and better foraging as a group through, for example, collective hunting [39, 73]. Some species however are just naturally gregarious and become distressed when separated from a group [72].

1.2 Mechanisms of swarming

Having addressed what swarms are and why animals might like to exhibit this sort of behaviour, the next natural question is *how*? This is a difficult question and re-

---

[2] Of course this assumes one hasn't done anything specific to annoy any vengeful predators!

searchers have tried to solve it through two main avenues of investigation: empirical observation and theoretical modelling. In the following work we are concerned with the latter, however both are important to tackle this research question. Theorists bring techniques from a wide variety of disciplines and recent advances in capabilities of numerical modelling, while experimentalists bring the sobering elixir of direct physical observation as well as new techniques to track and reconstruct large groups accurately. We present an overview of these two areas of work relevant to this thesis in the following section.

1.2.1 Biological observations

Many different species have been the attention of empirical study of collective behaviour. Insects can be good choices of model organism as they are easy to manage in a laboratory setting. Locusts in particular have been well-studied, in terms of transition to order [11] and their general swarm behaviour [98, 99]. Interestingly, experiments focussed on confined marching show band formation in the local density profile of a circularly bound swarm, with alignment strongly coupled to this density [5]. Swarms of midges have also been a system of interest. Observations have shown that there are elements of collective motion present in the system, despite midge swarms not having group alignment [2].

Similarly, fish are also extensively studied as they display a wide variety of behaviours. They are also larger than insects and in contrast can form very highly ordered, dense groups. Confining their three free dimensions into an approximately two-dimensional tank can allow for detailed tracking of individual trajectories. This allows, not only for study of group morphology [44], but also investigation of the inter-individual interactions present in such a group [47]. Also aspects such as leadership [51] and consensus formation [104] have also been investigated. Interestingly, the behaviour of predatory fish, with respect to virtual prey, found that collective motion can be produced as a direct effect of the predation [46].

Much of the work in this thesis has however been motivated by a different organism. Starlings are small, gregarious birds with a tendency to flock in scales on the order of a hundred to a hundred thousand individuals. This occurs near their roosting site at dusk and is thought to signal its location to other birds, but also to be a predominantly social behaviour. For very large flocks, the group can become spatially extended vertically above the roost, producing a large columnar structure. They are of particular interest due to recent field study which tracked and reconstructed the three-dimensional trajectories for flocks of up to 2700 birds [4]. This scale of observation had previously never been undertaken and the result allows for sufficient statistics to make good measurements of group properties such as shape, density and overall group dynamics. Flocks of this number of members tended to be planar: spatially extended in two dimensions, parallel to the ground, and thin in the direction of gravity.

A key finding of their study was that individuals only tended to interact with, on average, their 7 nearest neighbours [3]. This finding was particularly surprising as most descriptions of collective behaviour assumed two individuals interact when they are close, say within some fixed radius. This result, determined by inferring the interaction strength via a maximum entropy method [6, 19], suggests that the distance to an individuals neighbours is not important, only that its neighbours are relatively close compared to other flock members. The specific number 7 for nearest neighbours has been suggested to be optimal for robustness of consensus decision making in a noisy environment [106]. In addition, the correlation between fluctuations in velocity was shown to grow with the size of the flock (*scale-free*) suggesting that there is no characteristic length scale for the interaction between individuals, at least in terms of metric-distance. Therefore, it was established that *topological* distance provides the relevant scale for the interaction [3].

This observation forms the basis for this approach taken for the work in this thesis. Topological interactions are important and provide an interesting theoretical challenge due to their inherent lack of a length scale.

1.2.2 Modelling collective motion

While the field of collective motion may be relatively limited in terms of large-scale of groups *in vivo*, it is blessed with a plethora of interesting forms of model for group behaviour. The first model to simulate collective behaviour with a specified reduced ruleset is known as the Boids model [84]. This is based on three individual behaviours: cohesion, co-alignment and collision avoidance. These are realised in that model by effective attraction, alignment with nearby neighbour headings, and repulsion respectively. Even such a simple rule set is able to produce remarkably realistic swarms[3]. As the strength and description of these rules are dependent on the distance between particles, this is termed a *metric-based* model.

Later, Vicsek et al. [103] introduce the study of this type of system from the perspective of statistical mechanics. The model they introduce takes an XY model and allows the particle spins to move off-lattice at fixed speed in the presence of rotational noise, with neighbours identified as all particles within a fixed radius R around each particle (hence also metric-based). They found an order-disorder

---

[3] Remarkable enough to win an Oscar!

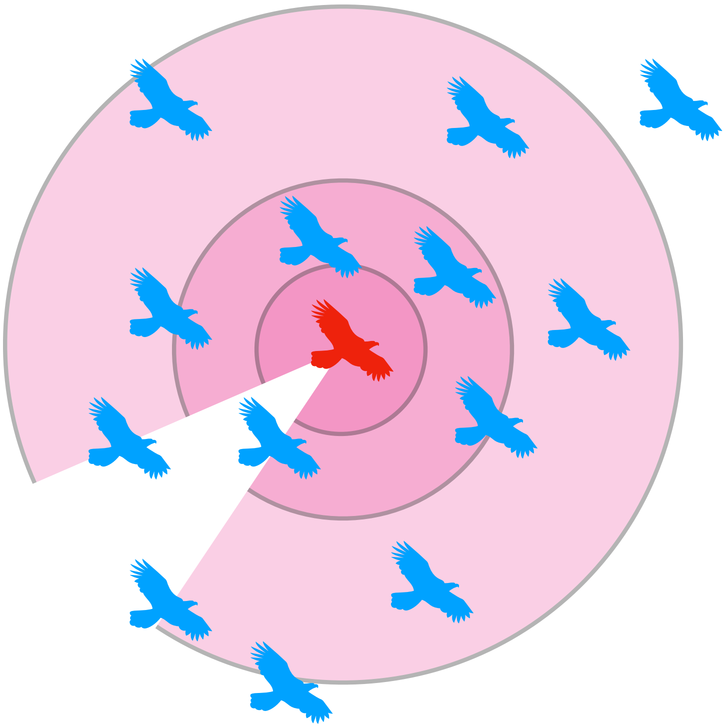

Figure 1.2: Description of interaction based on metric-range, such as in [84]. Red individual interacts with all neighbours (blue) in red concentric zones, via repulsion with innermost region, alignment for the middle, and attraction for the outer region. It would not interact with individuals if they are not in any of these regions, as either they are too far away, or may have passed into the blind region behind it (if such a concept is included in the specific model considered).

transition related to the strength of the noise in the system and analysed it from the perspective of a physicist with a ferromagnetic analogy. This sparked much attention to this field, essentially inviting other physics-based approaches to these types of system. The removal of lattice constraints on the particles makes this system explicitly out-of-equilibrium. We term these self-propelled particles (SPPs) and they are a form of *active matter.* This is characterised by their fixed speed which acts to continually provide energy to the system on the microscopic scale of the interacting particles. Galilean invariance is broken in the system and momentum is not conserved. Therefore, due to the nature of the effective interaction between particle and substrate, and the aligning nature of the inter-particle interaction, we term this *dry, aligning active matter.*

In the context of the empirical observations discussed in the previous section, it would appear that metric-based models would not accurately described collective motion in Starlings. Ginelli and Chaté [34] introduce the topological Vicsek model (TVM) as an extension to the above, where the assignment of neighbours is no longer based on a radius around the particle, but via the Voronoi tessellation [68]. Particles in adjacent Voronoi cells are identified as neighbours and in this way are always connected for aligning interaction. This suppresses fragmentation of the flock and alters the way in which density is coupled to alignment in the system.

Many biological systems have interacting elements which sense their environment through vision. One can also assign interacting neighbours via line of sight: visual interactions [93]. In addition, Pearce et al. [76] introduce a different sort of use for this visual input. They describe a rule that has each individual focus on features in the scene it can observe, comprised of the projected positions of other members in the group. Specifically, other group members occlude regions of an individuals field of view, so one set of features is the edges of those occluded regions. They found that by requiring each individual to head toward the average direction of those edges a swarm can regulate its global density and that the resulting swarms are *marginally opaque.* That is, the projection of the rest of the flock (the occluded regions) covers about half of the visual domain of each individual. They compare this to real flocks and find that they are also in a state of marginal opacity. It is however not known whether this is explicitly sought or obtained by other interactions.

For comparison, figure 1.3 presents a schematic diagram comparing the types of interactions reviewed here.

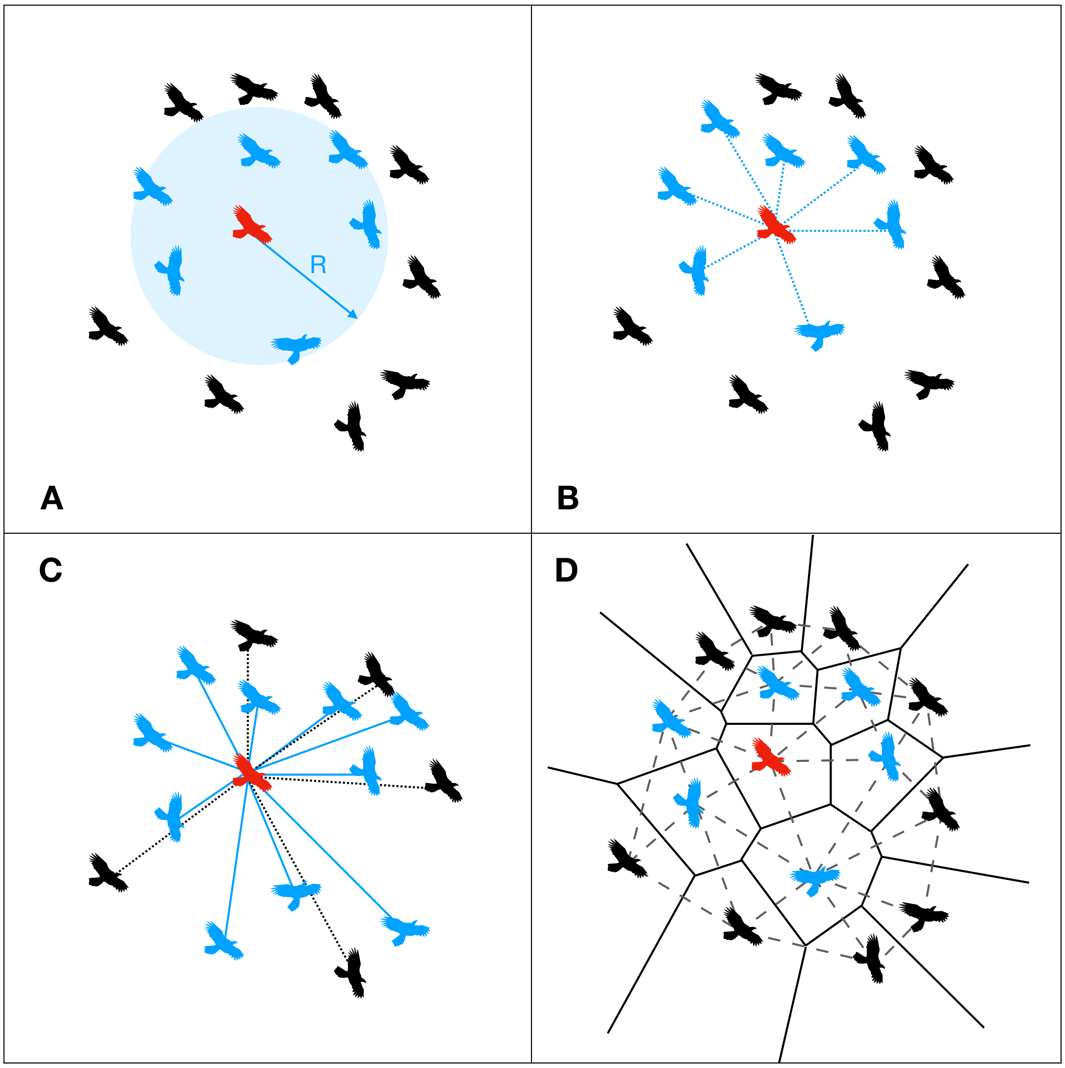

Figure 1.3: Different methods of neighbour identification for red individual. Neighbours in each scheme are blue. (A) Metric-based: interaction with all individuals within radius R. (B) Topological: interaction with nearest n (say 7) neighbours. (C) Visual: interaction with all neighbours that are in line-of-sight; solid lines denoting visible and dotted as occluded (D) Topological: interaction with nearest neighbours as determined via Voronoi tessellation (solid lines denote Voronoi cells; dashed lines denote its dual graph, the Delaunay triangulation).

1.3 Thesis outline

This thesis comprises work on the central theme of describing collective behaviour when the interaction rules between individuals are not local. Chapter 2 introduces a model which considers the well-studied, but physically infeasible, topological Vicsek model introduced above and introduces the concept of neighbour anticipation to naturally bound the group at any density without the need for periodic boundaries. This highlights the benefit of incorporating temporal information into the interaction scheme. Chapter 3 presents a way of controlling the distribution of density across an aggregation in a metric-free fashion. We present a specific way of doing this which reproduces the empirical observation that Starling flocks are more dense on the border than the centre. This goes beyond the question of how to bound a metric-free model in free-space to control its density to investigate global density gradients. We also introduce vision as a method of determining ones depth within a flock. Temporal information and visual input are then combined in Chapter 4 produce alignment and cohesion as emergent properties of the desire of an individual be in a marginally opaque flock. We show how it is possible to generate local correlations between individuals in a group despite there being no explicit local interactions.

Chapter 2

Bound topological swarming in free-space via neighbour anticipation

2.1 Introduction

Two of the most striking aspects of many biological groups are their ability to choose a common direction and remain together during motion despite potentially consisting of thousands of individuals. The former pertains to the groups ability to obtain consensus in velocity (alignment) and the latter in position (cohesion). From a modelling perspective, this identifies two distinct challenges when aiming to reproduce collective behaviour. Group alignment is typically generated through local co-aligning interactions between individuals, whereas group cohesion is commonly attained by specifying periodic boundary conditions to constrain the system.

Recent empirical studies have shown that interactions between group members do not have a characteristic length scale [3, 18]. This has driven interest towards *topological* models of collective behaviour where the interaction radius is replaced by, for example, a fixed number of nearest neighbours or a geometric construction on instantaneous positions. It has been shown that high group alignment can still be achieved in a topological model where each individual aligns with its nearest neighbours as determined by a Voronoi tessellation [34]. However within this *metric-free* paradigm it is not immediately clear if cohesion is supported. The aforementioned study specifically highlights the difficulty in bounding such a model in free space. They describe the dissipation of the group driven by diffusion in the orientation of the swarms constituents, due to the presence of noise (imperfect alignment with neighbours) in the interaction rules. This leads to an inevitable zero density steady-state for the system in the infinite time limit [34].

There are a number of ways to tackle the problem of cohesion in an unbounded topological model. A notable study [75] identifies individuals on the exterior of the group as exclusively aware of their position in the flock and applies a bias to their motion in a metric-free fashion analogously to surface tension. This approach uses the instantaneous state of the system to generate the group bounding. However this is not the only information that is available to the members of the group. Real world flocks are not only moving through space, but obviously also evolve over time. A flock is not just a collection of positions, but a bundle of trajectories (and can be analysed as such [15]).

In this chapter we introduce temporal information into the interaction between individuals in the form of neighbour anticipation. The nature of the co-aligning interaction in most models of collective motion is usually explicit via the aggregation of headings of an individuals neighbours [32]. This is sufficient from a modelling perspective to generate global order of the group. However from a biological perspective, the inter-animal interaction may not be to copy the orientation of their neighbours, but rather to anticipate their trajectory: i.e. not to "point where they are pointing", but to "go where they are going".

The model is defined in § 2.2. The effect of anticipation on group alignment is studied in § 2.3 and the limiting case of a well-studied model of established universality class is also explored. § 2.4 investigates the how the anticipation parameter can be used to control the density of the group and different regions of the model phase space are identified. § 2.5 explores how cohesion is generated as a consequence of varied neighbour distribution and also considers neighbour trajectory determination, before § 2.6 concludes.

2.2 Model outline

We begin by introducing the salient features of the topological Vicsek model [34], then introduce the anticipation interaction as the focus of our model. We then present the final rules which define the motion of particles in our model.

2.2.1 The topological Vicsek model

Classic metric-based models of self propelled particles, such as the Vicsek model [103], determine two particles to be neighbours if they are within some specified distance of one another. The topological Vicsek model [34] instead uses a geometric construction known as the Voronoi tessellation [68] to determine interacting neighbours. At any point in time, particle positions provide a set of points for which to compute this tessellation and particles in neighbouring cells are denoted neighbours. The dual of the Voronoi tessellation, the Delaunay triangulation [54], defines a graph with particles as nodes and neighbours sharing an edge.

This is an attractive choice for topological neighbour assignment as every particle will always be connected, ensuring every individual has others to interact with at all times and suppressing fragmentation of the group structure. Consider, for example, another topological neighbour assignment based on interaction with n nearest neighbours [3], where n is much smaller than the number of members in the group N. It is possible for a model like this to fragment into smaller groups of size $n + 1$, in contrast with the Voronoi tessellation-based method which ensures a single group. This idea can be seen clearly for the simple case of $n = 1$, whereby a pair could leave the group and still suit the neighbour assignment criteria, causing fragmentation of the group as a whole. This idea can be extended to $n = 2$ and fragmenting triads, and so on.

In the topological Vicsek model, particles interact via co-alignment with their Voronoi neighbours in the presence of (vectorial [22]) noise. This has been studied extensively in periodic boundary conditions and was found to exhibit long-range order, supporting a highly ordered phase at low noise strengths, with a continuous transition to disorder as the strength of the noise is increased and the density is kept constant. This is in contrast to an observed discontinuous transition in metric-based models and is directly due to the nature of the interaction. Assigning neighbours topologically decouples alignment from density: particles continually have neighbours to interact with, even if in a region of low density, therefore sparse regions do not induce local disorder. When the periodic boundaries are removed and the swarm initialised in free-space, the swarm diffusively expands indefinitely toward a zero density state. The group centre of mass performs a persistent random walk driven by fluctuations in the group velocity which can be large due to the aforementioned consequences of the topological neighbour assignment. This forms the basis for the neighbour anticipation model presented here.

2.2.2 Neighbour anticipation interaction

We will now derive the interaction rules for this model. A schematic of the proposed anticipation interaction is provided in figure 2.1. Consider a particle i with neighbour j at time t. The position of j moving at velocity $\underline{v}_j(t)$ after time τ has elapsed will

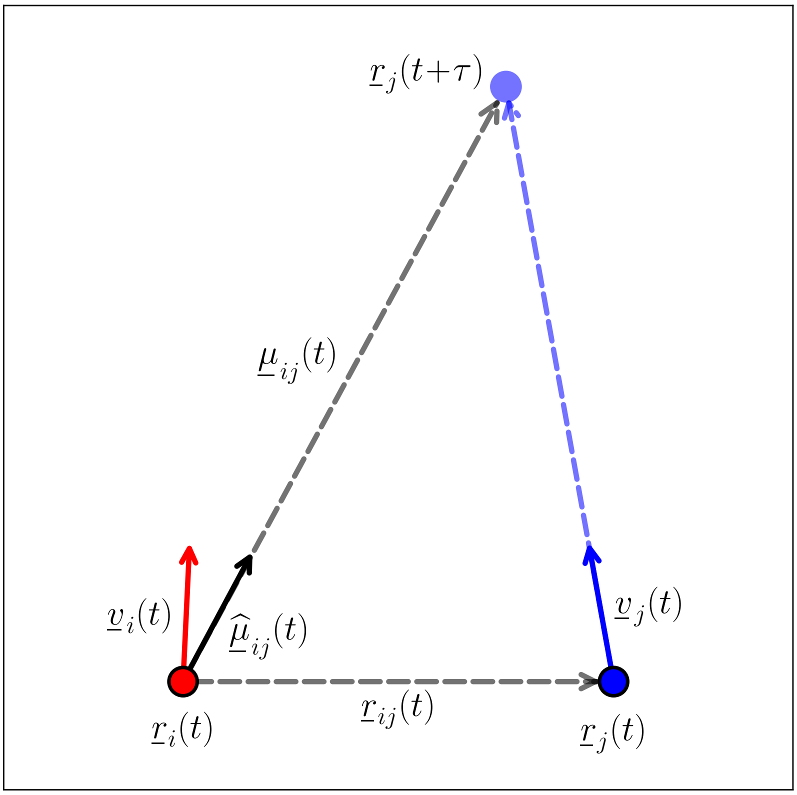

Figure 2.1: Schematic of anticipation interaction between particles i (red) and j (blue) with position $\underline{r}(t)$, velocity $\underline{v}(t)$ and separation $\underline{r}_{ij}(t)$ at time t. To anticipate the motion of particle j to first order, translate position $\underline{r}_j(t)$ by τ time steps in forward time with velocity $\underline{v}_j(t)$ to obtain $\underline{r}_j(t+\tau)$. From the perspective of i, this position lies in the direction $\widehat{\underline{\mu}}_{ij}(t)$: the contribution of j to the change in direction of particle i.

be $\underline{r}_j(t+\tau)$:

$$\underline{r}_j(t+\tau) = \underline{r}_j(t) + \tau \underline{v}_j(t). \tag{2.1}$$

From the perspective of i at $\underline{r}_i(t)$ this is in the direction $\widehat{\underline{\mu}}_{ij}(t)$, where $\widehat{\underline{\cdot}}$ denotes a unit vector. The vector $\underline{\mu}_{ij}(t)$ can be written as:

$$\underline{\mu}_{ij}(t) = \underline{r}_j(t+\tau) - \underline{r}_i(t). \tag{2.2}$$

To fulfil equations 2.1 and 2.2, particle i requires the values of $\underline{r}_i(t)$, $\underline{r}_j(t)$, τ and $\underline{v}_j(t)$. We can safely assume it knows its own position and that of its neighbour. τ is a control parameter which denotes the time scale of the anticipation. In the spirit of using temporal information, rather than using $\underline{v}_j(t)$ directly, we infer it from the trajectory of j. To first order, this is simply:

$$\underline{v}_j(t) \mapsto \underline{v}'_j(t-\delta t) = \frac{\underline{r}_j(t) - \underline{r}_j(t-\delta t)}{\delta t}, \tag{2.3}$$

where δt is the size of the time step. We use a prime ($'$) to distinguish the inferred velocity $\underline{v}'$ from the real (perfectly known) velocity $\underline{v}$. The current and previous time step position of j is used to obtain the simplest estimate of its previous velocity $\underline{v}'_j(t-\delta t)$ which is used in equation 2.1 to determine the position that particle i anticipates j to be at time τ later:

$$\underline{\mu}_{ij}(t) = \underline{r}_{ij}(t) + \tau \underline{v}'_j(t-\delta t), \tag{2.4}$$

where the position of j relative to i at time t is $\underline{r}_{ij}(t) = \underline{r}_j(t) - \underline{r}_i(t)$. Denote B_i as the set of neighbours of particle i at time t. These are the interaction rules which govern the motion of the N identical particles which comprise our system:

$$\underline{v}_i(t+\delta t) = v_0 \vartheta \Big\{ \sum_{j \in B_i} \widehat{\underline{\mu}}_{ij}(t) + \eta \mathcal{N}_i(t) \widehat{\underline{\xi}}_i(t) \Big\}, \tag{2.5}$$

$$\underline{r}_i(t+\delta t) = \underline{r}_i(t) + \delta t \underline{v}_i(t), \tag{2.6}$$

where δt is the size of the discrete time step and v_0 is the fixed speed of the particle. The operator $\vartheta(\ )$ performs normalisation via $\vartheta(\underline{w}) = \underline{w}/|\underline{w}|$. The velocity of particle i is updated as a combination of the sum of this deterministic contribution from each neighbour $j \in B_i$ and a stochastic contribution, as shown in equation 2.5. This stochastic term is comprised of a parameter η that denotes the strength of the noise applied to each particle – an important control parameter in the following, along with the time scale of anticipation τ. This is multiplied by a random unit vector obeying $\langle \underline{\widehat{\xi}}_i(t) \rangle = 0$ and $\langle \underline{\widehat{\xi}}_i(t) \cdot \underline{\widehat{\xi}}_j(t') \rangle = \delta_{i,j}\delta_{t,t'}$ where $\langle \dots \rangle$ represents ensemble average and $\mathcal{N}_i(t)$ the number of neighbours of i at time t (i.e. the size of B_i). Position is updated according to equation 2.6.

It is worth noting that the choice of the factor $\mathcal{N}_i(t)$ in the noise term of equation 2.5 is chosen for historical reasons: the topological Vicsek model (discussed in § 2.2.1) uses this form. Ginelli [33] mentions that perhaps it would be more suitable to use a factor of $\sqrt{\mathcal{N}_i(t)}$ due to the central limit theorem, however we do not use this in what follows, as we hope to keep a useful similarity to the literature (which we discuss further in § 2.3.2).

Furthermore, this choice does not appear to impact on the nature of the order-disorder transition. This is to be expected as $\mathcal{N}_i(t)$ does not vary across individuals or time by a large amount, typically staying close to 6 [61], due to the nature of the Delaunay triangulation. Therefore the difference between the factors $\mathcal{N}_i(t)$ and $\sqrt{\mathcal{N}_i(t)}$ is absorbed into the value of η, as it is also a factor of the noise term. The critical value of η shifts to a higher value for $\sqrt{\mathcal{N}_i(t)})$ than for $\mathcal{N}_i(t)$, as the square-root strictly reduces the magnitude of the noise term, thus a larger value of η is required to disrupt the ordered state. The outcome is that the critical point is different, but the nature of the phase transition is unaffected by this choice.

2.2.3 Experimental setup

The model with interaction rules in equations 2.5 and 2.6 is numerically simulated in two dimensions with an implementation in C++. Delaunay triangulation to assign topological neighbours uses the Computational Geometry Algorithms Library (CGAL) [108]. A system of N particles is initialised uniform randomly across a circle centred on $(0, 0)$ with initial density ρ_{init} and uniformly distributed random orientation. Individuals move in continuous space at a fixed speed v_0 and their state is updated in discrete time steps of δt, which are both set equal to unity in the following. This defines the simulation length scale as $v_0/\delta t = 1$ which is important to note as a reference for measurements of spatial extent. Control parameters are the strength of noise η and the time scale of the anticipation interaction τ. The system evolves for T time steps in total. The first T_{eq} of these are discarded to allow the system to equilibrate and lose the features of its initial condition. To compute swarm statistics the relevant values are averaged over the window $[T_{eq}, T]$ which we denote by $\langle \dots \rangle$ in the following.

2.3 Impact of anticipation on group order

2.3.1 Phase transition

The ability of this collective behaviour model to generate aligned groups is of primary interest. Alignment is quantified in this setting using an analogue with equilibrium models: the order parameter. In this case, the relevant measure of group order is the normalised group velocity, termed the polarisation $P = \left|\frac{1}{v_0 N}\sum_{i=1}^{N} \underline{v}_i(t)\right|$. It has been established in § 2.2.1 that the topological Vicsek model supports a high polarisation state at low noise strength with a transition to a disordered low polarisation state as noise is increased.

In this model with neighbour anticipation we observe a familiar transition from order to disorder with increased noise strength. Figure 2.2 shows the group statistics near this transition for a range of anticipation time scales. For moderate to high values of anticipation τ the group is able to achieve a high polarisation, however when this is decreased far enough the ordered state vanishes.

For a specific anticipation timescale, we are particularly interested in quantifying the value of noise strength that is sufficient to inhibit the formation of an ordered state. This is known as the *critical point* η^* of the system in analogy with equilibrium thermodynamic models [17]. The analogy extends by considering the noise akin to temperature in a ferromagnetic system, as the source of fluctuations to the order. In this analogous system, a quantity known as *susceptibility* χ, which measures the change of magnetisation with temperature T, diverges as we approach the critical temperature T_c [21]. Specifically as $\chi \propto |T - T_c|^{-\gamma}$, where γ is termed the *critical exponent* that quantifies the rate of this divergent behaviour close to the transition point. For a constant temperature the susceptibility is proportional to the variance in the order parameter of the system, defined as $\chi_P = \langle P^2 \rangle - \langle P \rangle^2$. In our simulated system, this will not diverge due to finite-size effects, however we do expect it to grow as we approach the transition point. Figure 2.2 does indeed appear to show maximal values of the variance in order parameter χ_P in our model for large enough values of τ that the ordered phase is present (left and middle columns). At low values of τ this is roughly constant.

Also presented in figure 2.2 is the fourth-order cumulant $G = 1 - \frac{\langle P^4 \rangle}{3\langle P^2 \rangle^2}$ [7] which is suggested to be less sensitive to finite size effects [8]. This can be seen to have values 1/3 and 2/3 in the disordered and ordered phases respectively, as expected [34]. Of particular interest is the value of this across the transition region. At high values of τ it can be seen to vary monotonically from 2/3 to 1/3 with increased noise. This can also be seen in figure 2.3 (left). This suggests a

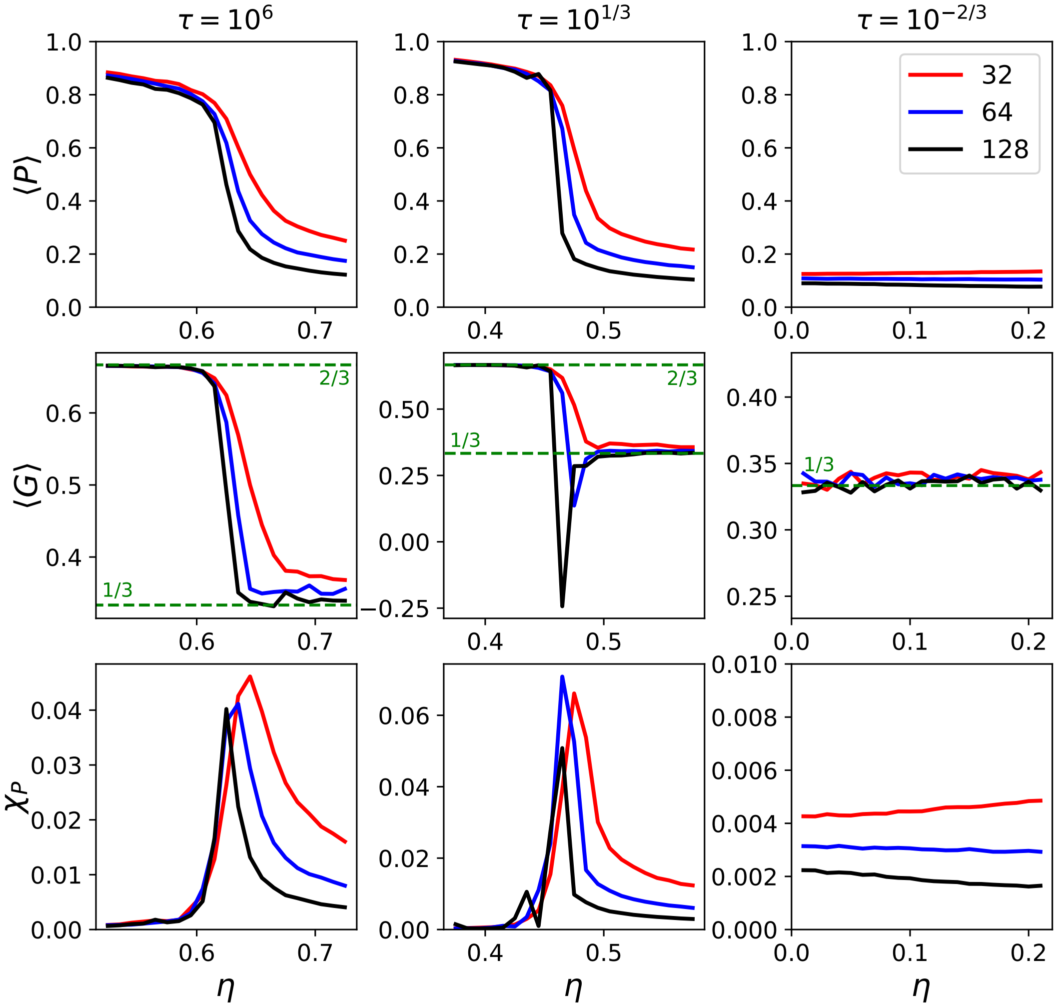

Figure 2.2: Swarm statistics near the order-disorder transition observed in this model using neighbour anticipation. Polarisation $\langle P \rangle$ (top), Binder's cumulant $\langle G \rangle$ (middle) and variance of polarisation χ_P (bottom) for different values of the anticipation parameter τ from high (left, $\tau = 10^6$), medium (middle, $\tau = 10^{1/3}$) to low (right, $\tau = 10^{-2/3}$), for various numbers of particles $N = 32, 64, 128$ (red, blue, black) respectively. Parameter sweep over η performed with resolution 0.01. Statistics are presented as time-averaged values over the window $[T_{eq}, T]$. Simulations performed for $T = 10^5$ time steps total with the first $T_{eq} = 25 \cdot 10^3$ time steps discarded for measurement and are initialised with uniform random orientations and positions in a circle of density 0.1 centred at $(0, 0)$.

continuous phase transition as expected in topological models, as discussed in § 2.2.1. However it is notable that this does not appear to be the case for lower values of τ (middle column). At smaller values of N this does indeed look monotonic, but as N is increased the value of G near the transition becomes negative and dips more sharply as N gets larger. Figure 2.3 (right) also shows how the presence of negative values of G manifests at lower τ values specifically, dipping further as τ is reduced.

A non-monotonic, negative Binder cumulant is the hallmark of a discontinuous transition [34]. However at this point, caution is urged. We will see in § 2.4 that the system is in a fairly dense state at lower values of τ. This may prevent us from easily separating the observation from finite-size effects. Previous studies on similar models of collective motion have seen contention over the nature of the observed transition due to particularly strong finite-size effects present in the system [22, 36]. Discontinuous transitions in these type of systems typically result from a coupling of alignment to local density and we have already established that the topological nature of the interaction precludes a suppression of alignment resulting from sparsity. However in a very dense state, the Delaunay triangulation can change structure very quickly from one time step to the next as it is easy for individuals to change relative positions, especially in a noisy environment. This highly changeable network structure could inhibit the relative local order and affect the nature of the phase transition. In addition, the specific form of the anticipation interaction in equation 2.4 could be the source of this apparent discontinuous transition, as it introduces a term involving the relative distance between individuals. In the low τ dense state the inter-particle distance is small, so the contribution of this term is small too. However as the system transitions to disorder, the high density state becomes significantly sparser. This increases the contribution of the aforementioned term. This interplay between density and interaction could well manifest the discontinuity observed in the phase transition at low values of anticipation time.

2.3.2 Limit of large τ

Consider the equation 2.4 describing the anticipated position of an individuals neighbour after time τ. The direction of this provides the contribution of the neighbour to that individuals new orientation. In the limit where $\tau \to \infty$ this reduces to:

$$\lim_{\tau \to \infty} \underline{\widehat{\mu}}_{ij}(t) = \underline{\widehat{v}}'_j(t - \delta t), \tag{2.7}$$

as the first term in equation 2.4 vanishes in this limit, this is simply the direction of the second term: the estimate of the neighbours previous velocity. This arises from

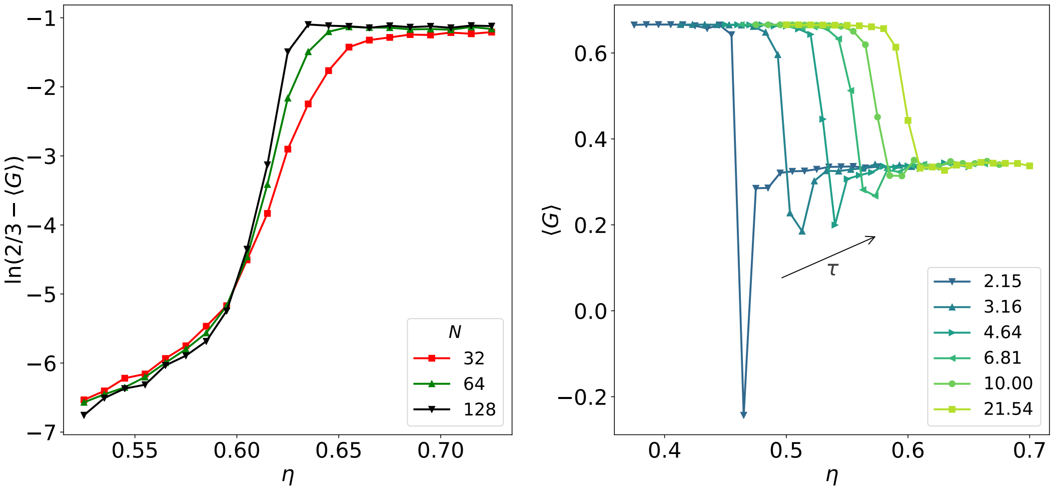

Figure 2.3: Left: Crossing of Binder cumulant curves for different system sizes, $N = 32$ (red), 64 (green) and 128 (black). Time-averaged Binder cumulant $\langle G \rangle$ is transformed as $\ln(\frac{2}{3} - \langle G \rangle)$ to see crossing of curves more closely [34]. High τ $(= 316.2)$ regime. Right: Binder cumulant curves for a range of τ values. The apparent monotonic behaviour of $\langle G \rangle$ across the transition point, as $\langle G \rangle$ goes from 2/3 (ordered) to 1/3 (disordered), at higher values of τ suggests the transition is continuous in this region. However it deepens and even goes negative for lower values of τ suggesting either discontinuity or increasingly strong finite size effects in this region. Simulation parameters as for figure 2.2 for both plots.

our intention to use temporal information to determine the motion of an individuals neighbours from their recent trajectories (and this is the simplest, first order form of that). Let us assume that we can infer the "true" neighbour velocity to good accuracy, i.e. $\underline{v}'_j(t-\delta t) \approx \underline{v}_j(t-\delta t)$. Let us also assume that trajectories are quite smooth, such that a particles velocity does not vary a large amount between single time steps, i.e. $\underline{v}_j(t-\delta t) \approx \underline{v}_j(t)$. One would expect this assumption to hold when the strength of the noise is low and the group is in the ordered regime. This is equivalent to replacing $\widehat{\underline{\mu}}_{ij}(t)$ with $\widehat{\underline{v}}_j(t)$ in equation 2.5, i.e. the topological Vicsek model. We therefore expect that under these conditions we can retrieve its features.

Observations from numerical simulation

Figure 2.4 shows the evolution of long time ($T = 10^7$) simulation for a large anticipation time scale ($\tau = 10^{12}$) and a noise strength ($\eta = 0.61$) close to the critical value for the topological Vicsek model ($\eta^*_{TV} = 0.61661(3)$ [34]). The group reaches an ordered state and expands diffusively in time with a mean distance to topological neighbours (computed as an average over finite edges in the Delaunay triangulation) that grows as $\langle r \rangle \sim \sqrt{t}$.

It is worth noting that the fluctuations in order do not grow with time, as it may appear at first glance of figure 2.4(a). This is merely an artefact of the logarithmic axis in time t. Polarisation P is measured uniformly in linear time from $t = 10$ to $T = 10^7$, but when plotting on the logarithmic axis most of these samples will lie on the right of the graph (at high t). The more samples, the more chance to observe values far from the mean. So while more extreme fluctuations can be found to the right of the graph, this is purely due to the logarithmic transform that places most of the samples in that region. The simulation presented in the figure takes $\mathcal{O}(10^3)$ time steps to equilibrate, then appears stationary until the end of the simulation, $T = 10^7$.

In addition, figure 2.5 shows the trajectory of the centre of mass position for the same simulated swarm. The swarm centre of mass performs a persistent random walk with fluctuations in the group polarisation driving curves in its trajectory. These are fluctuations in the centre of mass velocity and are not coupled with a rotation acting about the centre of mass position, rather this is a translation of a group structure that is relatively fixed with respect to the time scale of the motion. This is further suggested by the linear relationship observed between the mean-squared displacement of centre of mass over time shown in figure 2.5 (inset).

These observations are consistent with the expectation that we should retrieve the topological Vicsek model in the large τ limit. Note that this is not

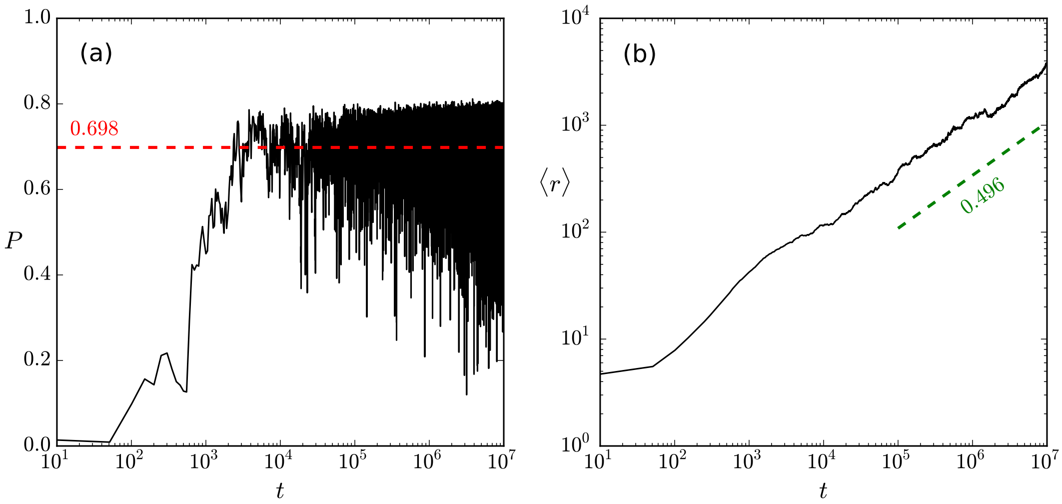

Figure 2.4: Evolution of (a) group polarisation P and (b) mean distance to topological neighbours $\langle r \rangle$ with time t for a system of $N = 2^{10}$ particles interacting with very large anticipation time scale $\tau = 10^{12}$ simulated for $T = 10^7$ time steps. Density initialised at $\rho_{init} = 0.1$. The strength of the noise $\eta = 0.61 \approx \eta^*_{TV}$ the critical point of the topological Vicsek model. At large τ, model should reduce to topological Vicsek. The observed mean polarisation for $t \in [10^6, 10^7]$ of 0.698 (3 s.f.) is consistent with this statement. The slope of (b) for $t \in [10^5, 10^7]$ is close to 1/2 (green dotted line), therefore $\langle r \rangle \sim \sqrt{t}$, displaying a diffusive expansion of the swarm over time while still in an ordered phase.

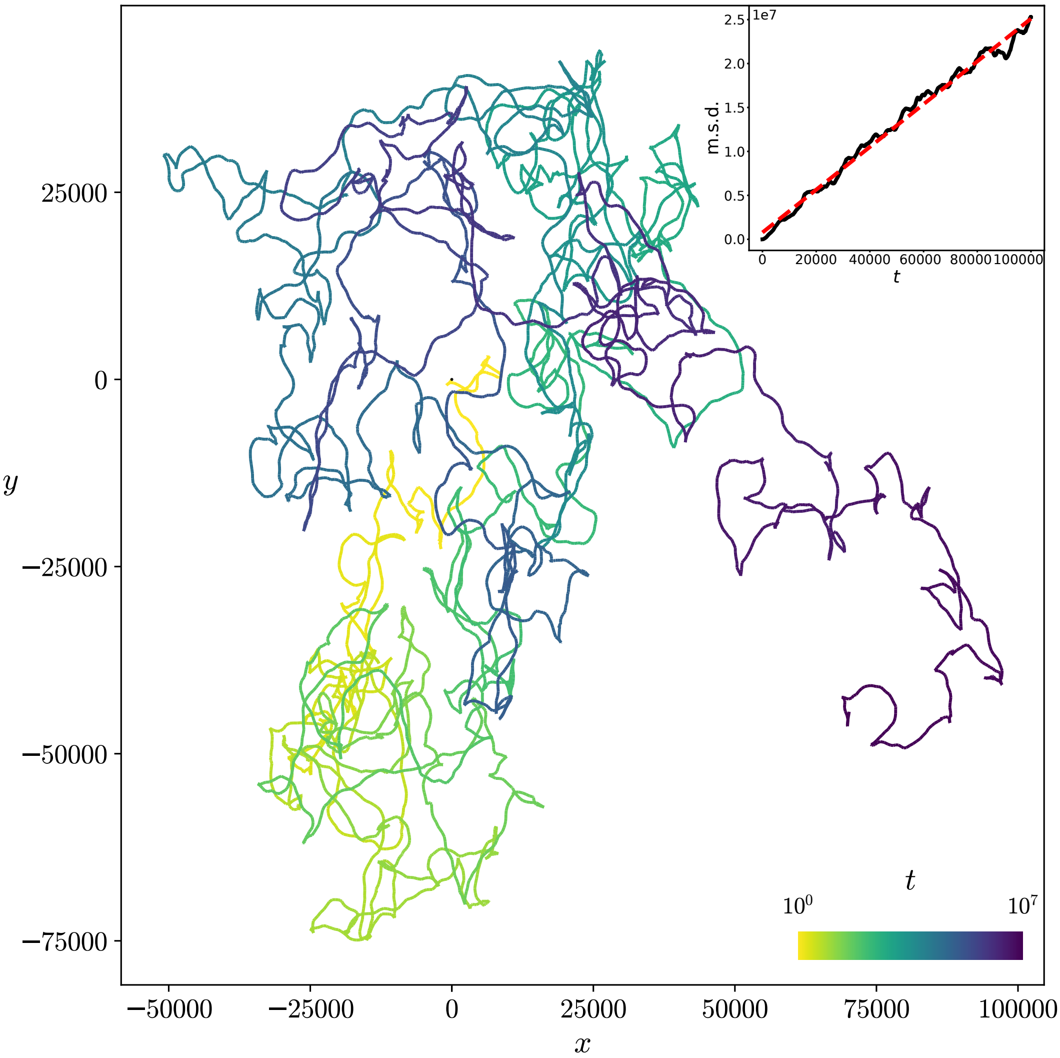

Figure 2.5: Evolution of centre of mass position of swarm near expected critical point in large τ limit. Trajectory structure is driven by fluctuations in the group velocity. Simulated swarm is the same as for figure 2.4: parameters $N = 2^{10}$, $T = 10^7$, $\eta = 0.61$, $\tau = 10^{12}$, $\rho_{init} = 0.1$. Colour denotes age of trajectory: starting yellow at $(0, 0)$ and moving toward purple after 10^7 time steps. Inset: mean-squared displacement (m.s.d.) over time, averaged over 60 simulations with parameters $N = 64$, $T = 10^5$, $\eta = 0.61$, $\tau = 10^8$, $\rho_{init} = 0.1$. Red line is linear fit with $R^2 = 0.991$ (3 s.f.).

necessarily the case as we are not using current neighbour velocities by using their value as inferred from their recent trajectory. This suggests that the aforementioned assumptions hold well. It appears that velocity can be obtained from trajectory even when noise is quite high, as above. This will be explored more directly in § 2.5.2.

The confirmation that the topological Vicsek model is retrieved in a limit of our model is beneficial as the previous study [34] looked very closely at its properties, albeit largely whilst confined by periodic boundaries. In particular they perform a finite-size-scaling analysis to obtain its critical exponents and thereby describe the system by its universality class [67]. Interestingly they find that it does not correspond to any of the known universality classes. Additionally, later work by Peshkov et al. [77] has developed this class of model as a continuous theory via a kinetic Boltzmann-Ginzburg-Landau approach [78]. Choosing a model formulation with a well-studied limit such as this could potentially allow us to expand our analysis with a continuous approach in the future.

Dependence of critical point on τ

In § 2.3.1 it is established that there is a relationship between the anticipation parameter and the strength of noise required to disrupt the ordered state. In this section we quantify the dependence of this critical point η^* on the anticipation time scale τ. As discussed, figure 2.2 shows that the variance of order parameter χ_P will peak in the transition region.

For a given value of τ we perform simulations near the transition region, if it is present, in order to map out the location of the expected peak. A Gaussian is then fitted to this region to estimate the peak location, determined as its mean with uncertainty estimated as its standard deviation. A selection of examples of this process are shown in figure 2.6, where the peak locations have been rescaled according to $\epsilon = 1 - \frac{\eta}{\eta^*(\tau)}$ with critical value $\eta^*(\tau)$. The choice of a Gaussian may appear somewhat arbitrary, however produces a good fit (R^2 close to 1). For the task of determining a peak in the data it certainly appears sufficient, aided by the apparently close to symmetric form of the peaks.

Figure 2.7 shows the impact of varying τ on the location of $\eta^*(\tau)$. As expected, at large values of τ it converges, specifically to $\eta^*(\tau = 10^8) = 0.618 \pm 0.002$. This is close to $\eta^*_{TV} = 0.61661(3)$ reported by Ginelli and Chaté [34]. This agrees within the uncertainty of our measurement, which we obtain as the standard deviation of the Gaussian fit shown in figure 2.6 for $\tau = 10^8$ (blue left-arrow). A difference is expected as the simulation uses a finite N $(= 2^{10})$ whereas η^*_{TV} is computed considering asymptotic scaling [34]. The approach to this value from above

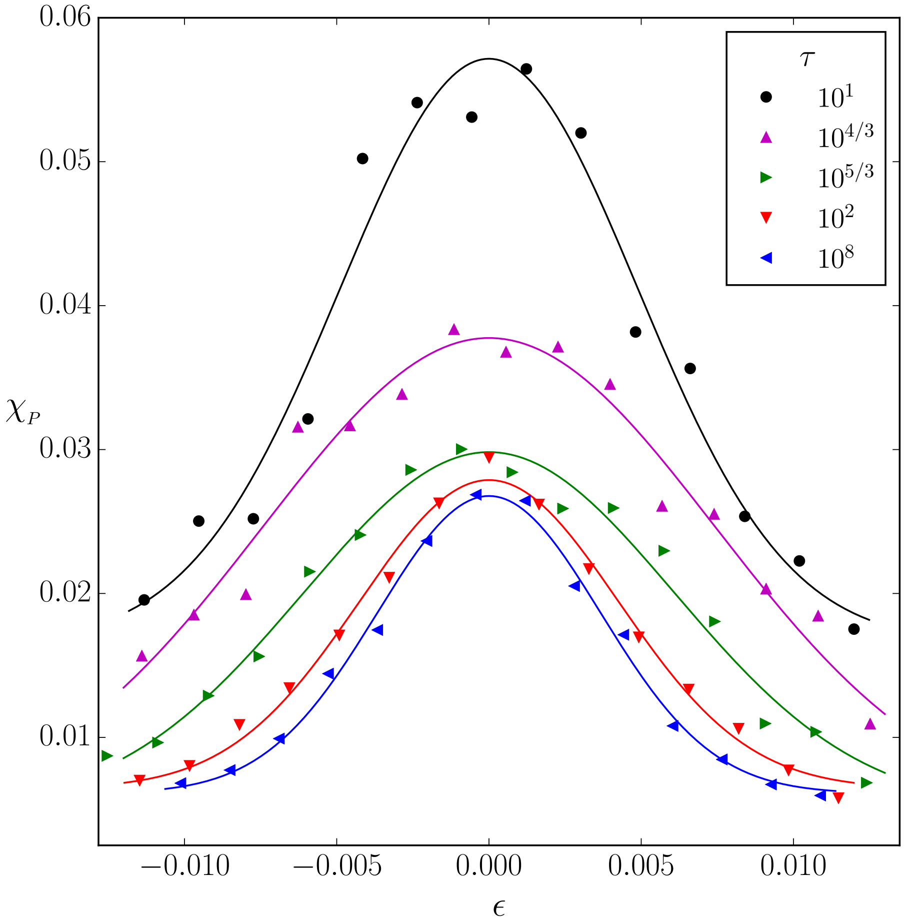

Figure 2.6: Critical points identified via peak in variance of group polarisation χ_P for various values of anticipation time scale τ in terms of rescaled noise strength $\epsilon = 1 - \frac{\eta}{\eta^*(\tau)}$ where $\eta^*(t)$ is the critical value of noise for a given τ. Simulations performed for $N = 2^{10}$ particles for $T = 2.5 \cdot 10^5$ time steps with $T_{eq} = 0.5 \cdot 10^5$ discarded and initial density $\rho_{init} = 0.1$. Anticipation time scale $\tau = \{10^1, 10^{4/3}, 10^{5/3}, 10^2, 10^8\}$ (black circle, magenta up-arrow, green right-arrow, red down-arrow and blue left-arrow respectively). Associated lines are Gaussian fits used to determine $\eta^*(\tau)$ with $R^2 = \{0.963, 0.979, 0.983, 0.990, 0.992\}$ respectively.

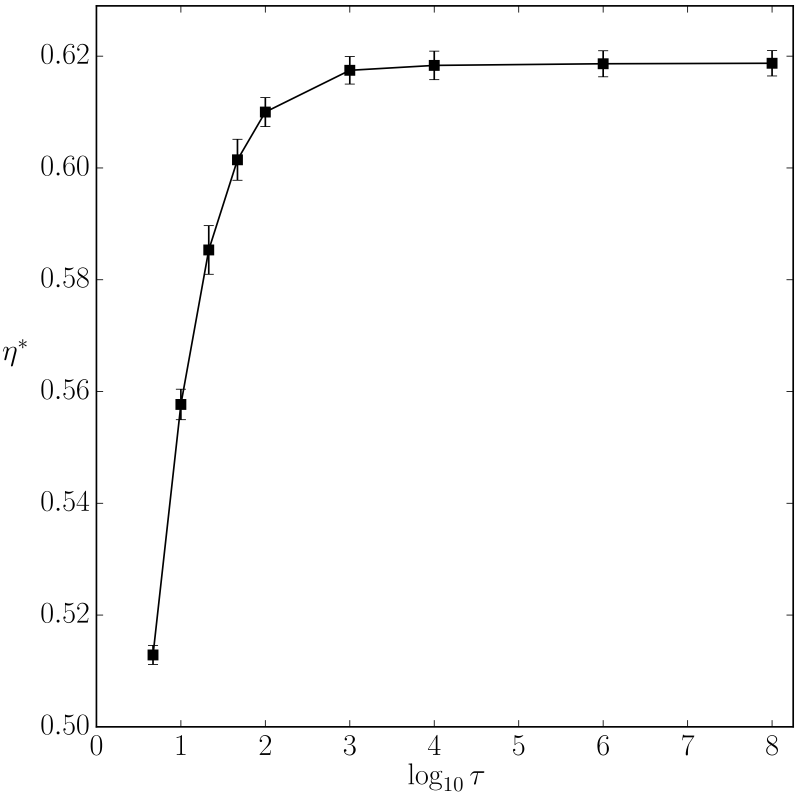

Figure 2.7: Dependence of the critical noise value $\eta^*(\tau)$ with anticipation time scale τ presented as $\log_{10}(\tau)$. Each point here corresponds to a peak determined from a Gaussian fit with associated standard deviation as uncertainty estimate as shown in figure 2.6. Simulations also performed as described in that figure caption.

in our simulations can be seen in figure 2.2: as N gets larger the transition point appears to approach this value. Testing at larger system sizes would help to see this with more precision.

At lower values of τ the transition point get smaller. In fact, as τ gets close to $\mathcal{O}(\delta t) = 1$ here, this value becomes very small, before it cannot be computed at around $\tau = 0.5$ as the system is disordered even in the limit of zero noise. In practice one should be careful performing measurement in this region. The density gets very high, therefore the time scale of the group (i.e. how long it would take to traverse the swarms longest linear distance at speed v_0) becomes close to the time scale of simulation δt. This causes the discrete nature of the interaction rules to dominate the dynamics, so reliable numerical simulation of the model can break down. However, as this is associated with the high density state, it is obvious when it occurs as the swarm has essentially collapsed.

Overall, the form of this relationship suggests that decreasing the time scale of anticipation makes the system less robust to noise, as less noise strength is required to break up the ordered phase. However, consulting figure 2.7 is encouraging as a huge part of the domain of τ, from $\mathcal{O}(1)$ and above, is robust to noise and widely supports an ordered phase.

2.4 Neighbour anticipation controls aggregation density

The discussion so far has primarily concerned the velocity degrees of freedom of the system; in this section we will focus on the position, specifically we will investigate how the neighbour interaction encourages group cohesion. We begin by describing how this is quantified in simulated swarms, then map out how the group density behaves with respect to the control parameters: noise η and anticipation time scale τ. This is used to identify different modes of behaviour observed in this model.

2.4.1 Quantifying cohesion

Consider the infinite τ limit of the model. It has been established in § 2.3.2 that swarms in this regime are not spatially stable and experience a diffusive expansion over time. For any finite value of τ there should be some, potentially very large, swarm size where expansion ceases. From a simulation perspective, this stable state is increasingly harder to reach for larger τ as longer simulation time scales are required. It is therefore important to define a spatially stable swarm with respect to this time scale. Specifically, we denote a spatially stable swarm as one which has been able to obtain a stable spatial extent over the simulation time T. But how do we measure spatial extent?

For a swarm at a specific instant in time there are a number of measures of spatial extent, both local and global, that could be used, each with their own associated strengths/drawbacks. For example, the mean distance of individuals from the centre of mass position, the largest distance between any pair of individuals in the swarm, or the ensemble-averaged mean distance to topological neighbours (as shown in figure 2.4). Another sensible choice could be the area of the group A. This would allow a number density to be assigned to the state via $\rho(t) = N/A(t)$. Due to the geometric construction used to assign neighbours in our simulation, we already have access to the area of the group as measured by the union of all simplicies in the Delaunay triangulation. This is known as the convex hull [68] and in two dimensions this is a representation of the point set $\{\underline{r}_i(t) | i \in \mathbb{N}_0, i < N\}$ as a convex

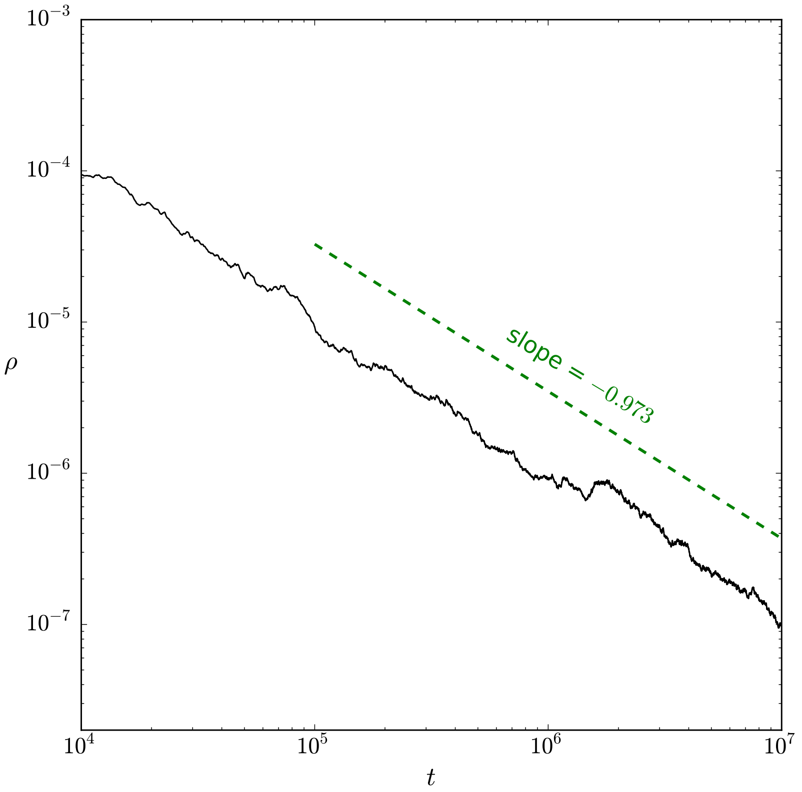

Figure 2.8: Swarm density converges to zero with time, specifically at the rate $\rho \sim t^{-0.973}$, with exponent close to the expected value of 1 for diffusive expansion. This example shows how we can identify a steady spatial state which would have an exponent of zero (and non-vanishing density). Simulation performed with $N = 2^{10}$, $\tau = 10^{12}$, $\eta = 0.61$ and $\rho_{init} = 0.1$. Linear fit on domain $t \in [10^5, 10^7]$. System is not in steady spatial state here therefore fit is to a transient of time scale $> T = 10^7$.

polygon. Simply, area is computed by summing up the areas of all the triangles in the triangulation. This allows us to work with densities $\rho(t)$ in the following.

Figure 2.8 shows the evolution of swarm density with time for a swarm in the large τ limit. Density decreases over time with a slope close to -1 on logarithmic axis. This suggests $\rho \sim 1/t$. This can be understood as a diffusive expansion (as previously discussed) as $\rho \sim A^{-1}$ and $A \sim \langle r \rangle^2$, and for diffusion $\langle r \rangle \sim \sqrt{t}$, so we do indeed expect $\rho \sim t^{-1}$. By allowing the simulation to equilibrate for a specified time T_{eq} and then fitting to the densities observed after, it is possible to understand the growth of the swarm over the time scale of the simulation. This allows us to quantify the cohesion in a simulated swarm.

2.4.2 $\eta - \tau$ phase diagram

Figure 2.9 shows the density of simulated swarms of $N = 64$ particles across the $\eta - \tau$ plane. For each instance, the swarm evolved for $T = 10^5$ time steps and a linear fit of $\log_{10}(\rho)$ against $\log_{10}(t)$ was performed in the region from $t = T_{eq}(= 2.5 \cdot 10^4)$ to T. The density values presented correspond to the $t = T$ value of this fit. The location of the phase transition is overlaid in order to identify regions of order/disorder.

At high τ the density is low, as expected. At low τ, it increases and density can get remarkably high when τ is close to the simulation time step $\delta t = 1$. Interestingly the ordered region has an extremely wide range of supported densities which suggests that the time scale of anticipation τ can control the density of the swarm very well.

Of additional note is the shape of the green dotted line in figure 2.9. This corresponds to unit density. It does not vary smoothly as it crosses the transition line. This is partly due to the discretisation of the parameter sweep, the resolution of which prevents a detailed estimate of this contour in this region. This may also suggest that order and density are not completely decoupled and could provide insight to the nature of the phase transition, as discussed in 2.3.1. It could also be quite an attractive feature in a biological setting. At roughly unit density, by varying the level of anticipation the system could move from order to disorder (or vice-versa) without affecting the overall level of cohesion in the group. This would allow such a system to respond to external perturbation quite robustly.

2.4.3 The cohesive steady-state

We have established how the density changes across a wide range of the $\eta - \tau$ parameter space. The densities presented relate to the final state of a system evolved over a specified simulation time. Up to this time scale, we would like to identify for what region of parameter space the swarms have found a cohesive steady-state. That is to say, for the parameters investigated, which values generate swarms that have been prevented from dissipating due to the neighbour anticipation interaction and can be termed a *cohesive* group with respect to the time scale of the simulation.

To do this we perform a linear fit to the logarithm of density with respect to the logarithm of time, as shown in figure 2.8, with the form $\log_{10} \rho = \alpha \log_{10} t + \beta$, where α is the slope of the fit and β is the intercept of the $\log_{10} \rho$ axis. This describes the change in density as $\rho \sim t^\alpha$, where the constant of proportionality is 10^β which indicates the initial density for expanding systems and the steady-state density for spatially stable systems. The value of α is shown on the $\eta - \tau$ plane in figure 2.10

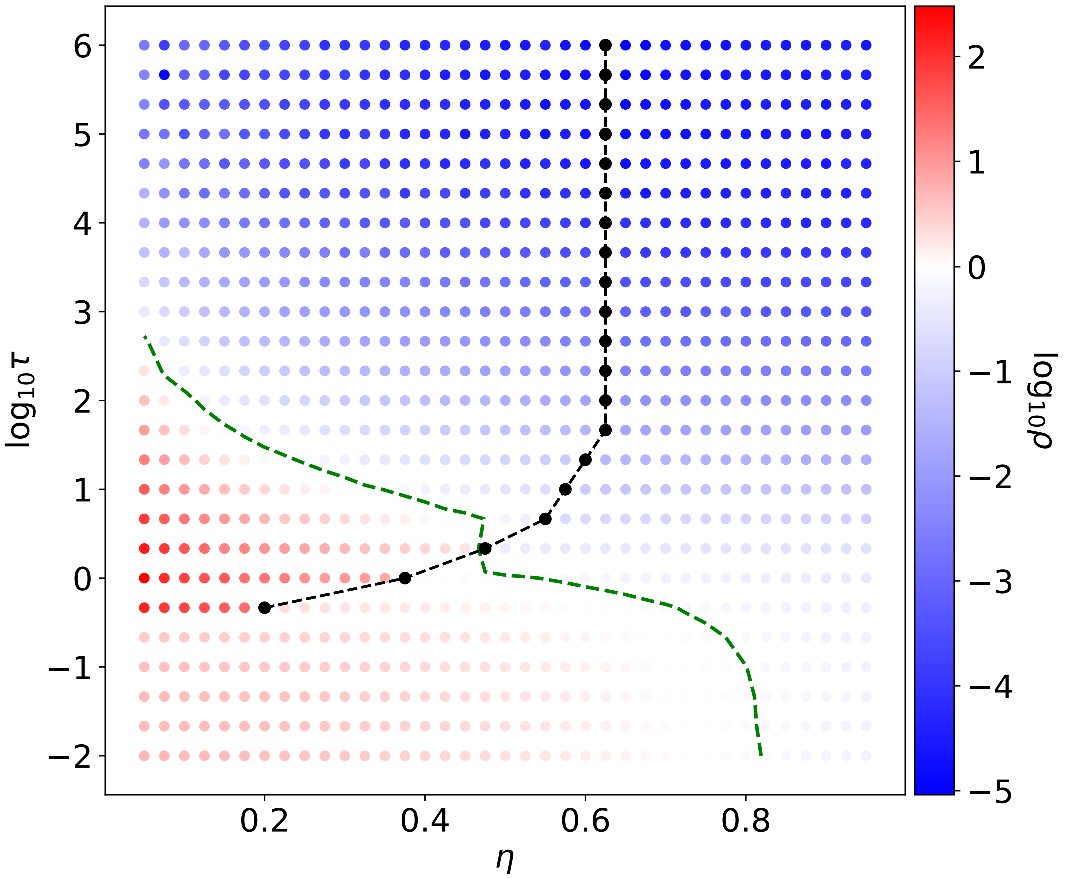

Figure 2.9: Phase diagram for neighbour anticipation model for $N = 64$ particles. Red/blue circles correspond to high/low density $\log_{10}\rho$ sampled at each (η, τ). Black circles correspond to the critical points $\eta^*(\tau)$ of the order-disorder phase transition discussed in 2.3 as determined by peak variance: order/disorder to the left/right of the black dotted line. Green dotted line corresponds to $\rho = 1$. Simulations initialised at $\rho_{init} = 0.1$ and run for $T = 10^5$ timesteps in total. Linear fit determined over domain $t \in [2.5 \cdot 10^4, 10^5]$. Density values presented correspond to the fit value at $T = 10^5$, the end of the simulation.

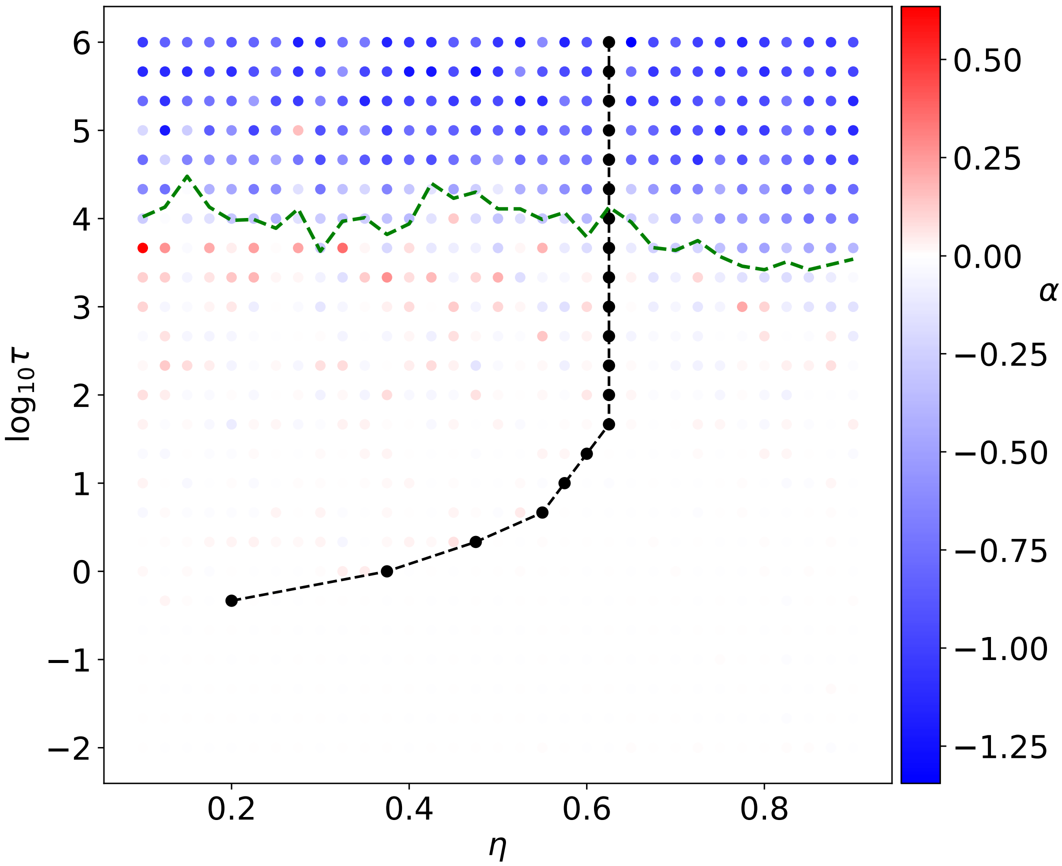

Figure 2.10: Identification of a region of $\eta - \tau$ space with spatially stabilised swarms. Linear fit to density of form $\log_{10}\rho = \alpha \log_{10} t + \beta$ performed as in figure 2.8 to obtain rate of expansion exponent α. Green dotted line corresponds to crossings of $\alpha = -0.25$. An expanding region (α close to 1) is present at high τ, but at lower values simulated systems can reach a cohesive steady-state (α close to 0).

for the same simulation procedure as for figure 2.9.

For large values of τ, α is close to 1, indicating that the group is still expanding over the course of the simulation. Below the green dotted line corresponding to $\alpha = -0.25$, α becomes much smaller, indicating that the group density is more or less stationary on the time scale $t \in [T_{eq}, T]$. These groups are cohesive.

The location of this separation line is determined by looking at the value of α for fixed η (vertical sections of figure 2.10) and determining the crossing point of this function with a threshold value of $\alpha = -0.25$. This procedure is shown in figure 2.11. This α threshold is determined broadly by the typical value of uncertainty in the estimation of α and provides a fairly unambiguous crossing value of τ for the $\alpha(log_{10}\tau)$ curves. As the values for this exponent have been determined for

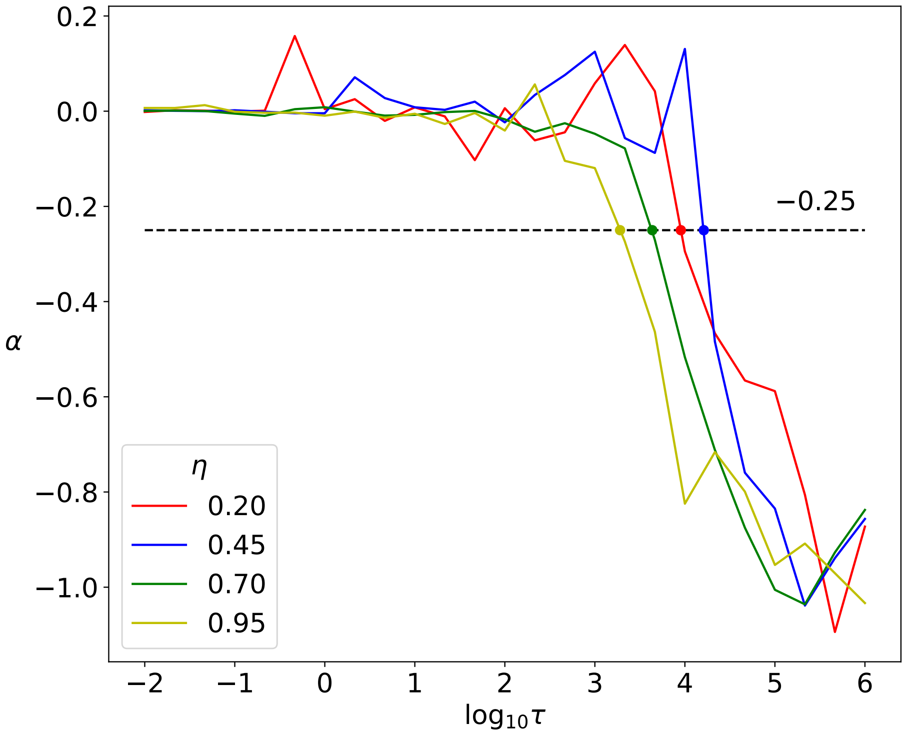

Figure 2.11: Determination of threshold τ for cohesive/expanding groups in figure 2.10 for a selection of noise strengths $\eta = \{0.20, 0.45, 0.70, 0.95\}$ (red, blue, green, yellow lines respectively). Crossing points of $\alpha(\log_{10}\tau)$ lines with $\alpha = -0.25$ (corresponding circles) provides an estimate of the region of τ for which swarm can reach a spatial steady-state within the time scale of the simulation.

time scale of the simulation, increasing this will move the separation line up toward higher τ values, as the simulated systems have more time to stabilise spatially.

2.4.4 Characterisation of swarm behaviour

We have now established regions of the parameter landscape which result in order/disordered and cohesive/dissipating swarms and have determined how the specific density depends on (η, τ). The resulting behaviour of simulated swarms in different regions of this parameter space is therefore quite varied. We present a broad overview of this in figure 2.12.

We identify regions depending on three criteria: order, cohesion and density. Sample configurations from each of these regions are provided in figure 2.13. For each, polarisation P and linear swarm size $L = \max_{i,j} |\underline{r}_j(t) - \underline{r}_i(t)|$ as the largest distance between any pair of group members.

The shaded area in figure 2.12 highlights a region of high polarisation. At

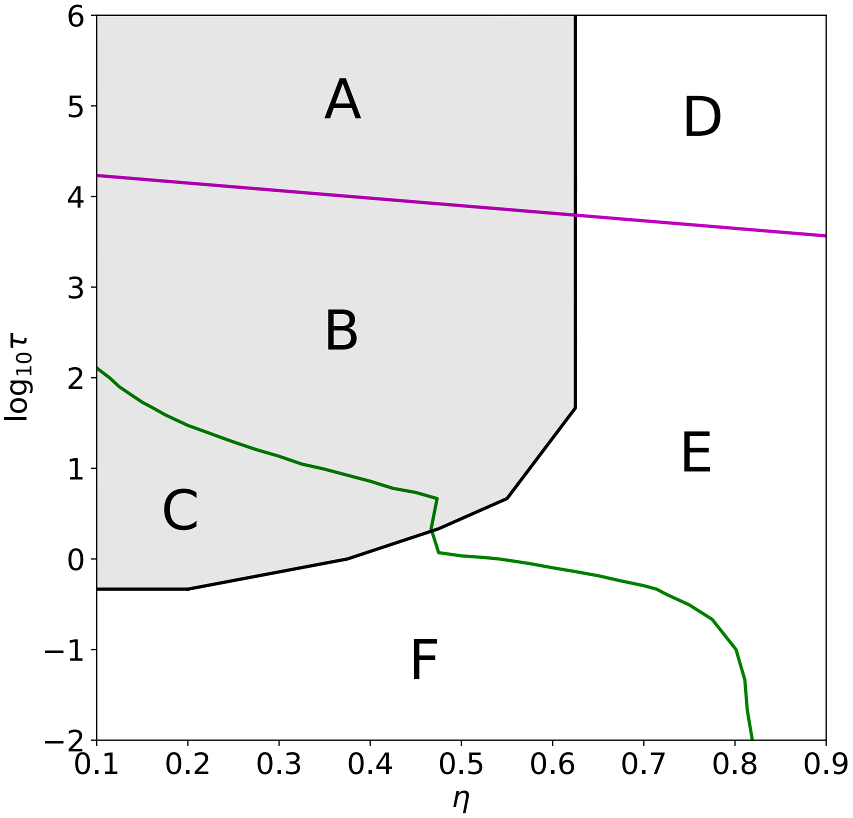

Figure 2.12: $\eta - \tau$ phase plane with regions of characteristic swarm behaviour identified: (A) ordered dissipating, (B) ordered cohesive, (C) highly dense ordered, (D) disordered dissipating, (E) disordered but at steady density and (F) highly dense disordered. Configurations for each presented in figure 2.13. Grey region (A, B, C) is high order, white region (D, E, F) is low order; black line denotes transition between these. Green line denotes $\rho = 1$. Magenta line is a fit to points along green dotted line in figure 2.10: above this groups do not reach a spatial steady-state in the time scale of the simulation $T = 10^5$, below they do with density as shown in figure 2.9.

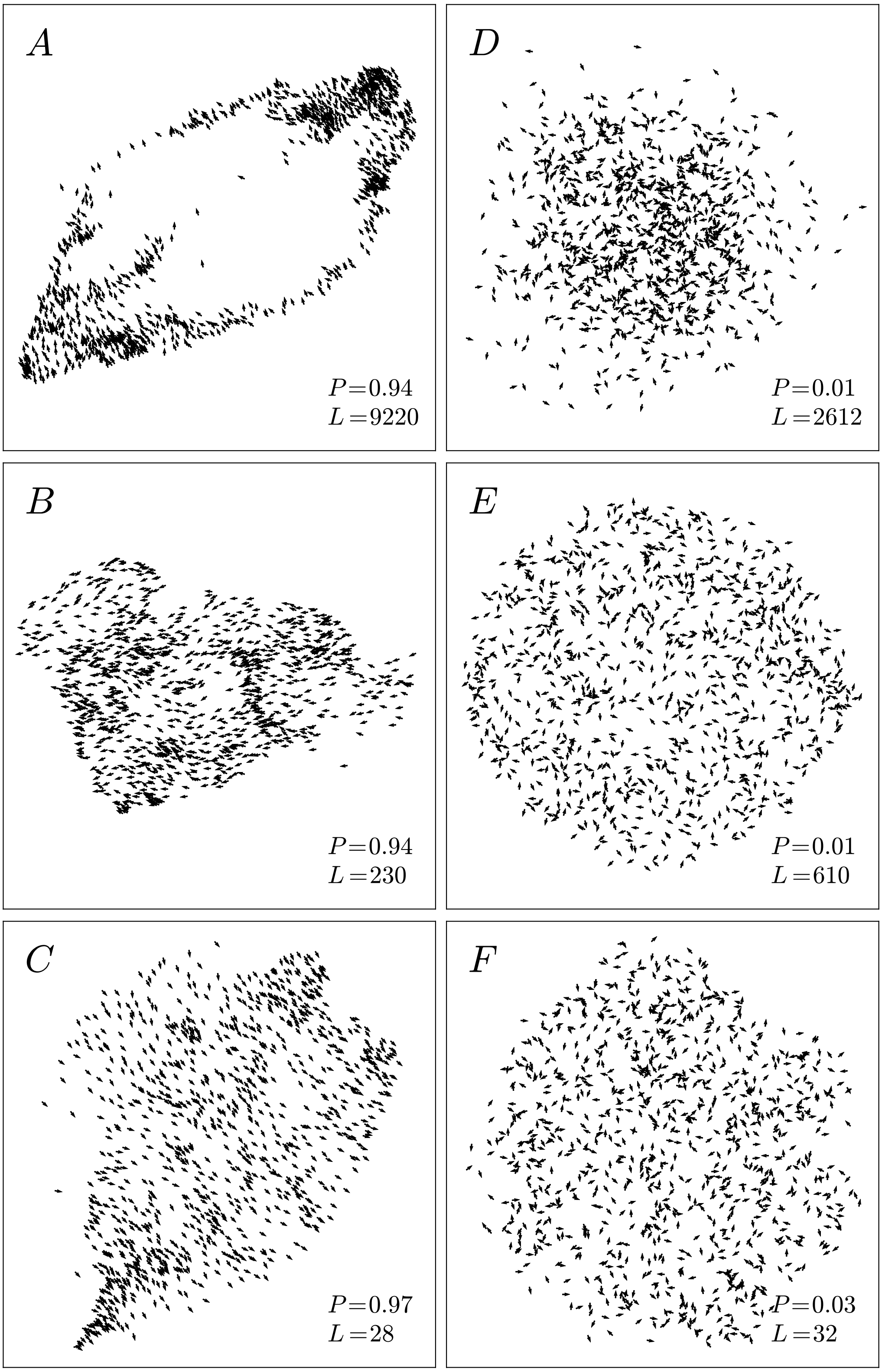

Figure 2.13: Swarm configurations for different types of group identified in neighbour anticipation model. $N = 2^{10}$. Labels correspond to regions in figure 2.12.

high τ, the group does not cohere, but does develop strong order (A: $\eta = 0.35, \tau = 10^5$). Initialised as a maximally disordered state the group expands until it develops high order via its topological interactions between individuals. This suppresses the dominant mode of the expansion as the group translates together at high P. Expansion continues driven by diffusive fluctuations in velocity. The spatial structure is now "frozen in" since there is very little relative motion within the group and the large distances cause the Delaunay triangulation to be very stable over time, with only rare changes in its connectivity. This causes the large region of sparsity observed in 2.12 (A).

Both (B: $\eta = 0.35, \tau = 10^2$) and (C: $\eta = 0.25, \tau = 10^1$) are a cohesive, highly ordered state. The long-ranged order is obvious in the configuration plots. The key difference is the length scale. (C) is very dense ($\rho \approx 3$) however (B) is much less so ($\rho \approx 0.05$). We have previously discussed the importance of the simulation length scale in § 2.2.3, which is $v_0/\delta t = 1$ here. This suggests that densities greater than 1 (green dotted line) are undesirable. From a biological perspective, consider a classic example of swarming: a murmuration of Starlings. The observed densities in real-world flocks are typically $0.05 - 0.5$ [3], i.e. relatively sparse. This helps avoid collisions, but can also help individuals navigate and avoid predators as vision is a key information stream for individual birds, and if density is too large this would be inhibited [76]. In this sense, the region (B) corresponds to "real-world" swarms, that is a highly ordered and cohesive group.

In the disordered region at high η, (D: $\eta = 0.75, \tau = 10^5$) and (E: $\eta = 0.75, \tau = 10^2$), there are still some obvious differences in global structure, as can be seen in the configuration plots. (D) has a very large spatial extent and the density is not homogenous, since the edges appear to be relatively sparse. This is due to the τ term in equation 2.4 dominating, as previously discussed, which does not generate sufficient inward drift for spatial stability. Contrast with (E) which appears to have a homogeneous distribution of individuals in the group, as well as a stable moderate density ($\rho \approx 0.005$). We can make an analogy with thermodynamic systems again, by relating noise with temperature (as the source of fluctuations) which can be thought of as an outward pressure. This drives particle mass away from the group centre. Bounding the system using the neighbour anticipation interaction generates an effective force which appears to be stronger further from the centre, i.e. radially symmetric. The system then appears to be in an effective-force-balanced state. This is discussed further in § 2.5.1. Therefore the group edge is more sharply defined, and density more homogenous, in region (E) than (D).

Finally if τ is reduced to a small enough value group order is impossible (D:

$\eta = 0.5, \tau = 10^{-1}$). This generates very dense disordered states for most values of noise, until around $\eta = 0.8$ where the group members are almost completely non-interacting as noise overwhelmingly dominates.

2.5 Additional considerations

2.5.1 Mechanism of cohesion

We would like to understand the specific reason why the interaction described in § 2.2.2 can generate cohesion of the group as a whole. The neighbour anticipation interaction that we have proposed in this model, when considered on two particles in isolation, acts in the direction from the particle in question i toward its neighbour j. If one considers a generic cohesion promoting two-particle interaction, that is one that acts to reduce the separation of these two particles, it is not clear that the global effect would be to bind the group *as a whole*, instead of generating increased local densities.

In our model however, neighbours are assigned topologically, which precludes group fragmentation. This suggests the source of the whole group cohesion is in the structure of the Delaunay triangulation that defines these topological neighbours. For a Delaunay triangulation on a Poission point process, it is known that the expected number of neighbours for any individual is a constant value [96]: asymptotically 6 in two dimensions [61] and $\frac{48\pi^2}{35} + 2 = 15.54$ (4 s.f.) in three dimensions [60]. Due to the nature of this process, these neighbours would be on average distributed isotropically. However for a distribution on a disk in $\mathbb{R}^2$, near the edges this would certainly not hold and neighbours would all be distributed on one side, specifically toward the centre of the disk.

This observation suggests a measurement we can make on our simulated swarms which will quantify the isotropy in the distribution of topological neighbours for a particle i at time t:

$$\underline{\Delta}_i(t) = \frac{\sum\limits_{j \in B_i} \widehat{\underline{r}}_{ij}(t)}{\mathcal{N}_i(t)}, \tag{2.8}$$

where $\underline{r}_{ij}(t) = \underline{r}_j(t) - \underline{r}_i(t)$, so $\widehat{\underline{r}}_{ij}(t)$ points in the direction of neighbour j from particle i, B_i is the set of topological neighbours of particle i at time t and $\mathcal{N}_i(t)$ is the number of neighbours of i (i.e. the size of B_i). Therefore, $\underline{\Delta}_i(t)$ will point in the dominant direction of the neighbour distribution for i. As it is normalised, $|\underline{\Delta}_i(t)| = \Delta_i(t) \in [0, 1)$, with exclusive upper-bound due to the nature of the triangulation. If neighbours are isotropically distributed then this will be on average close to 0, but if there is a preferred direction it will increase towards 1. We also define $\underline{R}_i(t) = \underline{r}_i(t) - \underline{r}_{cm}(t)$ which points from the position of i to the centre of mass of the group $\underline{r}_{cm}(t)$. This can also be normalised in magnitude in order to aid comparison between states, as shown in equation 2.9.

$$R_i'(t) = \frac{|\underline{R}_i(t)|}{\max\limits_{i \in S} |\underline{R}_i(t)|}, \tag{2.9}$$

where S denotes the set of all N particles in the swarm. Also define C as the subset of S which lie on its convex hull [68]. Therefore particles in $S \setminus C$ lie in the bulk of the group.

Figure 2.14 shows the relationship between the magnitude of the anisotropy in the distribution of topological neighbours and the relative distance sampled for simulations in the disordered cohesive phase (E: $\eta = 0.75, \tau = 10^2$). This phase was chosen as it is cohesive in our typical simulation time scale $\mathcal{O}(10^5)$ and has stable morphology allowing many configurations to be sampled and aggregated reliably. Additionally this state appears to be approximately homogeneous (c.f. the Poisson process motivation discussed above). It is also not in the ordered state, therefore there is no weak cohesion from group alignment present. All of the bounding should therefore be due to this geometric effect. As expected, the anisotropy in topological neighbour distribution is maximal furthest from the centre of mass position. By separating out the contribution from particles on the convex hull (red line) it becomes clear that they are the main cause of this effect. This is as expected since the convexity condition excludes at least half of the directional domain. However it is interesting to observe that some particles *not* on this hull still experience this neighbour anisotropy, as evidenced by the green line increasing at high R_i'.

We next consider specifically where this anisotropic direction is pointing when it is of high magnitude. We project the neighbour anisotropy $\underline{\Delta}_i$ onto $\widehat{\underline{R}}_i$ as it always points towards the centre of the group by construction, and define this as $\Delta_i^{cm} = \underline{\Delta}_i \cdot \widehat{\underline{R}}_i$. Figure 2.15 shows this compared to the distance from the group centre R_i' (= 0 at the centre, 1 furthest away from it). Near the centre $\Delta_i^{cm} \approx 0$ suggesting an approximately isotropic neighbour distribution for individuals near there. However towards the edge $\Delta_i^{cm} \approx 1$, which indicates that not only is the neighbour isotropy high there (as we have determined in figure 2.14) but also that the direction of this anisotropy is in the direction of the centre of mass. Recalling the radial symmetry in the construction of $\widehat{\underline{R}}_i$ and that R_i' is normalised distance from centre of mass, we conclude that the neighbour anisotropy should always increase toward the group edge and point to the group centre. Furthermore this suggests

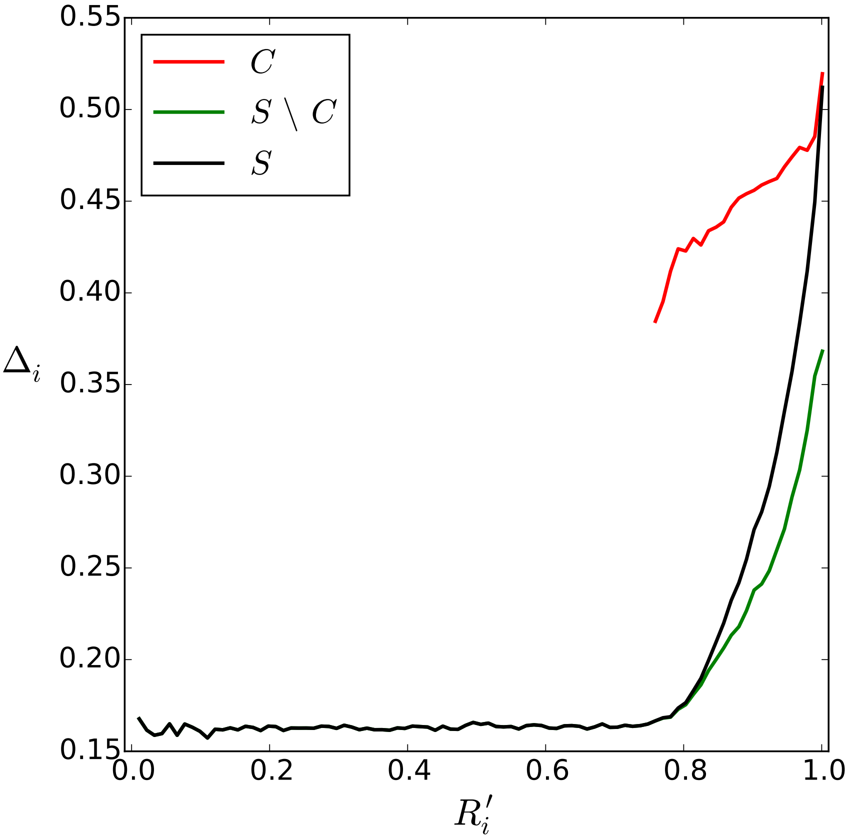

Figure 2.14: Magnitude of anisotropy in the distribution of topological neighbours for particle i at normalised distance from centre of mass R_i', shown for all particles in the swarm S (black), the convex hull C (red) and the bulk $S \setminus C$ (green). Simulation was performed with control parameters $\eta = 0.75$ and $\tau = 10^2$ (region E) with $N = 2^{10}$ starting at ρ_{init} for $T = 5 \cdot 10^4$. $T_{eq} = 4 \cdot 10^4$ are discarded and samples taken for each i at a given time step. 1000 configurations are sampled at every 10 time steps after equilibration, and aggregate R_i' discretised into 100 bins. There is a sharp increase at R_i' close to 1 corresponding to an increased anisotropy in neighbour distribution toward the edge of the group.

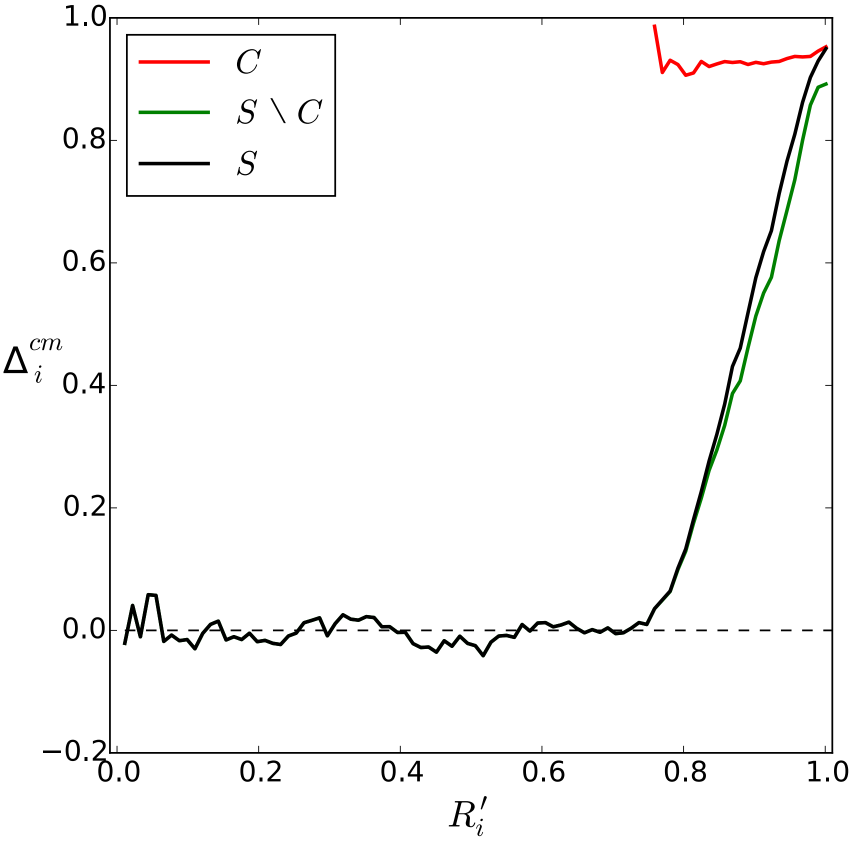

Figure 2.15: Anisotropy in the distribution of topological neighbours for particle i projected onto the direction pointing from i toward the centre of mass at normalised distance from centre of mass R_i', shown for all particles in the swarm S (black), the convex hull C (red) and the bulk $S \setminus C$ (green). Simulation procedure same as for figure 2.14. As this anisotropy grows toward the edge of the group, it does not do so arbitrarily, rather it points toward the group centre ($\Delta_i^{cm} = \underline{\Delta}_i \cdot \widehat{\underline{R}}_i$ approaches 1).

that the observed neighbour anisotropy does not originate from local differences in structure of the triangulation, say due to the presence of large internal concavities.

Interpreting this bounding effect as a force acting on a particle by its topological neighbours, the net force on the particle is close to zero in the bulk. However it gains a preferred direction as the neighbour distribution deviates from isotropic. This suggests that the mechanism of whole group cohesion observed in our model is the anisotropy in the distribution of topological neighbours that increases towards the edge of the group.

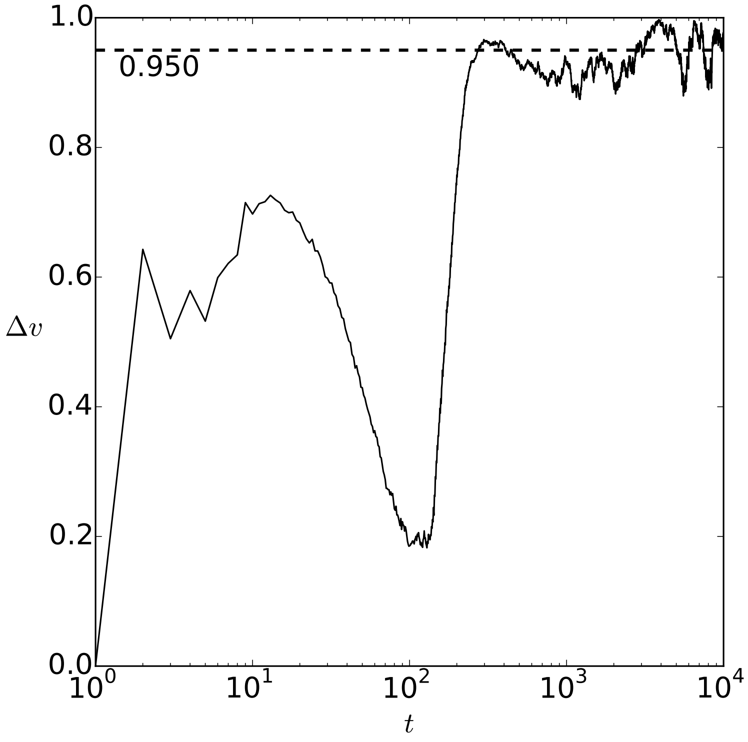

Figure 2.16: Evolution of the mean difference between inferred and explicit velocity $\Delta v = \langle \langle \underline{v}'_j(t-1) \cdot \underline{v}_j(t-1) \rangle_{j \in B_i} \rangle_{i \in S}$ over time t for a simulated system of $N = 64$ particles with $\tau = 10^6$ and $\eta = 0.05$ near initialisation, with $\rho_{init} = 0.1$, $T = 10^5$ and $T_{eq} = 0.5 \cdot 10^5$. Dotted line highlights value in polarisation steady-state of 0.950 (3 s.f.).

2.5.2 Determination of neighbour trajectories

The model we have introduced uses an interaction based on neighbour anticipation in which a particle i moves toward the expected future position of each of its neighbours. This position is computed by using information from the near past to determine neighbour trajectory, assuming uninterrupted motion along this path. To first order, as we have presented in this work, this is ballistic motion at an inferred previous velocity $\underline{v}'_j(t - \delta t)$.

We are interested to confirm whether this process is performed well at each simulation time step. Figure 2.16 shows the difference between the inferred previous velocity $\underline{v}'_j(t-1)$ and its actual value $\underline{v}_j(t-1)$ computed as its cosine distance $\Delta v_i = \langle \underline{v}'_j(t-1) \cdot \underline{v}_j(t-1) \rangle_{j \in B_i}$. This has value 1 when these velocities coincide and -1 when they point in opposite directions, as the magnitude of the fixed speed here is 1. The figure specifically shows how this difference, ensemble averaged over N particles in the simulated swarm ($\Delta v = \langle \Delta v_i \rangle_{i \in S}$), evolves over time, for a swarm in the ordered regime. At the initialised disordered state, this is done poorly (Δv close to 0), however as the group achieves order this improves dramatically, approaching an time-averaged value of $\langle \Delta v \rangle_{t \in [T_{eq}, T]} = 0.950$.

It is encouraging that the system can obtain this ordered state when approaching from a disordered one, where the determination of neighbour trajectories is done relatively poorly. In fact, we observe a robustness of this process due to the central limiting effect of averaging over neighbours: deviations of $\underline{v}'_j(t-1)$ from $\underline{v}_j(t-1)$ are smoothed out when determining the new orientation due to the summation in the interaction rule shown in equation 2.5. This robustness is precisely why an ordered state can develop from disorder despite a non-perfect computation of neighbour trajectories. Overall, this analysis suggests that the determination of neighbour trajectories in this way does not inhibit the model from generating alignment, which we have seen throughout this work and particularly in § 2.3.

2.6 Conclusions

We have introduced a topological model of swarming that is bound in open boundary conditions, producing cohesive and aligned swarms. The form of interaction we proposed to generate this cohesion is that an individual moves to where it anticipates its topologically assigned neighbour to be at some time in the future: aligning with its presumed goal in space rather that its specific orientation, as is typical in traditional models of collective motion [32]. This allows us to use a single rule to generate both alignment and cohesion, rather than two rules which attempt to manifest these behaviours independently. This rule set is completely homogeneous with no special treatment of individuals in the flock required to produce this bounding, and we have shown that its mechanism takes advantage of the underlying geometric construction defining interacting neighbours to establish the strength and direction of the effective bounding forces. We have shown that neighbour anticipation can drive cohesion in (topologically) co-aligning groups.

We have identified a number of characteristic behaviours displayed by this model by mapping out its phase diagram, identifying how the anticipation interaction affects the robustness of the ordered phase, and compared this with the resulting density of the swarms across this region. We have then analysed the spatial stability of these states, with respect to a specific time scale of simulation, in order to identify steady states of particular densities and other dissipating states. We have also analysed the presented model in the limit of high anticipation, retrieving the topological Vicsek model which has been well-studied in terms of universality class and in the continuous limit. It remains to be seen whether this feature may allow us to describe our model more easily in terms of a continuous theory.

If we draw an analogy with particle diffusion in a potential well, for which the root-mean-squared (r.m.s.) distance from the centre of the well can be derived for many symmetric cases of potential, it may be that we could relate this r.m.s. distance with the distance to the boundary for our swarming particle ensemble in order to describe the bounding as an effective potential which could be used in a continuous description of the system. There may also be a similar argument via force balance of outward diffusive pressure and inward bounding which could help derive the observed form of the density surface on the phase diagram. Any such description would be subject to the effect of considering these particles as active and so the traditional fluctuation-dissipation relation being violated. Recent work [66, 87, 88] has however considered many of the effects of bounding active particles and it was found that an effective fluctuation-dissipation theorem still holds [31]. This is currently a very active area of research.

Chapter 3

Density distributions and depth in flocks

Work in this chapter has previously appeared in the article "Density distributions in flocks" by Lewis and Turner [56].

It has been demonstrated in chapter 2 that it is possible to bound a topological model of swarming in open space by introducing a specific model that can successfully do so and by studying its behaviour. This establishes the ability of models with this type of neighbour interaction to obtain a steady group density that is greater than zero; i.e. we can take a topological swarm out of periodic boundary conditions and still keep it together. In the following chapter we will show that, despite the challenges the biologically-motivated topological constraint provides, we can go one step further and prescribe the *distribution* of density of the group. Specifically, we will focus on reproducing density distributions that are seen in naturally occurring flocks of birds.

3.1 Introduction

In recent years, a large number of theoretical models have been developed in which local interaction rules give rise to global ordering in animal systems [13, 14, 32] however empirical studies have been more rare [47, 59]. Testing models against data is essential if we are to determine which sorts of model give rise to specific characteristics: many models can generate some form of swarming, but which of these models give rise to swarms that resemble those seen in nature? Specifically, in terms of comparable observable quantities of the group (such as density, structure and shape) and its dynamic behaviour in different situations (say, under the external pressure of a predator attack). It has been suggested that the specific interaction mechanism may vary with species and for some systems an interaction based on neighbour distance appears to be a good fit [102]. In contrast, recent field studies have reconstructed the internal dynamics of large flocks of Starlings and have determined that their nearest-neighbour interactions do not depend on interaction range [3, 4, 18].

Developing models with this *metric-free* characteristic is technically challenging as they typically support a zero density steady-state, such as described in the work of Ginelli and Chaté [34] in which diffusive expansion continues indefinitely. Pearce and Turner [75] describe a model that regulates swarm density using a motional bias on surface individuals and *topological* interaction rules, preserving the metric-free nature of the model and also generating a steady-state with finite spatial extent. This Strictly Metric-Free (SMF) model is therefore useful to compare with observations of bird flocks as it can produce bounded swarms in open boundary conditions. However we will show that, in its simplest form, it yields density distributions that are rather different to those observed in nature.

In this chapter we propose a fully topological (metric-free) 3-dimensional model which includes a motional bias that is tunable throughout the swarm and not just on its surface. This bias has a topological character, preserving the fully topological nature of the model. Our aim is to explore the regulation of density across flocks of birds. We are motivated by findings from a field study [4] that reports a nonhomogeneous density variation across flocks of Starlings, specifically a higher density at the border of the flock than in the centre. This observation is counter to what has been observed in some other models of collective behaviour [52]. It is also counter-intuitive in relation to some theories of animal behaviour, such as the selfish herd hypothesis [38] in which the centre of the group would be the safest location and all individuals might therefore be expected to seek to occupy it. We show that our metric-free distributed motional bias model is able to support behaviour consistent with these empirical observations.

The model is introduced in § 3.2. The methods used to measure aggregate densities and fit the model to data are described in § 3.3. The resultant model and swarm density profiles are presented in § 3.4. Additionally, a biologically motivated basis for an individual determining their depth from within the flock is presented and discussed in § 3.5. Concluding remarks are in § 3.6.

3.2 Description of the model

The model we propose[1] begins with the surface bounding effect introduced in the SMF model [75] and extends it to act on all individuals in the aggregate with strength prescribed by a function of the topological depth of the individual within the swarm. In contrast to classic models of self-propelled particles, such as those by Vicsek *et al.* [103], we identify two particles to be neighbours if they are directly connected to each other under a Voronoi tessellation [54, 68]. This is constructed for the particle positions at each time step, thus defining interacting neighbours as those in neighbouring Voronoi cells (i.e. particles which share an edge in the Delaunay triangulation of all particle locations).

3.2.1 Topological depth

We use a Voronoi tessellation to determine *topological depth* for each of the particles in the dynamic aggregate (flock). We first identify a shell, or set, of particles as being those that occupy an infinite Voronoi cell (that is, a cell of the tessellation that is not fully bounded). These are denoted as occupying shell 0 and correspond to particles that are on the convex hull of the system [68]. Particles that are connected to these shell 0 particles via Delaunay edges, but that are not themselves members of shell 0, are defined to lie in shell 1. This process is repeated iteratively until all particles are assigned a shell number, and is clarified explicitly in algorithm 1. Figure 3.1 provides a step-by-step example of shell labelling in 2D. The 3D version, as used in this study, is defined analogously.

This labelling encodes topological depth as it relates to the shortest path length from the border through the graph defined via the Delaunay triangulation, which gives us a broad idea as to how many particles are between each particle and the edge of the swarm. A driving term can then be included in the equation of motion that provides a motional bias on each particle. The direction of this bias (loosely "inwards" or "outwards"), is derived using the locations of its neighbours on the same shell.

3.2.2 Direction of motional bias

Figure 3.2 shows the way in which the direction of motional bias is determined for a typical particle (shown for shell 0: a border particle, and analogously for others). We average over the unit vectors pointing from this particle i to its shell neighbours

---

[1] The concept of this model was conceived in a Master's dissertation by Lewis and Turner [55]. Ideas presented in this work have been developed substantially since then.

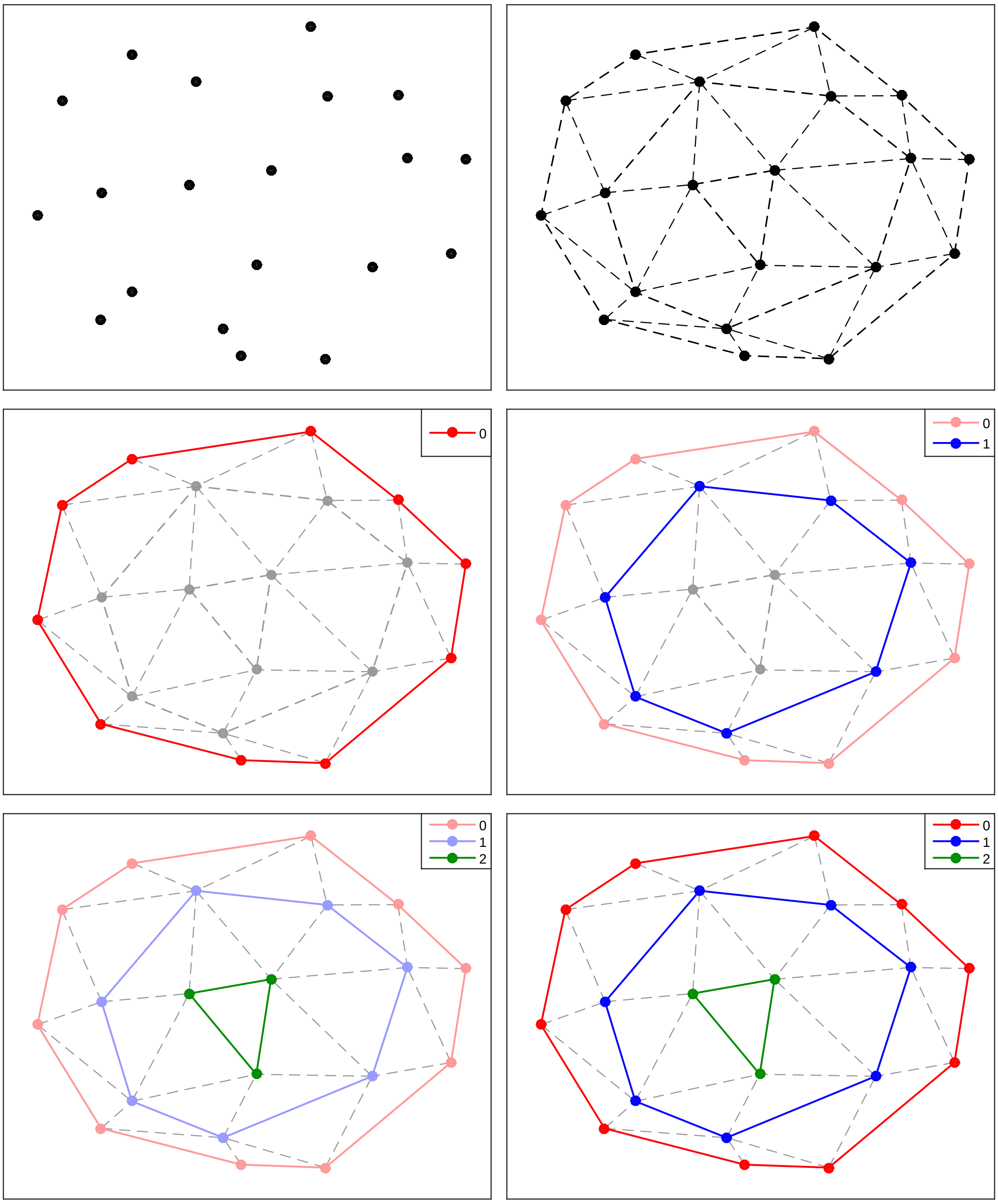

Figure 3.1: Schematic of system topology (shown as a 2D sketch for clarity): picture series illustrating successive labelling of shells from the border (shell 0) inward. (a) Black circles are particle positions at time t. (b) Black dashed lines denote edges of Delaunay graph that is dual to Voronoi tessellation of particle positions. (c) Particles on the convex hull of this point set (those which occupy infinite Voronoi cells) are defined as shell 0 (red), that is the border of the flock. (d) Moving inward, we label all particles that are connected to shell 0 particles via an edge (which are not yet labelled) as shell 1 (blue). (e) This is done iteratively, defining shell 2 particles (green) as those connected to shell 1 particles. (f) This is terminated when all particles have been labelled.

Algorithm 1: Iterative determination of topological depth for each individual.

```
Input  : Particle positions $\underline{r}_i$ for $i \in [1 \dots N]$.
Output : Associated topological depth $\kappa_i$ for each particle $i$.

// First, compute triangulation of particle positions:
$DT \leftarrow$ DelaunayTriangulation($\underline{r}_1, \dots, \underline{r}_N$);
// and initialise $\kappa$ as length $N$ array of $-1$'s:
foreach $i \leftarrow 1$ to $N$ do $\kappa[i] \leftarrow -1$;
// and initialise empty list of particle indicies at the
   current Voronoi layer (depth):
depthList $\leftarrow \emptyset$;
// Next, identify particles on convex hull:
neighbours $\leftarrow \emptyset$;
for edges $e \in DT$ do
    $q_1, q_2 \leftarrow$ indices of vertices of $e$;
    if isInfinite($e$) then    // $e$ connects to infinite vertex
        $q \leftarrow$ index of non-infinite vertex of $e$ (i.e. $q_1$ or $q_2$);
        $\kappa[q] \leftarrow 0$;
        // as $q$ must lie on convex hull
        depthList = depthList $\cup$ q;
    else
        neighbours $[q_1] \leftarrow q_2$;
        neighbours $[q_2] \leftarrow q_1$;
        // which builds a look-up for later use

// Then, search inward to find each new Voronoi layer,
   labelling particles with topological depth as found:
depth $\leftarrow 1$;
while | depthList | $> 0$ do          // still finding unlabelled
    newDepthList $\leftarrow \emptyset$;
    for $q \in$ depthList do
        for $m \in$ neighbours $[q]$ do                // using look-up
            if $\kappa[m] == -1$ then
                $\kappa[m] \leftarrow$ depth;
                // i.e.  if unlabelled particles found
                   connected to the previously labelled
                   layer, label new particles with depth
                newDepthList $\leftarrow$ newDepthList $\cup\ m$;
    depthList $\leftarrow$ newDepthList;
    depth $\leftarrow$ depth + 1;
// Leveraging the fact that no particles are disconnected
   from the triangulation to fill $\kappa$ and conclude process.
```

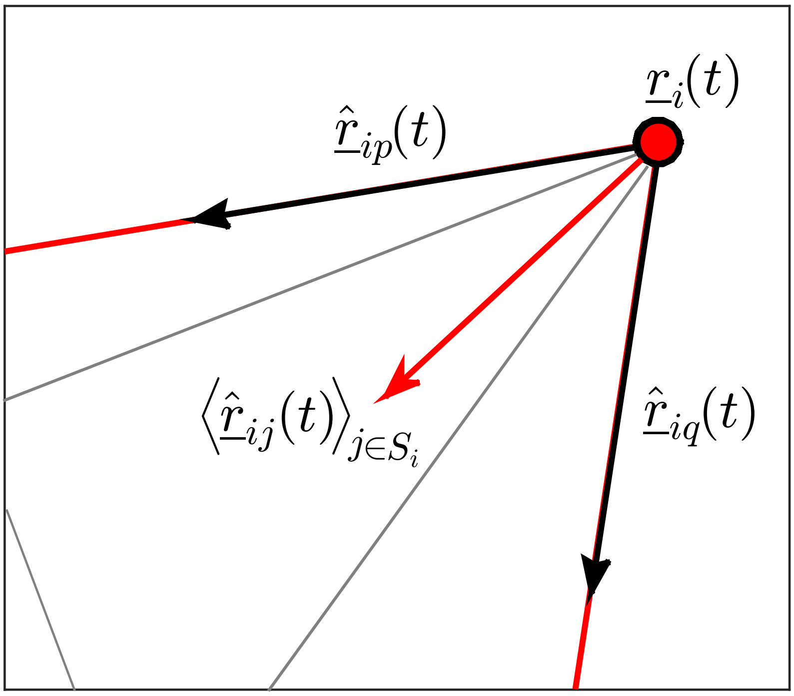

Figure 3.2: Illustrative construction of bounding term for particle i at $\underline{r}_i(t)$ with shell neighbours p and q. Other neighbours (in B_i only) connected via grey lines. Effect direction (red arrow) is average of unit vectors pointing from particle i to each of the shell neighbours $S_i = \{p, q\}$, i.e. $\langle \hat{\underline{r}}_{ij}(t) \rangle_{j\in S_i}$.

S_i, so this will be pointed inwards, on average. For shell 0, this becomes more strict: it will always point inwards, due to the convex nature of the hull that defines this outermost shell. Note, that as this construction relies purely on the *directions* of topological (specifically same shell) neighbours, not their distance, the metric-free nature of the interaction is fully preserved by this effect.

3.2.3 Interaction rules

The interaction rules governing all N identical particles in the system are:

$$\underline{r}_i(t+1) = \underline{r}_i(t) + v_0 \hat{\underline{v}}_i(t), \tag{3.1}$$

$$\underline{v}_i(t+1) = (1-\eta)\hat{\underline{\mu}}_i(t) + \eta \hat{\underline{\xi}}_i(t), \tag{3.2}$$

$$\underline{\mu}_i(t) = f_i \langle \hat{\underline{r}}_{ij}(t) \rangle_{j\in S_i} + (1-f_i)\vartheta\big(\langle \hat{\underline{v}}_j(t) \rangle_{j\in B_i}\big). \tag{3.3}$$

They involve the position $\underline{r}_i(t)$ of particle i at discrete time t, having direction of motion $\hat{\underline{v}}_i(t)$ and constant speed v_0, which is set equal to unity in what follows. The "hat" symbol ˆ denotes a normalised (unit) vector and angled brackets $\langle \cdots \rangle$

indicate an average over the indicated particle subset. The operator $\vartheta(\ )$ performs normalisation via $\vartheta(\underline{w}) = \underline{w}/|\underline{w}|$ and $\hat{\underline{r}}_{ij}(t)$ denotes the unit vector pointing from particle i to particle j at discrete time step t. The parameter η encodes the strength of the (vectorial [22]) noise applied to each particle, multiplied by a random unit vector obeying $\langle \hat{\underline{\xi}}_i(t) \rangle = 0$ and $\langle \hat{\underline{\xi}}_i(t) \cdot \hat{\underline{\xi}}_j(t') \rangle = \delta_{i,j}\delta_{t,t'}$. The neighbours of particle i are denoted B_i and particles which share the same shell number $\kappa(i)$ as particle i form the set $C_{\kappa(i)}$. Therefore we denote the set of shell neighbours of i as the intersection $S_i = B_i \cap C_{\kappa(i)}$. We average over the unit vectors pointing from particle i to members of this set, as described in § 3.2.2. In addition, figure 3.1 shows how shell 0 is defined as the members on the convex hull of the system, and also the procedure for identifying all other shells.

Equation 3.1 represents a simple vectorial particle translation along the current velocity. Equation 3.2 encodes an update rule for the velocity that includes both some deterministic driving terms, weight $(1 - \eta)$, and some stochastic noise, weight η. Thus η, the degree of noise, is an important control parameter in what follows. Equation 3.3 defines the deterministic driving terms. It is comprised of two terms, the first, with weight f_i, encodes the motional bias constructed from the shell geometry, as described and the second term, with weight $(1 - f_i)$, provides co-alignment of each particle with its neighbours.

We denote f_i as the "bounding function", which encodes the relative strength of the bounding effect on each Voronoi shell. Changing this allows us to tune the bounding of the model across the aggregation as we wish. If we choose f_i to have the form of equation 3.4, where λ is a parameter controlling the strength of the border shell effect, then we can recover the Strictly Metric-Free (SMF) model of Pearce and Turner [75] in its entirety. If instead we choose $f_i = 0\ \forall i$ then we recover the unbounded metric-free model of Ginelli and Chaté [34].

$$f_i = \begin{cases} \lambda & \underline{r}_i(t) \in C_0 \\ 0 & \text{otherwise} \end{cases} . \tag{3.4}$$

In our model, which uses topological shell depth, the value of f_i is the same for all particles in the same shell and can therefore be mapped to a lower dimensional parameter set $f_{\kappa(i)}$. We believe that this generalisation of the SMF model is natural, allowing us to describe the motional bias, not as a specific characteristic for a subset of birds, but as a rule for all birds that has a strength that depends on the relative depth of an individual in the swarm.

3.3 Methodology

We are interested in measuring the density variation across our simulated swarms. As we wish to compare directly to the empirical study of Starling murmurations [4] we seek to compute this in a similar fashion. The type of flocks which were studied in [4] were non-columnar and compact, with sharp borders, containing on the order of hundreds to thousands of birds, and which moved nearly linearly for sufficiently long times so as to treat their behaviour as near steady-state. The type of density variation we are interested in here is the density profile across flocks in this steady state, which is observed to be higher near the edge and to decrease toward the centre: It is not the propagating density waves observed in response to specific events, such as turning or shock.

3.3.1 Determination of spatial extent

We determine the spatial extent of simulated swarms using the α-shape method [4, 27], which allows for the presence of concavities within the swarm to the scale of α. A comparison between α-shape and convex hull border is provided in figure 3.3 as a general example. The α-shape of a set of points is as an extension of the convex hull. In two dimensions, its construction can be thought of intuitively with the following analogy. Take a coin and roll it along the edge of the point set, all the way around. If we draw a line between all of the points that we could touch with the coin, in the order they were visited, then we would have a curve which denotes the α-shape of the point set. The parameter α is related to the size of the coin used: a small coin would allow us to reach more points and a large coin would prevent our access to them. In the limit where the coin is infinitely large, we retrieve the convex hull [27]. As it approaches a point, the α-shape would effectively become the same as the point set. Therefore, it is clear that the α-shape can be more than one region, especially if there are large concavities in the group.

To measure density, individuals with distance less than δ from the border were removed and a new border of the reduced flock was computed. The reduced density was computed using this reduced volume and the number of internal birds. This process was repeated until the flock was empty (i.e. less than four members remaining such that no tetrahedra, and hence no volume, can be determined).

Simulated swarms typically have a non-negligible degree of concavity (as is also observed in the empirical study), therefore allowing for presence of a non-convex border is natural. Fixing the convexity scale α is non-trivial as we are not dealing with a few observations, but thousands of configurational snapshots per simulation,

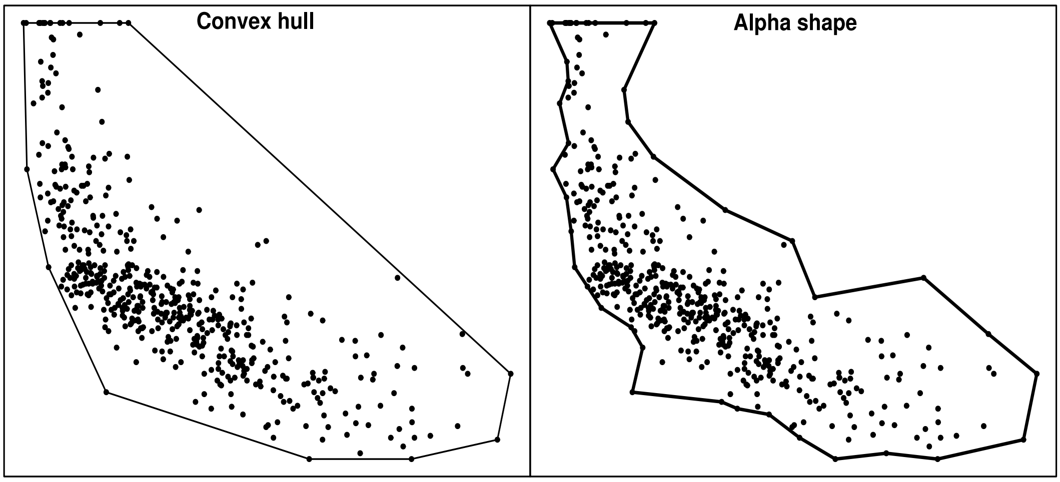

Figure 3.3: Two constructions of the border for an arbitrary set of points in two dimensions, convex hull (left) and α-shape (right). The region on the right has a smaller total area, but a higher number density, as the α-shape method allows the presence of some concavities, specifically up to the scale of α. Image adapted from Wikimedia Commons [23].

therefore we cannot do this manually (as is described in [16]). Instead we obtain a sensible estimate for α by selecting the smallest value possible that leaves the particle aggregation as a single connected component. This fixes the convexity scale throughout. We must also make a choice of the flock reduction parameter δ as this impacts on our measurement and ability to compare with the data. We select a value which on average provides a similar number of flock reduction iterations as the field study (which is 7).

3.3.2 Model fitting considerations

In order to prevent the choice of measurement variables from 3.3.1 from impacting our measurements we scale the reduction so that shell number is mapped to the domain $[0, 1]$ with 0 corresponding to the first reduction and 1 the final reduced flock. This also allows for a much easier comparison with the observational data; we can map that data to the same domain and perform cubic splines interpolation to allow query of comparison points between simulated and empirical data. Additionally we normalise the density data such that the first flock density measurement is 1, which makes our measurements and comparisons dimensionless, and allows us to look primarily at the *density gradient across the aggregation.* These transformations allow us to compare our simulation data more easily with the empirical data and to minimise the impact of possible differences in choice of parameters.

Our primary goal is to identify a bounding function f_κ that can produce simulations with density profiles that provide a good fit to the empirical data. There is some freedom in how one might parametrise f_κ. We choose f_κ to be linear in shell depth (parametrised via gradient a and intercept b). We allow the bounding strength on shell 0 individuals to be a separate parameter λ in order to include models in which individuals on the edge behave differently from the bulk.

We then use the Simultaneous Perturbation Stochastic Approximation (SPSA) algorithm [89, 91] for recursive optimisation of bounding function parameters (λ, a, b) using gain sequences with suggested practical values from [90]. We used the mean-squared difference between simulated and empirical data, averaged over a specified number of density evaluations, as the cost function estimate. Using this method allows for a principled stochastic search of the parameter space and can be performed in parallel. Fresh simulations were performed at each parameter update, due to the presence of hysteresis in these types of systems [22, 36].

SPSA is an optimisation algorithm that is able to perform gradient-descent though a parameter space, even when direct measurement of the gradient is not possible. It does this by estimating the local gradient by evaluating the cost function at a point close to the current point in parameter space (a small perturbation away) and at the point perturbed in the opposite direction too. All parameters are randomly perturbed simultaneously, thus instead of evaluating two points in each dimension of the space each iteration, only two points are needed each iteration independent of the dimensionality of the parameter space, making this approach potentially quicker than other methods of stochastic optimisation [91]. In our case, we do not have direct access to the gradient of the loss function (as chosen above), however we can measure it by running a simulation at specified parameters, and this estimate will be subject to noise. This situation is the design focus of the SPSA algorithm [91], so it is a suitable choice of approach to search for a model which will closely match the empirical data, especially as it is too computationally costly to grid search the full parameter space.

It is worth noting however, that it is not straightforward to estimate uncertainty of the resultant parameters as their values are the outcome of an optimisation process based on gradient descent. To do so would require a full understanding of the landscape of the parameter space, which we most certainly do not have here. If we did, we could ask questions about the uniqueness of the model found by the optimisation, and whether there is a large region of similarly close-to-optimal models near the one that was found. This is a drawback of the approach and can limit the understanding of the resultant parameters. However, if all we are interested in is

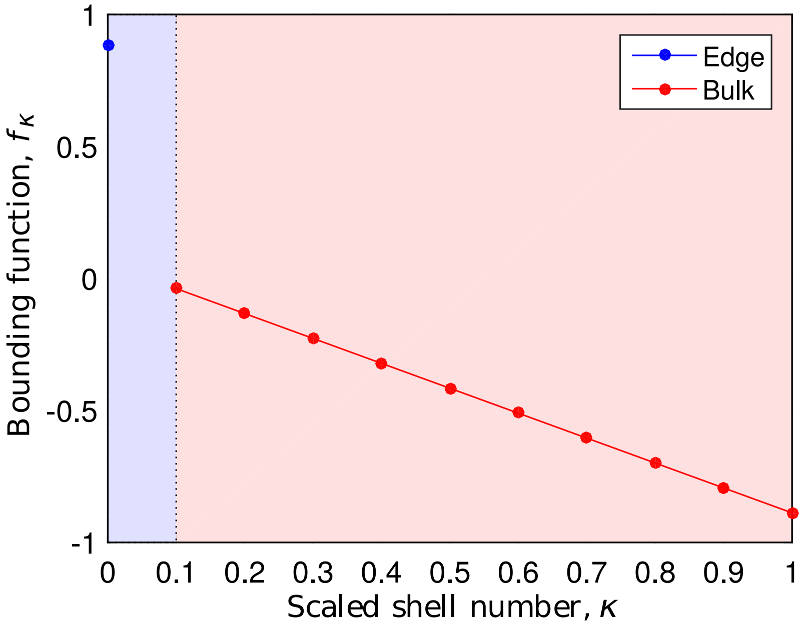

Figure 3.4: Distribution of motional bias via bounding function f_κ shown for parameters fit via stochastic optimisation: $\lambda = 0.883$, $a = -0.944$, $b = 0.056$. Example is shown for 11 shells: 0 to 10. Blue denotes the surface members, shell 0, whose motional bias is determined by λ, and red denotes members in the swarm bulk, with scaled shell number $0 < \kappa \leq 1$ and motional bias linearly parameterised by $a\kappa + b$.

finding a single model (set of parameters) which fits our data as closely as possible under the limits of the optimisation scheme chosen, then we can do so.

3.4 Realistic flock density distributions are observed

3.4.1 Model fitting outcome

In order to understand how the density across aggregation varies for swarms which interact in a metric-free fashion we generated simulations of our Distributed Motional Bias Strictly Metric-Free (DMBSMF) model, as described in § 3.3.2. As we are interested in simulating real-world behaviour we choose the parameters for the model via stochastic optimisation using the previously described method, directly fitting to empirical data, obtaining fit parameters of $\lambda = 0.883$, $a = -0.944$, $b = 0.056$. These parameters result in a bounding function f_κ as displayed in figure 3.4. This translates to a strong surface effect generally pointing toward the centre of the flock, however the bulk of the flock has an outward motional bias of increasing strength as one approaches the centre.

In order to simulate a flock that is comparable to that observed in the field study, we note from the motivating empirical study [4] that the flock in question contains $1,360$ reconstructed birds. We also note details from a later study [18](S.I.) for the flock in question: $1,571$ reconstructed birds with a measured polarisation of 0.96 ± 0.03 (i.e. observed flocks in high order regime). We therefore chose to simulate $1,500$ birds with noise parameter $\eta = 0.22$, yielding a polarisation of 0.931 ± 0.003, which is of similar magnitude to the observed flock. In each instance, we performed a simulation for $20,000$ time steps with the first $10,000$ steps discarded for equilibration of the system. The initial condition is a random (isotropic) orientation and a random location, uniformly distributed within a unit cube, for each individual. We measured the density variation across the flock (as described in § 3.3) every 10 time steps after equilibration, resulting in $1,000$ measurements per simulation instance, which are then time-averaged. We combine the results from five independent simulation instances, with final values presented as the mean of these quantities and uncertainties corresponding to standard errors.

3.4.2 Density variation across aggregation

The simulated model matches closely to empirical data of Starling flocks, as can be seen in figure 3.5, and produces the observed effect that aggregation density is greater at the border and reduces in what appears to be a linear fashion. The rate of this decrease is also closely matched. This counter-intuitive observation appears to require a model with a surprising motional bias: whilst surface birds move toward the flock centre, ensuring global cohesion, the rest of the flock move toward the border with increasing strength the further from it they are, as determined by topological depth. Naturally then, the number of birds closer to the border of the flock increases and drops off toward the centre due to the strong gradient of the bulk bounding function.

Our model shares some similarity with another recently proposed flocking model, the "hybrid projection" model [76], that drives individuals to move towards features in their visual field, specifically the boundaries between light and dark regions, where light/dark encodes the absence/presence of a neighbour in each direction. This model effectively encourages the movement inwards of individuals near the flock border. This is because individuals at the border will experience featureless outward-directed visual fields, resulting in an inward bias. It will also generate a bias outwards from the bulk of the flock as there will typically be more features in the outward-pointing directions than toward the often opaque centre of the flock. It is notable then that the motional bias that fits data from real-world flocks is similar to the effective motional bias present in visual models of this type.

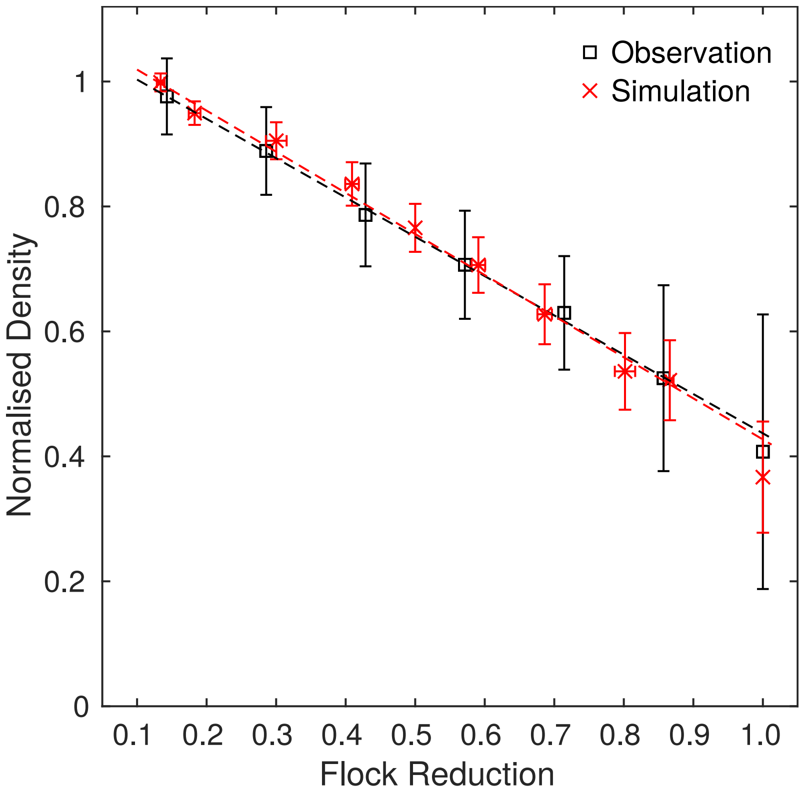

Figure 3.5: Density variation across aggregation: comparison of empirical data (black squares) reproduced from [4] with simulation data from DMBSMF model (red crosses) with parameters $\lambda = 0.883$, $a = -0.944$, $b = 0.056$ obtained via stochastic optimisation. Simulation data is an average of five time-averaged independent initialisations. Measurements are normalised such that the first flock reduction ($= 0$) has unit density, and a value of 1 corresponds to the final measurement before a fully reduced (empty) flock. Linear fits show good agreement with the model: flock density is largest on the border and decreases toward the centre at a similar rate.

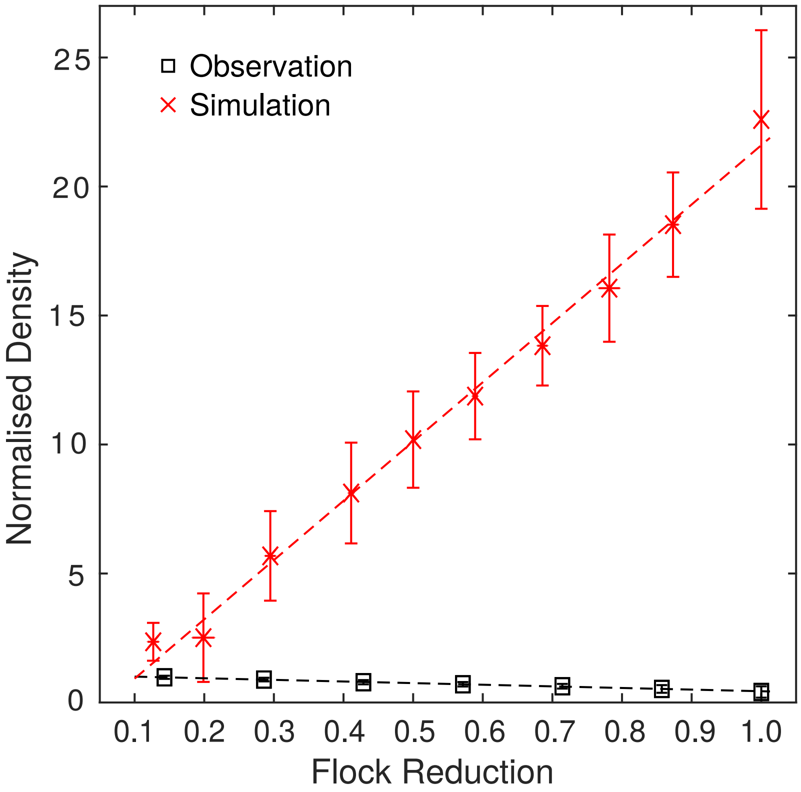

Figure 3.6: Density variation across aggregation: comparison of empirical data (black squares) reproduced from [4] with simulation data from SMF model (red crosses) with parameters $\lambda = 0.5$, $a = b = 0.0$, as in [75]. Simulation data is an average of five time-averaged independent initialisations. Measurements are normalised such that the first flock reduction (= 0) has unit density, and a value of 1 corresponds to the final measurement before a fully reduced (empty) flock. The large disparity between the SMF model and observations highlights the strength of our new DMBSMF model.

3.4.3 Comparison with SMF model

Recall the form of the interaction rules presented in § 3.2.3 with the bounding function as specified in equation 3.4. This recovers the SMF model [75]. This model can produce bounded swarms in free-space, however figure 3.6 reveals the density distribution to be quite different from empirical observations, and from our model too. The density is largest further from the border in this control case. The significant difference between the values obtained in our model and this control model provides strong evidence that the form of the bounding function is driving factor in determining a specified density distribution.

At this point it would be useful to gain some intuition on the typical morphology of these simulated swarms. Figure 3.7 shows specific instances of simulated swarms arising from the SMF model [75] and DMBSMF model (with SPSA fit parameters, present study). The local density profile for typical swarms generated by these models differs. In the figure, the DMBSMF swarm individuals look more uniformly distributed then for the SMF swarm, where a relative sparsity can be observed towards the edge. This qualitative difference between the structure of the two groups is reinforced by the quantitative measurement of group density, as shown in figure 3.6, which shows an order of magnitude variation across the group for the SMF swarm.

Real flocks of Starlings have a quasi-two-dimensional morphology, despite freedom in three-dimensions [4]. The plane of the flock also tends to be perpendicular to gravity, with group polarisation also tending to be perpendicular to gravity, i.e. flocks are extended in the plane of the ground and move parallel to it. Ballerini et al. [4] also found that there was no correlation between any dominant spatial axis of the flock and its direction of motion. Therefore, we can hypothesise that this morphology is driven by two factors: an energetic cost associated with motion in the direction anti-parallel to gravity and an absorbing boundary in the direction of the ground.

The simulated flocks which we consider have no such constraints. They are bounded by a motional-bias acting from the vertices of a convex polyhedron which surrounds the group. This defines the system as spherically symmetric, as without the aforementioned physical constraints, there is no broken symmetry in position, except that which is associated with the choice of polarisation direction [97]. In a simulated SMF flock bounded by an inward motional bias on its convex hull, we can also observe a spatial extension along the direction of motion, particularly in very highly ordered flocks. An example of this can be seen in figure 3.7 (top). This is associated with the fixed movement speed of the individuals as the strength of the motional bias is largest perpendicular to the polarisation of the group. This promotes an extension of the group over time in its direction of motion. Interestingly, an increase in noise arrests this elongation: an example of fluctuations in the system preventing it from exploring an undesirable state. The outward motional-bias present in our DMBSMF model also suppresses this elongation effect.

3.4.4 Flock characteristics

In this section we briefly present a few features of simulated DMBSMF swarms with SPSA fit parameters. Simulation parameters are $N = 1500$ and $\eta = 0.22$, initialised with uniformly random positions in a cube of specified density and randomly

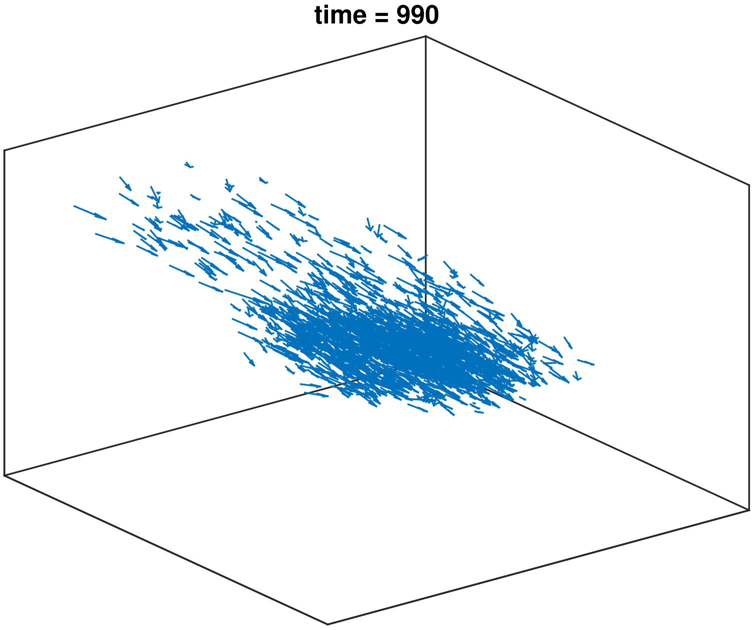

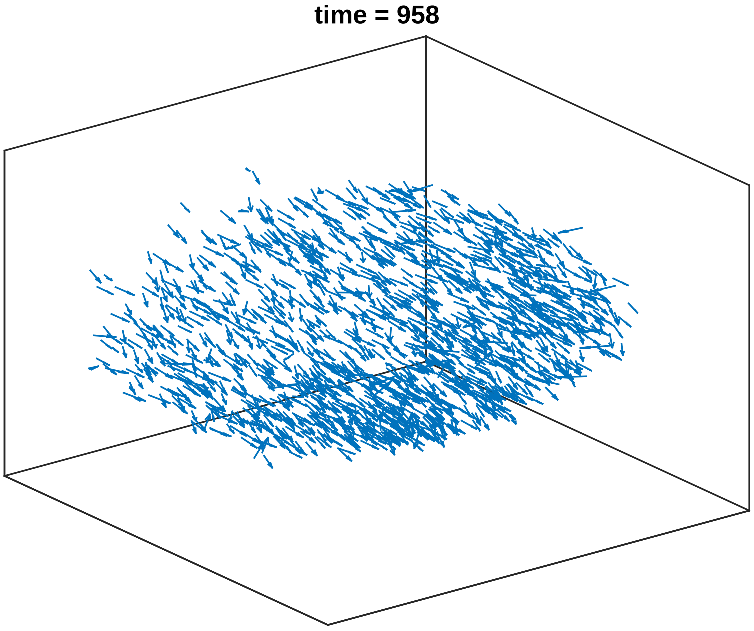

Figure 3.7: Configurational snapshots of simulated swarms: (top) SMF and (bottom) SPSA fit for our DMBDSMF model. We observe specific regions of high density in the SMF model, however in our model tuned with fit parameters these cannot persist and density variation across aggregation is regulated similarly to that observed in the empirical study [4].

distributed three-dimensional orientation.

Evolution of flock velocity

Figure 3.8 shows the fluctuation of the flock velocity which we define as $\underline{V}(t) = \frac{1}{N}\Sigma_{i=1}^{N}\underline{v}_i(t)$ (green). The system moves from a maximally disordered initial state ($P = 0$) to a highly ordered steady-state ($\langle P \rangle = 0.92 \pm 0.06$). The flock does not just settle on a heading an translate along it indefinitely; its orientation changes over time (spherical polar heading ϕ, θ in blue and red respectively). These fluctuations in group velocity are driven by the stochastic contribution of noise to the orientation of each individual in the flock.

Finite size steady-state

Figure 3.9 presents the evolution of the spatial extent of simulated for initial states with varying system size, from a cube of length 1 to 1000. Regardless of the initial state all of these swarms eventually result in a cohesive steady-state of consistent size. This is an important consistency check regarding the stability of the model fitted to empirical data.

3.5 Determining topological depth

3.5.1 Defining visual anisotropy

A key aspect of our model is the notion of topological depth within the flock. Individuals are assigned a shell number based on this quantity, encoding a non-metric measure of depth as the shortest path length from the individual to a member of the convex hull (shell 0). The motional bias experienced by this individual is a function of shell number, as shown in figure 3.4. It is therefore important to consider the accessibility of this quantity to the individual, from a biological/sensory perspective - how might flock members determine their shell number? In this section we present a model for how this could be achieved using the degree of anisotropy in an individuals visual field as an indicator of their depth within the flock.

We analyse a simplified model of the system in which the density is homogeneous, for simplicity. Consider the three-dimensional flock as a sphere S of radius R centred on the origin with particle mass distributed uniformly within this sphere. For a point P on or inside the sphere we can define an axis z along the vector from P to the sphere centre at the origin, as seen in figure 3.10. In spherical polar coordinates (r, θ, φ) this necessarily has φ-rotational symmetry about the z axis.

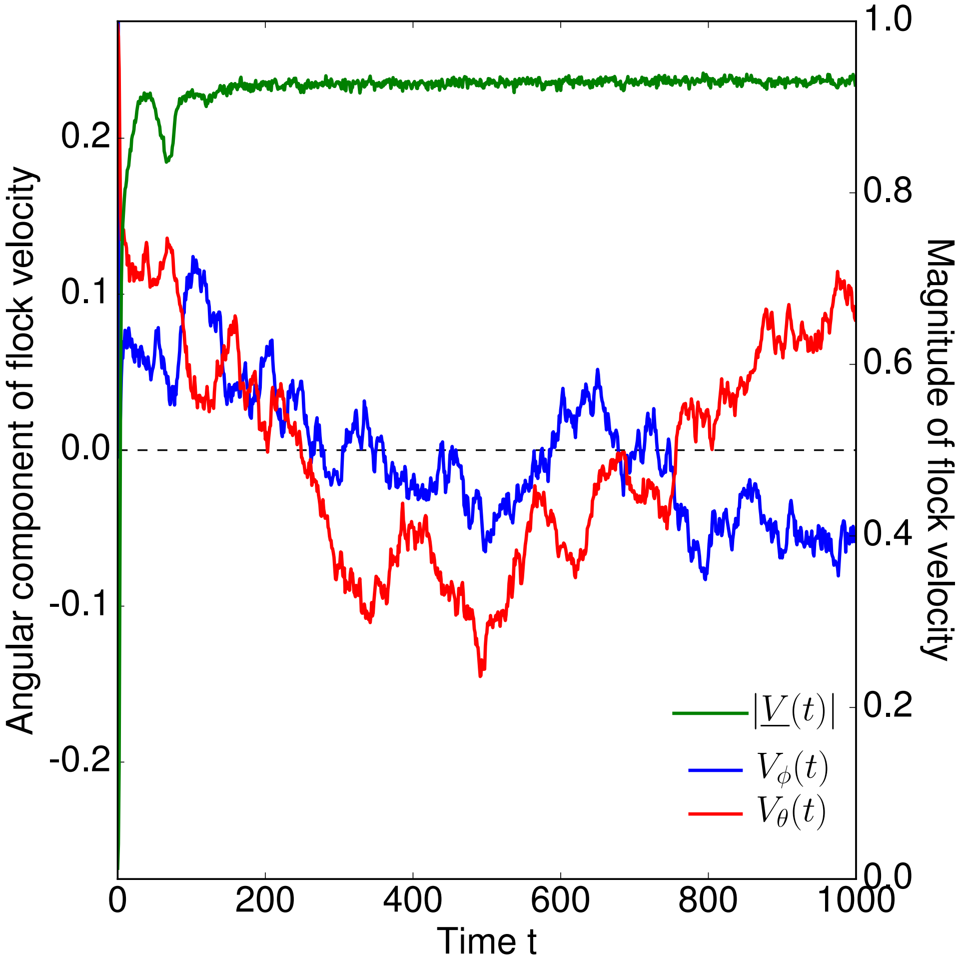

Figure 3.8: Change in flock velocity over time. Simulation with SPSA fit parameters, $\eta = 0.22$ and $N = 1500$, initialised with random positions, distributed uniformly, in a unit cube centred on the origin with random initial orientation, isotropically distributed. Flock velocity $\underline{V}(t) = \frac{1}{N}\Sigma_{i=1}^{N}\underline{v}_i(t)$ grows in magnitude (green line, right axis) from close to zero, a disordered state, to close to 1 ($\langle \underline{V}(t) \rangle = 0.92 \pm 0.06$), an ordered state. The angular components of $\underline{V}(t)$, described in spherical polar θ and ϕ, as $V_\phi(t)$ and $V_\theta(t)$ (blue and red lines, left axis) respectively, are shown to fluctuate in both ordered and disordered states, driven by noise of strength η.

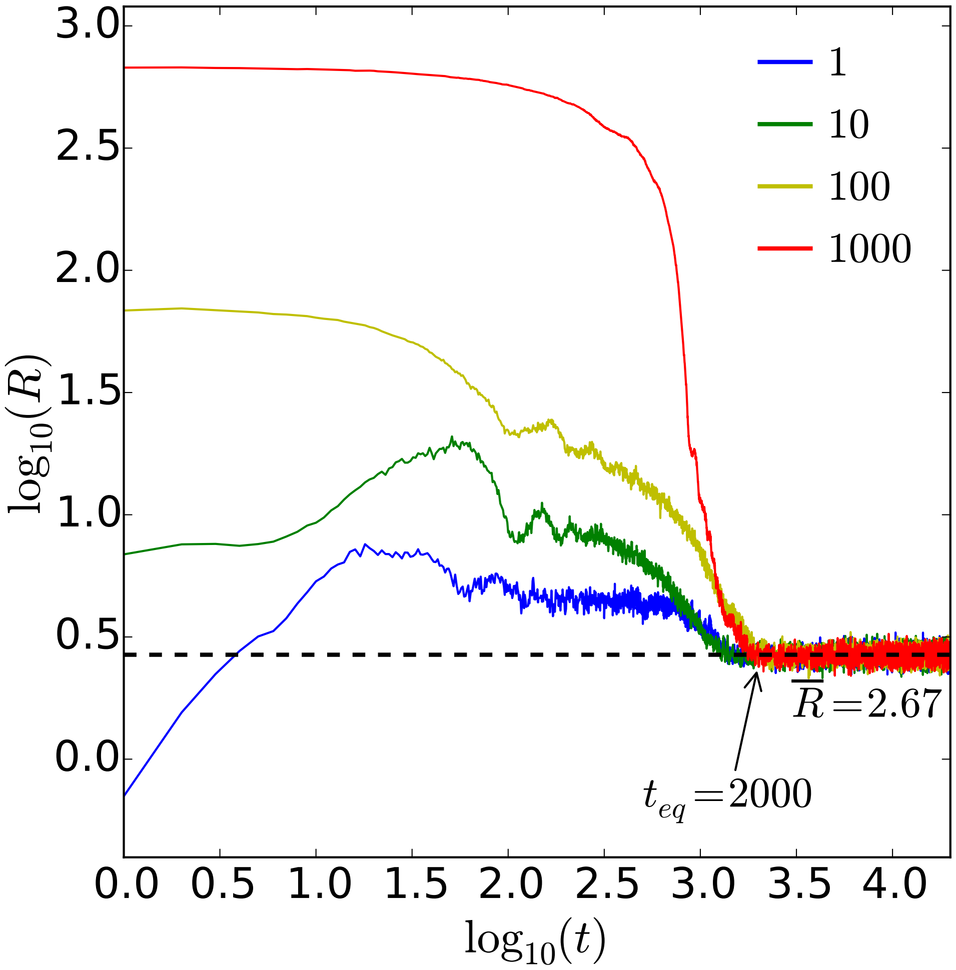

Figure 3.9: Convergence to steady-state. Simulation with SPSA fit parameters, $\eta = 0.22$ and $N = 1500$, initialised with random positions, distributed uniformly, in a cube of length l centred on origin with randomly distributed 3D orientation. Blue, green, yellow and red lines correspond to $l = 1, 10, 100, 1000$ respectively, increasing the spatial extent of the initial state. The spatial extent $R = \langle |\underline{r}_i - \underline{r}_{cm}| \rangle_{i \in C_0}$ converges to $\bar{R}$ after equilibration time t_{eq}. A steady-state is reached asymptotically.

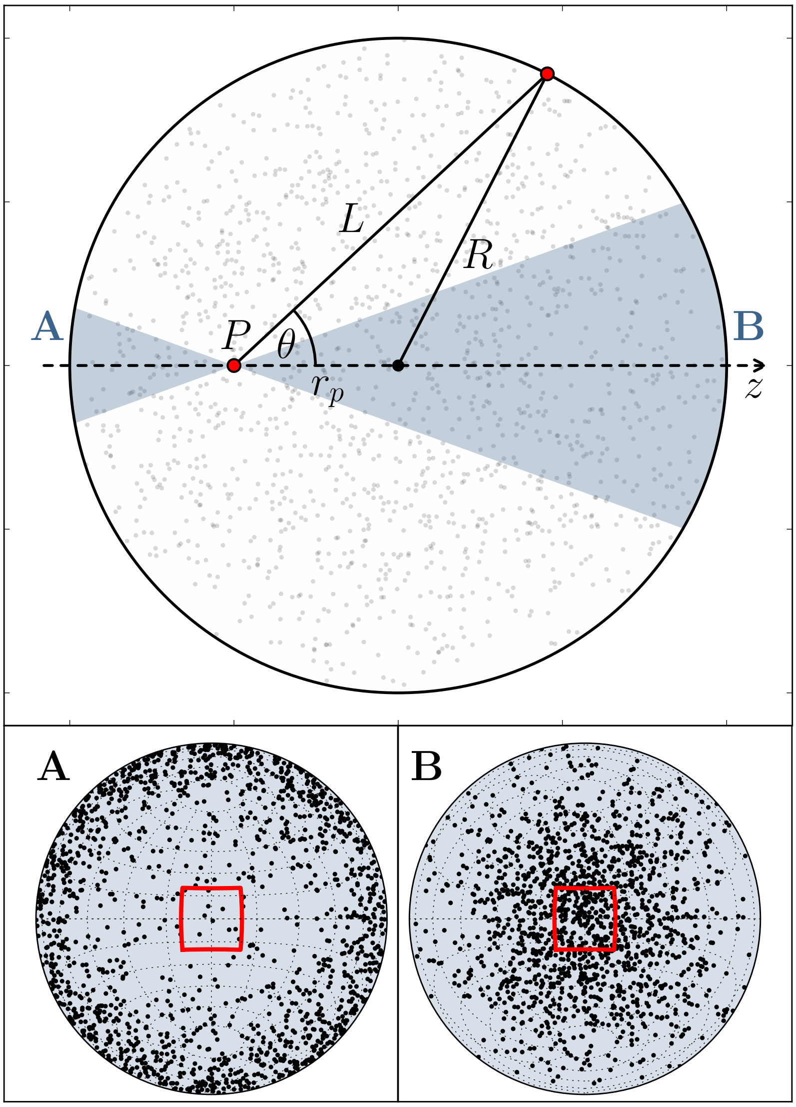

Figure 3.10: Schematic of simplified description of system: a cross-section of a sphere of radius R with homogeneous mass density $\rho(\underline{r}) = \rho$ for $|\underline{r}| \leq R$ and 0 otherwise. We consider the visual information available to an individual at point P at a distance r_p from the centre in different directions encoded by θ. $L(\theta)$ is the distance from P to the edge of the sphere in the θ direction. The system is symmetric under rotation about the axis z defined in the direction from P through the centre of the sphere. Areas A and B, shaded in blue, denote an example field of view between ±20 deg in the negative and positive z direction respectively. In the sub-figures A/B we plot the position of 1500 flock members relative to P, at $r_p = R/2$ from the centre, as Lambert azimuthal equal-area projections centred on the direction of negative/positive z respectively, with the red region denoting bounds of ±20 deg along each axis. Looking along z through the flock, as in B, one can see a high density of other flock members, however this is drastically reduced when looking in the opposite direction out of the flock, as in A. We use this visual anisotropy as the basis for an individual inferring its depth from deep within the flock.

The number of particles $N = \int_S \rho(\underline{r})\, dV$ constrains the density, here assumed homogeneous $\rho(\underline{r}) = \rho$. If we transform to the frame in which P as the origin, we can write:

$$N = \rho \int_S \tilde{r}^2\, d\tilde{r}\, d\Omega, \tag{3.5}$$

where $\tilde{r}$ is the radial component of a point in this frame and $d\Omega$ is the solid angle. Therefore,

$$\frac{dN}{d\Omega} = \frac{\rho L(\theta)^3}{3} := I(\theta), \tag{3.6}$$

which is the particle mass per solid angle, where $L(\theta)$ is the distance from P to the sphere surface. This quantity $I(\theta)$ is biologically accessible (i.e. can be sensed) via the visual field of an individual within the flock and is closely related (via a threshold function) to the fraction of sky occluded by individuals in the θ direction as observed from P.

For an individual at P there are intuitively directions which have higher and lower particle mass per solid angle. The imprint of the flock on an individuals visual field is greater when looking through its centre than in the opposite direction, as can be seen in figure 3.10, panels A & B.

We are interested in the extrema of $I(\theta)$ and make use of the observation that $L(\theta)$ is the radial distance to the flock edge, see figure 3.10, with P as the origin. This has the form $L(\theta) = r_p \cos\theta + \sqrt{R^2 - r_p^2 \sin^2\theta}$. To obtain the extrema of $I(\theta)$ we differentiate equation 3.6 which yields:

$$\frac{dI}{d\theta} = -\rho L^2 r_p \sin\theta \left(1 + \frac{r_p \cos\theta}{\sqrt{R^2 - r_p^2 \sin^2\theta}} \right) = 0\,. \tag{3.7}$$

For non-zero density ρ, there are a number of stationary points. First when $r_p = 0$, from the perspective of an individual at the centre of the spherical flock, there is no variation in mass density in any direction, and $I(\theta) = \frac{\rho R^3}{3}$ is independent of θ. More significantly, there is a maximum and minimum at $\theta = 0$ and π respectively. These correspond to $L(0) = R + r_p$, looking along a line from P through the centre of the sphere (along $+z$), and $L(\pi) = R - r_p$, away from it (along $-z$). This also provides two features identifiable in the visual field of the individual at P: $I_{\max} = \frac{\rho(R+r_p)^3}{3}$ and $I_{\min} = \frac{\rho(R-r_p)^3}{3}$.

To obtain a quantity which captures the asymmetry of any individual's visual field we take the ratio of the values of these two features to define the "visual anisotropy" ΔI as:

$$\Delta I = \frac{I_{\min}}{I_{\max}} = \frac{(1-D)^3}{(1+D)^3}, \tag{3.8}$$

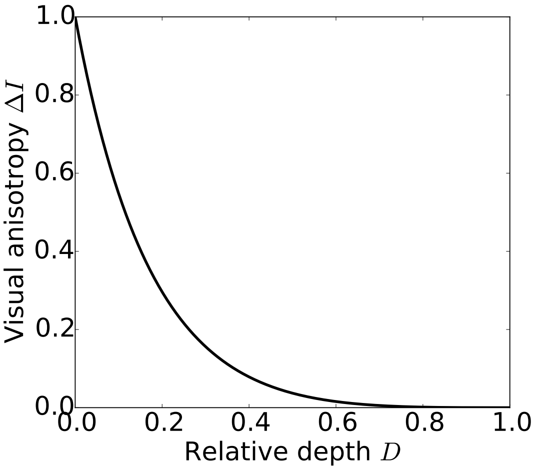

Figure 3.11: Analytic relationship between visual anisotropy ΔI and relative depth D as shown in equation 3.8. Data points from figure 3.12 are transformed by this function to obtain the relationship seen in figure 3.13.

where $D = r_p/R$ is the relative depth within the flock for an individual at P. The form of this is illustrated in figure 3.11

Note how equation 3.8 does not explicitly feature ρ and is "scale-free" by nature, being only a function of the dimensionless depth D, and is also monotonic on the interval $D \in [0, 1]$.

3.5.2 Connecting relative and topological depth

This formulation is useful if it can be linked to topological depth. To make this connection we now seek a relationship between relative depth D and topological depth κ. For each time-step for our simulated, non-spherical flocks (an example configuration can be seen in figure 3.7 (bottom)), we determine the spatial extent of the flock as $R = \langle |\underline{r}_i - \underline{r}_{cm}| \rangle_{i \in C_0}$ the mean distance to centre of mass $\underline{r}_{cm}$ over all particles on the convex hull of the point set. Relative depth per individual is then determined as $D_i = |\underline{r}_i - \underline{r}_{cm}|/R$ which, on average, is one for individuals with zero topological depth. Figure 3.12 shows relative depth averaged over a thousand configurations from five simulations with parameters determined from the fit to empirical data, as shown in figure 3.4, compared with the corresponding topological depth. We observe a linear relationship with relative depth decreasing with increased topological depth: when an individual is closer to the centre ($|\underline{r}_i - \underline{r}_{cm}|$ is smaller) it has a higher topological depth and vice versa.

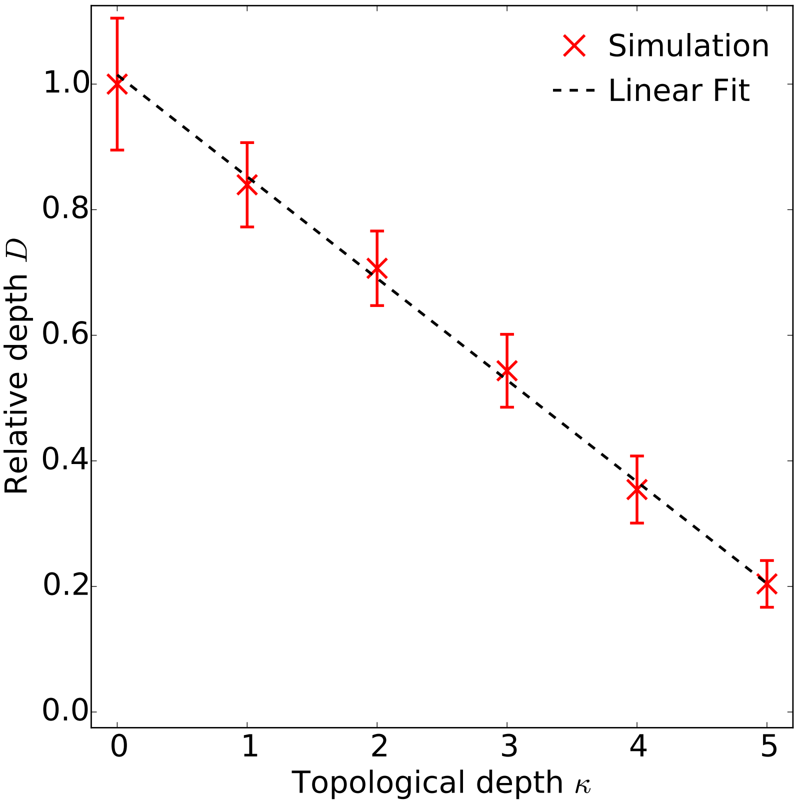

Figure 3.12: Relative depth D of an individual within a simulated flock compared to its topological depth κ averaged over five runs of 1000 time-steps after equilibration with $N = 1500$, $\eta = 0.22$ and bounding function as fit to empirical data (figure 3.4) shown as red crosses. Inverse squared-error weighted least squares fit shown as dotted black line: $D = -0.162\kappa + 1.015$. The D-intercept is close to 1, as expected since convex hull members have $\kappa = 0$, and are also the furthest from the centre of mass, thus $|\underline{r}_i - \underline{r}_{cm}| \approx R$ and so $D \approx 1$. If it is also true that the highest topological depth individuals are near the centre of mass, then the gradient of the fit must go as $1/\kappa_{\max}$. Since $\kappa_{\max}$ is 5 here, we would expect the gradient to be 0.2, which is close to our fit value.

3.5.3 Establishing the relationship between visual anisotropy and topological depth

We can finally relate our biologically accessible quantity, the visual anisotropy ΔI from equation 3.8, to topological depth κ and we show this for our model in figure 3.13, providing a one-to-one map. An individual can therefore compare two features (the minimum and maximum projected density) from their visual field in order to determine their topological depth within the flock, and hence understand how they should adjust their motion. One could imagine such a relationship might be determined heuristically: an intuitive understanding of depth within the aggregation from visual observations. When ΔI is small, the ratio between minimum and maximum of particle mass per solid angle $I(\theta)$ is large, so there is a large distinction between the two directions these represent (away from and toward the bulk of the flock respectively). When ΔI is larger the curve in figure 3.13 has less extreme slope and presents distinct values for different topological depths suggesting an individual deep in the flock still has capacity to determine its depth.

The relationship in figure 3.13 suggests that, for an individual in a group, they would need to have some estimate of the maximum topological depth κ possible for their group in order to calibrate their visual anisotropy curve with respect to it. Figure 3.14 shows how the maximum topological depth in an aggregation grows with the number of individuals N for the homogeneous spherical test case. Specifically it scales as $\kappa_{\text{max}} \sim N^{1/3}$. Considering that density $\rho = N/V$ for a spherical volume V implies $R^3 = \frac{3N}{4\pi\rho}$, then at a fixed density $R \sim N^{1/3}$, therefore $\kappa_{\text{max}} \sim R$. The maximum value of topological depth scales with the size of the flock. Therefore, an individual in such an aggregation would only need estimate the length scale of the group in order to use its visual field to determine its depth within the group. This length scale could be fairly easily estimated by, for example, relating it to the smallest projected size of other individuals it can see in the group, i.e. also using its visual information.

3.6 Conclusions

We have introduced a generalised topological model of collective behaviour with a tunable bounding function to distribute a metric-free motional bias across the swarm. This model was fitted to empirical data of Starling murmurations using stochastic optimisation to determine a suitable form of bounding function. Simulation data from this model was shown to match field study data and produce swarms which are more dense at the border than at the centre, which is a sur-

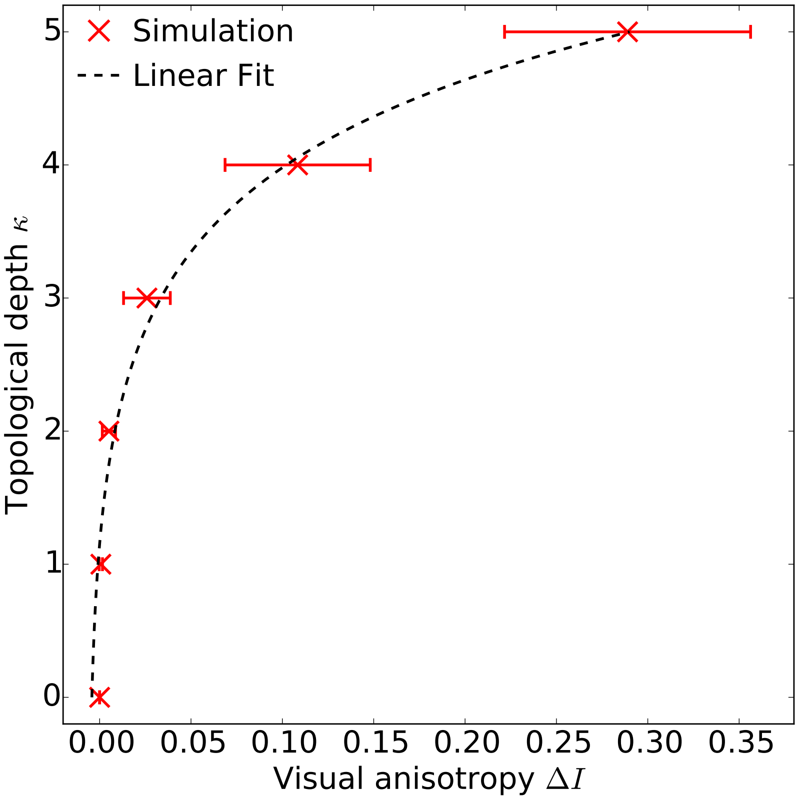

Figure 3.13: Relationship between visual anisotropy ΔI and topological depth κ. Simulation data (red crosses) is as for figure 3.12 and unweighted fit (black dashed line) of form $\kappa = ae^{b\Delta I} + c$ is provided as a guide-line ($a = 0.002$, $b = 1.005$, $c = -0.006$). The functional form is not itself important but is designed to show that a simple heuristic relationship could be accessible to animals.

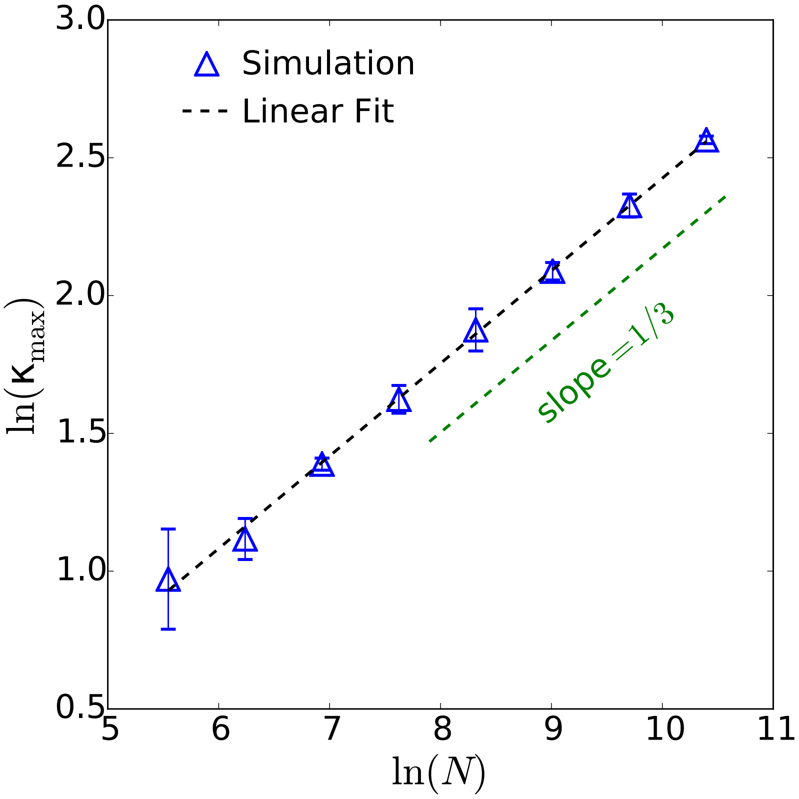

Figure 3.14: Scaling of maximum topological depth $\kappa_{\max}$ with the number of flock members N for the test case of a homogeneous sphere of unit density (blue triangles). Fit function (black dashed line) has the form $\ln(\kappa_{max}) = 0.336\ln(N) - 0.933$ which suggests $\kappa_{\max} \sim N^{1/3} \sim R$, as one might expect at fixed density. The dashed green line has gradient 1/3, for reference. Thus maximum topological depth grows with the size of the flock.

prising characteristic of real-world Starling flocks. We compared this fitted model to a benchmark topological model with no motional bias on the bulk of the flock (only on the surface). This allowed us to understand the role of the specific form of distributed motional bias that we have identified, which is to produce the desired level of inter-individual exclusion across the swarm, and allow individuals to keep the necessary relative distance apart without directly enforcing what this should be.

We also proposed how an individual might use the observed anisotropy of its visual field to determine its depth within the flock. The analysis presented here is restricted to the simple case of a homogeneous sphere therefore there does exists scope to potentially extend to this approach to explore the role of heterogeneity in both density and flock morphology. From a biological perspective, there many situations where there is individual benefit from being able to sense depth within an aggregation, beyond that which might inform individual dynamics within a moving flock. Safety is of the individual by screening risk of predation using its neighbours (the selfish herd hypothesis) would require some idea of where the group centre is, relative to their current position, in order to occupy it. Moving away from birds and toward insects, it has been observed that the trajectory of individual midges within stationary (i.e. without high group order) swarms are as effectively free particles [48]. They do not stay in one part of the swarm but explore its space [83] and it has been suggested this behaviour could be motivated by the search for a mate. This sort of motion appears to require some understanding of depth. Their primary information stream is acoustic in nature, rather than visual as we have considered here, however it is still a long-range stimulus [82] so a similar argument may be possible for this system too.

Models of swarming generally aim to obtain group cohesion and co-alignment [43, 84]. Typically, these are explicitly included as rules imposed on the interacting agents in the system. Our model differs from current models in the literature. While it explicitly imposes co-alignment in a familiar way, swarm cohesion (and density regulation) are controlled using a motional bias distributed across the flock, which is prescribed via metric-free interaction rules, consistent with experimental observations. We show that specific field observations of density variation in aggregations of Starlings can be reproduced using our model so that density is higher on the border of the flock than at the centre. This density profile may relate to the predator-evasion mechanisms of three-dimensional swarms and the evolutionary development of such behaviour.

Chapter 4

Seeking marginal opacity is sufficient to induce alignment in swarms

In the preceding chapters we have seen how swarming rules, specifically co-alignment between topologically assigned neighbours, can generate highly ordered artificial swarms. The aligning interaction between nearby individuals propagates information of the specific group heading, individual by individual, allowing distantly separated group members to go in the same direction, in spite of the distance between them and even the presence of noise. We have shown how to obtain a specific group density, or density distribution across the group, in the presence of the topological constraint and this sort of aligning interaction.

In chapter 2 we found how temporal information can be used to help achieve a cohesive, aligned group. In chapter 3 we establish the importance of visual information for certain types of animal group and explore how it can be used by group members to move within the group. We build on these themes in the following chapter, combining both temporal and visual information to generate a cohesive, ordered group with strongly correlated behaviour without the need for traditional, explicit aligning rules to produce swarming.

4.1 Introduction

A striking observation of real-world flocks of Starlings is that they appear to be in a state of marginal opacity [74, 76]. This means that, for a bird within the group, they will see about half of their view occupied by other members of the group and the rest will be the environment (i.e. the sky and surrounding landscape). From an evolutionary perspective this can be particularly beneficial as individuals inside the group are still able to look out and contribute to threat detection (recalling the "many eyes" hypothesis introduced in § 1.1.2). This sets the global density naturally, as if two birds are very close to one another they will contribute dramatically to occluding one side of each others view, but if the average spacing between birds is too low then the apparent size of each other flock member will be vanishingly small. It has not however been established if the state of marginal opacity observed is a consequence of interactions between elements of the flock or whether it is established at the individual level that this state is desirable (through say, evolutionary instinct) and hence sought out. Pearce et al. [76] show how this state can be produced by a model in which individuals focus on the features in the scene that they can observe, comprised of the projected positions of other members in the group. The approach we consider will be the converse hypothesis: marginal opacity to generate swarming, rather than swarming rules to generate marginal opacity.

In this chapter, we introduce a model of collective behaviour in which individuals determine the expected local opacity they will observe after time τ has elapsed conditional on where they might turn. They compare this with a specified desired opacity in order to update their motion. Broadly, the rule imposed on all individuals homogeneously is "seek desired opacity". There are no explicit two-particle alignment or cohesion interaction rules, only the opacity target. There are also no fixed boundaries. Despite these challenges, we will show that this behaviour can induce alignment in the swarm and even keep it cohesive. We will show how individual behaviour is locally correlated, even though this model is specifically non-local, and also discuss how this effect is generated.

4.2 Model outline

We begin by defining the projection of the swarm onto the individuals field of view which we term the "visual field" of that individual. We will then present the rules describing the model dynamics and the procedure of numerical simulation used to study the model.

4.2.1 Defining the visual field

Figure 4.1 shows a schematic representation of the visual projection of surrounding group members onto the field of view for a specific individual i. We use this projection to define the "visual field" for an individual as follows.

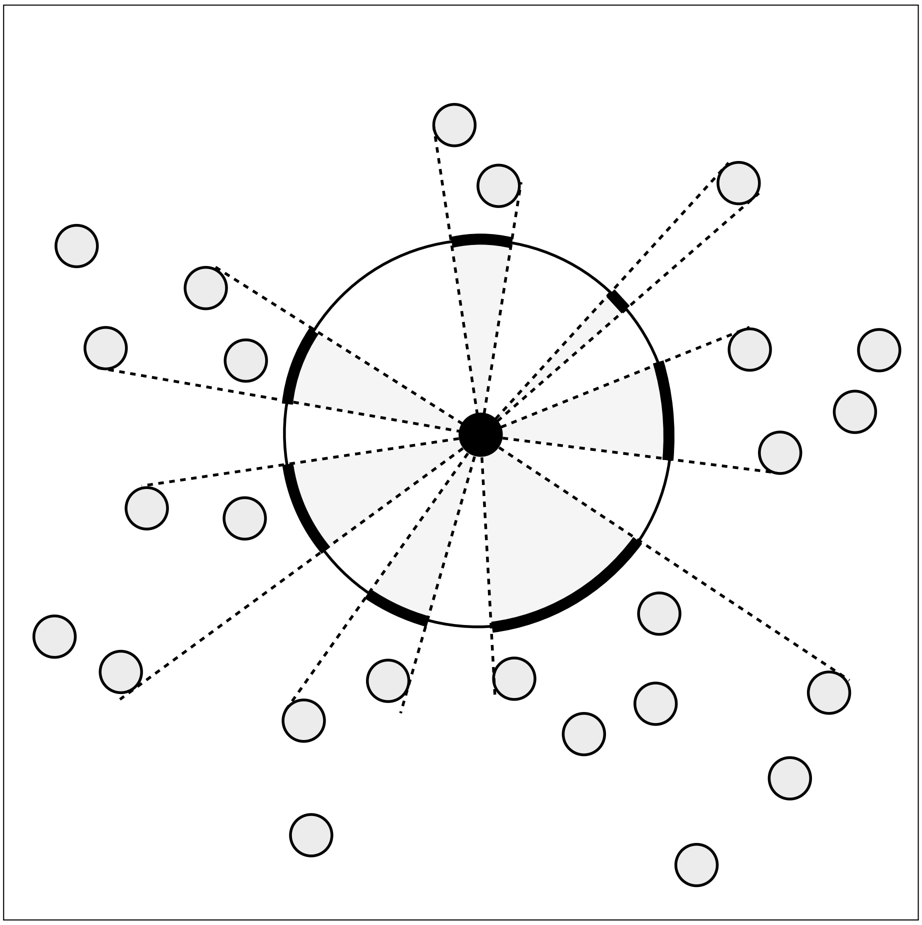

Figure 4.1: Schematic construction of the visual field of i (black circle) $\mathcal{V}_i(\theta)$ in two-dimensions. Where there is dark, there is a particle in the group blocking view in that direction. Otherwise, i can look out of the flock, corresponding to a light region. $\mathcal{V}_i(\theta)$ is therefore a discontinuous binary function (dark:1, light:0).

In two-dimensions, the visual projection corresponds to identifying intervals of polar angle subtended for each other individual j in the group at time t. The width of this interval is the angular radius of j with respect to i, that is $\alpha_{ij}(t)$:

$$\alpha_{ij}(t) = \sin^{-1}\left(\frac{b}{|\underline{r}_{ij}(t)|}\right), \tag{4.1}$$

where $\alpha_{ij}(t)$ depends on the actual particle size, which are two-dimensional disks of radius b, and the distance between the two particles via $\underline{r}_{ij}(t) = \underline{r}_j(t) - \underline{r}_i(t)$, and where $|\underline{w}|$ obtains the magnitude of vector $\underline{w}$. If $|\underline{r}_{ij}(t)| \leq b$ we set $\alpha_{ij}(t) = \pi/2$, as particles are not explicitly prevented from overlapping.

Note that, in three-dimensions this would correspond to projected spherical caps as the contribution for each visible particle. This extra degree of freedom makes interval merging much more difficult practically, as has been discussed by Miller [62]. In what follows, we work in two-dimensions, for simplicity, though a three-dimensional extension can be naturally defined too.

The angular radius of particle j is used to define an interval of θ which is occluded by j, for each of the other particles in the group. For j this is $[\theta^-_{ij}, \theta^+_{ij}]$, where $\theta^{\pm}_{ij} = \theta_{ij} \pm \alpha_{ij}(t)$ and θ_{ij} is the polar angular component of $\underline{r}_{ij}(t)$.

These are merged to obtain a binary description of projected neighbour positions for i. We call this construction the *visual field* $\mathcal{V}_i(\theta, t)$ of particle i at time t, which is a discontinuous binary function on the polar domain $\theta \in [-\pi, \pi)$:

$$\mathcal{V}_i(\theta, t) = \begin{cases} 1 & \text{if occluded along } \underline{\hat{u}}(\theta) \\ 0 & \text{otherwise} \end{cases}, \tag{4.2}$$

where $\underline{\hat{u}}(\theta)$ is a unit vector of polar angle θ originating at $\underline{r}_i(t)$.

Algorithmically, for particle i, this construction is performed starting with the nearest neighbour j as it is certainly not occluded, and its projection would have the largest individual contribution to $\mathcal{V}_i(\theta, t)$. At this point, $\mathcal{V}_i(\theta, t)$ is a single interval $[\theta^-_j, \theta^+_j]$, taking care to split at the polar discontinuity at $\pm\pi$ where necessary. We then work outward from i, going to the next nearest neighbour. We check if each is occluded, and if so whether that occlusion is full or partial. Full occlusion means no contribution to the visual field. Partial occlusion means that the new interval must be merged with the previous intervals that comprise $\mathcal{V}_i(\theta, t)$. If no occlusion at all, then a new interval is created and appended to $\mathcal{V}_i(\theta, t)$. This process is repeated for all other $j \neq i$ in the group, resulting in the full visual field of particle i at time t.

The speed of this process can vary widely between best and worst case. The pairwise distance from each point to all other points is needed which has complexity $\mathcal{O}(N^2)$. For a specific particle i, other group members j need to be sorted in distance from i, thus $\mathcal{O}(N \log N)$ for this process. Interval merging is generally similar as $\mathcal{O}(k \log k)$ where k is the number of intervals being merged: for a sorted list of intervals, merging is linear time. The worst case then corresponds to a sparse group, such that every other group member requires an interval to be added to the $\mathcal{V}_i(\theta, t)$ and no intervals are merged, though for each neighbour each preceding interval needs to be checked, which would be $\mathcal{O}(N^2)$. The best case corresponds to a very dense group: two equidistant individuals at opposite sides of i such that the three are on a line, overlapping, at distance b (the particle radius) away. All other $N-3$ individuals are necessarily occluded and a minimum number of intervals are present to check over, which would be $\mathcal{O}(N)$. Generally, if k_m is the median number of intervals, then for each particle i there would be typically k_m checks through intervals for each neighbour j. As we build the interval list we can keep it sorted to avoid a sorting step, thus typical complexity for each particle i is $\mathcal{O}(Nk_m)$.

4.2.2 Defining the local opacity

Given $\mathcal{V}_i(\theta, t)$ there is much scope in which information we can use. In general, we can describe the structure of the visual field, a discontinuous binary function, by decomposing it into Fourier basis of sines and cosines. This would allow us to pick out specific structures on this domain and dominant regions of projected neighbours. In this work, we concern ourselves with only the lowest order information in $\mathcal{V}_i(t)$, namely the proportion of the total visual field which is covered. We call this the local opacity $\Omega_i(t)$:

$$\Omega_i(t) = \frac{1}{2\pi} \int_{-\pi}^{\pi} \mathcal{V}_i(t). \tag{4.3}$$

Algorithmically, this corresponds to summation over merged interval widths that define $\mathcal{V}_i(t)$. The contribution of each will be its arc length on the unit circle. This is normalised by the full circle perimeter 2π, thus $\Omega_i(t) \in [0, 1]$.

4.2.3 Model outline

The rule set for the motion of particle i is:

$$\underline{v}_i(t + \delta t) = v_0 \vartheta \Big\{ (1 - \eta) \underline{\mu}_i(t) + \eta \widehat{\underline{\xi}}_i(t) \Big\}, \tag{4.4}$$

$$\underline{r}_i(t + \delta t) = \underline{r}_i(t) + \delta t \underline{v}_i(t), \tag{4.5}$$

where δt is the size of the discrete time step and v_0 is the fixed speed of the particle. The operator $\vartheta(\ )$ performs normalisation via $\vartheta(\underline{w}) = \underline{w}/|\underline{w}|$. The stochastic term in equation 4.4 is comprised of a parameter η that denotes the strength of the noise applied to each particle. The term $\widehat{\underline{\xi}}_i(t)$ is a random unit vector obeying $\langle \widehat{\underline{\xi}}_i(t) \rangle = 0$ and $\langle \widehat{\underline{\xi}}_i(t) \cdot \widehat{\underline{\xi}}_j(t') \rangle = \delta_{i,j}\delta_{t,t'}$. The schematic in figure 4.2 illustrates this process.

The specific contribution of opacity in our proposed model is controlled by the form of $\underline{\mu}_i(t)$:

$$\underline{\mu}_i(t) = w(\Omega_i^L(t+\tau))\widehat{\underline{v}}_i^L(t) + w(\Omega_i^R(t+\tau))\widehat{\underline{v}}_i^R(t), \tag{4.6}$$

which is a linear combination of two orientations, $\widehat{\underline{v}}_i^{L/R}(t)$, each weighted by a function of local opacity, $w(\Omega) \in [0,1]$:

$$w(\Omega) = 1 - 2|\Omega - \Omega_{des}|. \tag{4.7}$$

The form of this acts to penalise deviations of local opacity from its desired value Ω_{des}. This function is maximal when $\Omega = \Omega_{des}$ and the requirement of marginal opacity sets $\Omega_{des} = 1/2$. Also the L/R orientations, corresponding to a left/right turn by $+\gamma/-\gamma$ respectively are given by rotation of the current orientation $\widehat{\underline{v}}_i(t)$ by those angles:

$$\widehat{\underline{v}}_i^{L/R}(t) = \mathcal{R}(\pm\gamma)\widehat{\underline{v}}_i(t), \tag{4.8}$$

where $\mathcal{R}$ is the two-dimensional unitary rotation operator. Then, $\Omega_i^{L/R}(t+\tau)$ is the local opacity computed after all particle positions have evolved ballistically based on the current state for τ time ahead. However for particle i its orientation is replaced by $\widehat{\underline{v}}_i^{L/R}(t)$ as such local opacity is computed at a proposed left/right position in the future.

In short, $\underline{\mu}_i(t)$ in equations 4.4 and 4.6 is a combination of turning to the left and right, each weighted by a factor that specifies how close to the desired opacity the local opacity is, in those directions, at time τ in the future. In the schematic in figure 4.2 that shows this process, the right state is closer to $1/2$ opacity than the left state, which results in the new velocity (in blue) to be more in the right-hand direction. In this way, particles can move to seek this desired marginal opacity at time horizon τ.

4.2.4 Experimental setup

The model with interaction rules in equations 4.4 and 4.5 is numerically simulated in two dimensions with an implementation in C++. A system of N particles is

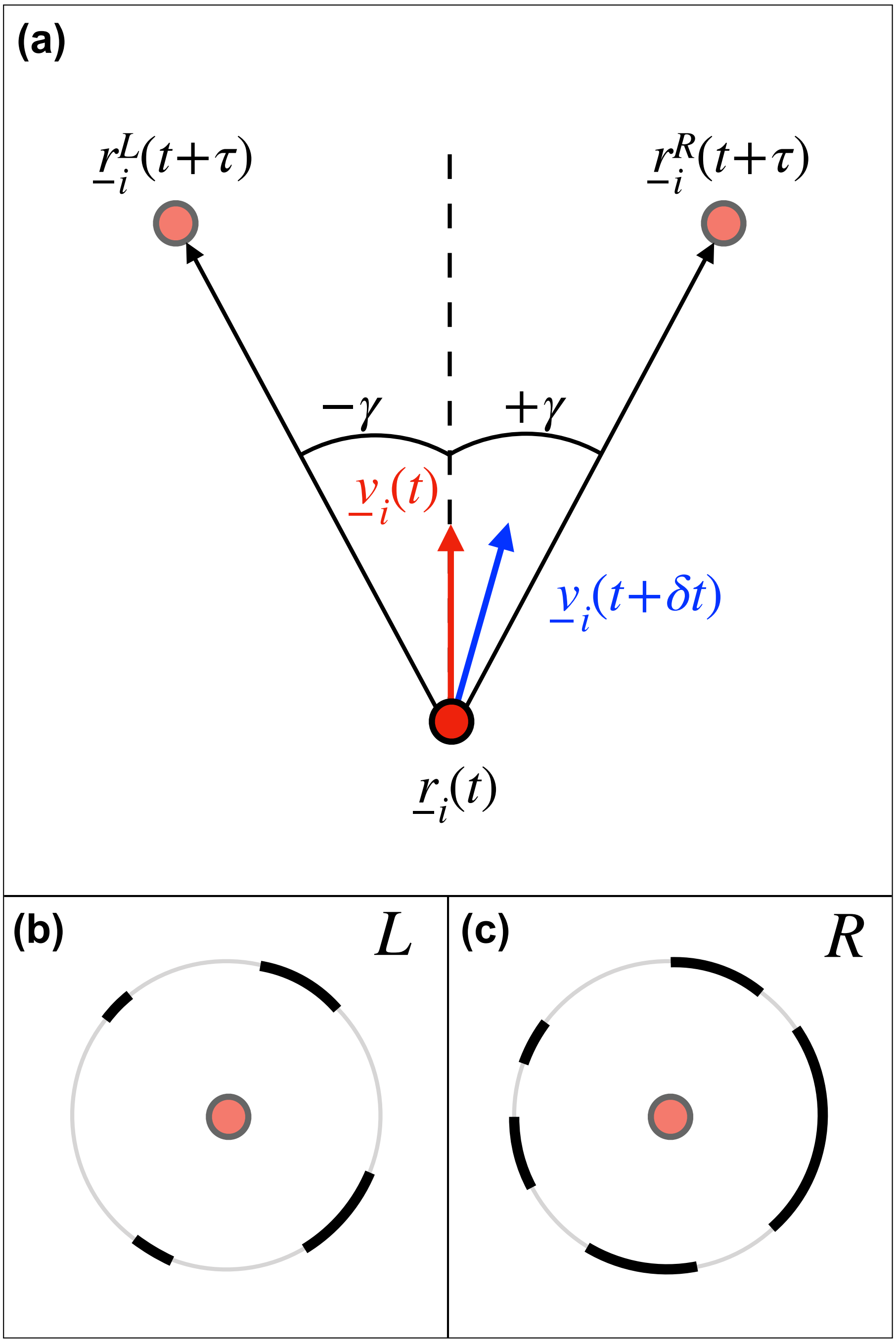

Figure 4.2: (a) Schematic showing how particle i (red) "looks forward" to the time horizon τ, and moves towards states which are closer to the desired marginally opaque state. This is shown here for the case of no noise, i.e. the case of $\eta = 0$ in equation 4.4, thus reduced to $\underline{v}_i(t + \delta t) = v_0\widehat{\underline{\mu}}_i(t)$ shown here. Lower panels show the visual field observed after the left (b) and right (c) turn choices (rotations of $\underline{v}_i(t)$ by $-\gamma$ and $+\gamma$ respectively) after τ timesteps $\underline{r}_i^{L/R}(t+\tau)$, constructed as shown in figure 4.1. The visual field in (c) is closer to the desired opacity, thus particle i updates its velocity to $\underline{v}_i(t + \delta t)$, which is rotated more toward the right (blue).

initialised uniform randomly across a circle centred on $(0, 0)$ with initial density ρ_{init} and no overlap, and uniformly distributed random orientation. Individuals move in continuous space at a fixed speed v_0 and their state is updated in discrete time steps of δt, which are both set equal to unity in the following. This defines the simulation length scale as $v_0/\delta t = 1$. Control parameters are the strength of noise η and the time horizon τ. The system evolves for T time steps in total. The first T_{eq} of these are discarded to allow the system to equilibrate and lose the features of its initial condition. To compute swarm statistics the relevant values are averaged over the window $[T_{eq}, T]$ denoted $\langle \dots \rangle$ in the following.

There are natural choices for the remaining parameters introduced here. We set b to 1, defining the particle radius as the same as the simulation length scale. We also set turning angle γ to 45^o, which makes the left and right turns orthogonal to one another, providing maximal span for the resultant linear combination that makes up the new heading, as defined in equation 4.6.

It is worth considering the complexity of the algorithm. We have discussed the complexity of constructing the visual field for each particle i in § 4.2.1. This is done for each of the N particles twice at each time step: once for each of the proposed future states. This is complexity $\mathcal{O}(N^2 k_m)$ for a median number of intervals of k_m, which has worst case of $\mathcal{O}(N^3)$.

4.3 Requiring marginal opacity implicitly generates group alignment

4.3.1 Group polarisation

As has been established, this model does not have any explicit inter-particle alignment terms in its interaction rules, shown in equations 4.4 and 4.5. In traditional models of collective behaviour [32, 102], macroscopic alignment is a direct result of microscopic aligning interactions. Therefore, we first investigate the ability of our model to generate a globally aligned state.

In figure 4.3, at a low/moderate value of noise ($\eta = 0.15$), we show how increasing the time horizon over which the future marginally opaque state is aimed for increases the level of order in the flock. Low values of τ do not produce aligned flocks as the left and right future paths do not have sufficient discrimination between their visual state. Increasing τ rectifies this is an apparent continuous fashion. At around $\tau = 11.0$ the system is able to achieve a mean polarisation of around 0.8 which is an ordered state, and levels off at a mean polarisation close to 0.9.

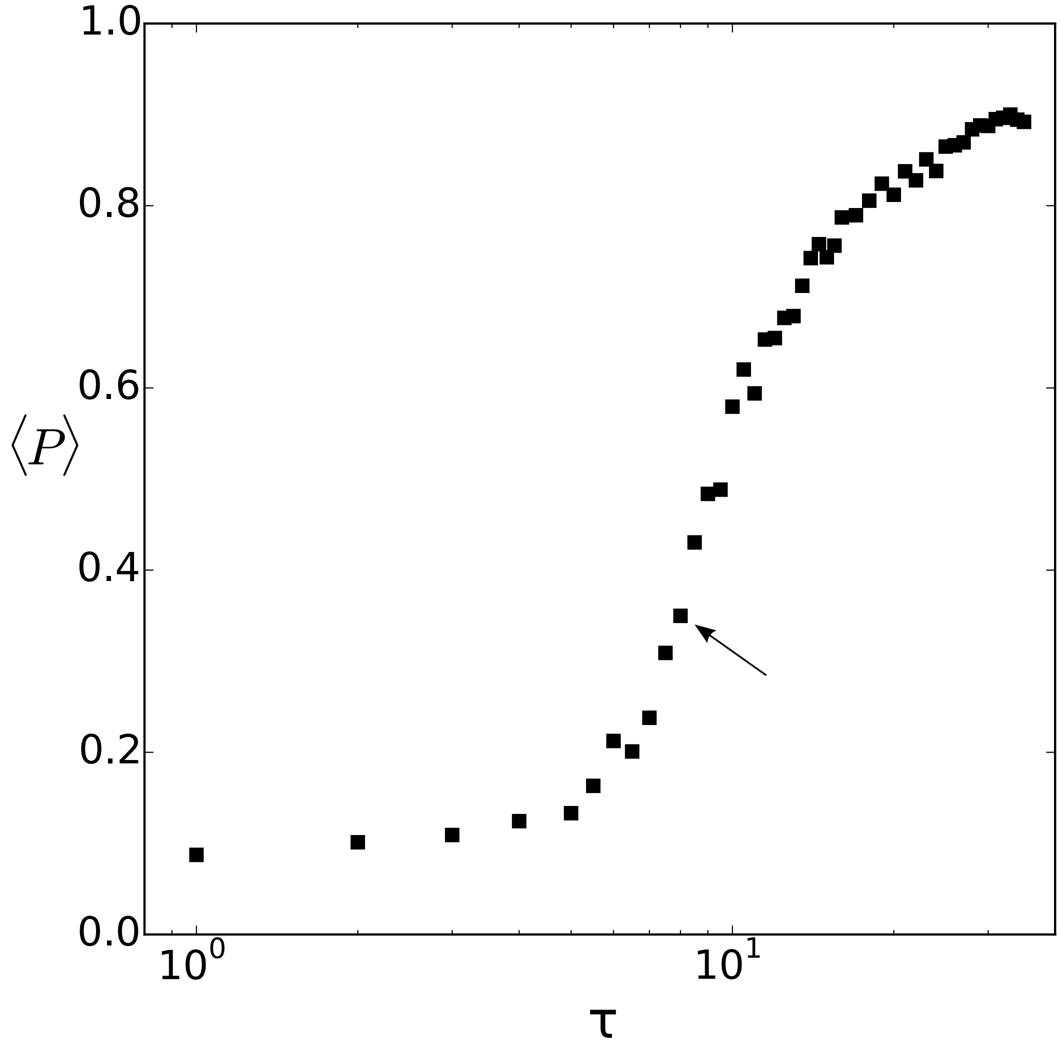

Figure 4.3: Variation of time-averaged order parameter $\langle P \rangle$ with time scale τ for a system of $N = 100$ particles at $\eta = 0.15$ and $\rho_{init} = 0.005$. Group order increases from disorder (low $\langle P \rangle$) to an ordered state ($\langle P \rangle$ close to 1). Arrow indicates point of maximal variance, as determined in figure 4.4.

The overall change in polarisation, the order parameter of the system, reminds of a continuous phase transition of the type observed in ferromagnetic systems, and discussed in § 2.3.1. We observe this sort of behaviour in models presented in Chapters 2 and 3, as these are based on the topological Vicsek model [34] discussed therein. This is a surprising similarity as, in those models we prescribe alignment directly between topological neighbours, but here we do not.

In order to scrutinise the behaviour across transition from the disordered, low τ state to the strongly ordered, high τ state, in figure 4.4 we present the change in variance across the same domain. This is proportional to the susceptibility in the ferromagnetic analogue mentioned, which characterises the systems linear response to external perturbation, which relates proportionally to the fluctuations in order of the system. This can be seen to grow sharply toward a peak at $\tau = 8$, as designated by the black arrow, before rapidly decreasing after this point. This qualitatively agrees with the expected behaviour across the transition region from the ferromagnetic analogue.

Notably, the variance grows once more as τ is increased to large values. This is quite surprising as the system is in a highly ordered state in this region, as can be seen in figure 4.3. The source of these fluctuations is not yet clear though could be related to an instability in coherence between the current and future visual states, as discussed in § 4.3.2 below.

4.3.2 Cohesion and local opacity

In addition to group polarisation it is important that the group be cohesive as we are simulating swarming in open boundary conditions. As the basis for the interaction is based on opacities we would expect this to be the case, as discussed in [76] and 4.1; flock spatial extent and opacity are coupled by the size of the individuals in the group b and since we are seeking a specific value of opacity ($\Omega_{des} = 0.5$), cohesion should be assured if group members are achieving this goal.

Figure 4.5 shows the convergence of the local opacity, averaged over the ensemble of swarm members, to the desired marginally opaque state over time. The flock begins in a more dense, higher opacity state (green in figure) before decreasing in opacity towards the $\Omega_{des} = 1/2$ marginally opaque region. The inferred future mean local opacity to the left/right (blue/red in figure) also follow this trend and actually settle closer the desired opacity. This is because the future visual state is the one that is being optimised for, not the current one. The current opacity settling in a similar region, although slightly higher, is a only a consequence of the future state convergence. It can be seen in the figure that the left and right states, which

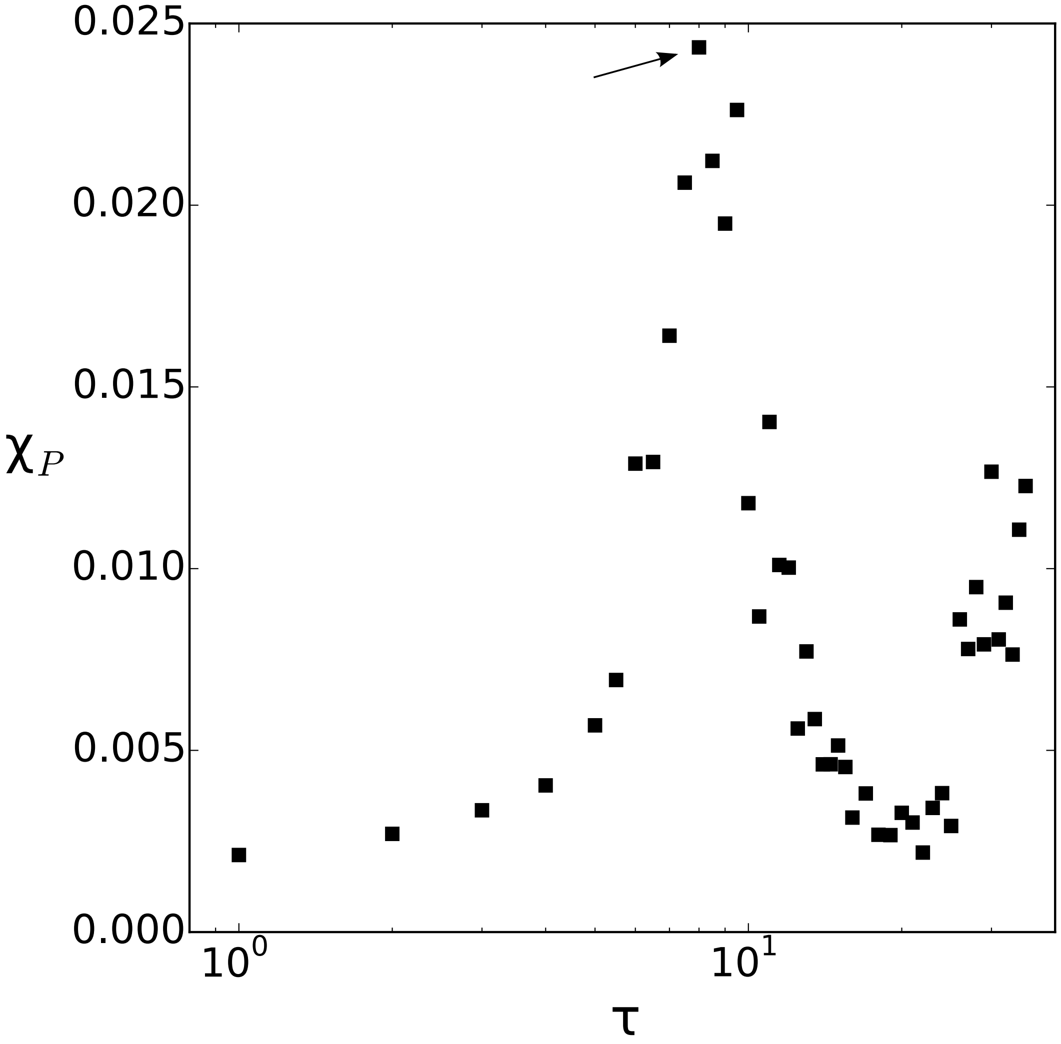

Figure 4.4: Relationship of variance of polarisation χ_P with time scale τ for a system of $N = 100$ particles at $\eta = 0.15$ and $\rho_{init} = 0.005$. Arrow indicates point of maximal variance at $\tau = 8.0$.

provides the information of a specified direction to turn, deviate in opacity from one another during convergence before settling to a similar value, although fluctuations around this mean value are still persistent. We should therefore observe a cohesive flock.

Figure 4.6 shows the variation of the final distance to first nearest neighbour, averaged over the ensemble of swarm members, with respect the time horizon τ. At low τ the value is large, indicating a low density flock. As τ increases the flock becomes more cohesive, until after $\tau = 6$ it gets larger again. This is quite surprising as it indicates a local maximum density in the region near the phase transition. The arrow indicates the point of maximal variance, as determined in figure 4.4. This lies close to this maximum density region. At very high τ the spatial extent of the group appears to collapse, which is also quite surprising. At this density, individuals would be overlapping as there is no explicit repulsion term in the model.

Now, if we look at figure 4.7 we can see the variation of the local opacities averaged over the ensemble of swarm members, both current and prospective, with respect the time horizon τ. At low τ, all are at low opacity, corresponding to flocks which have dissipated and failed to achieve their goal, as expected. Increasing τ produces local opacities that are close to the desired value of $^1/_2$, for both the current and prospective states. Interestingly, increasing τ further disrupts this initially for the current state, causing it to become more opaque, and further for the future states too. This divergence of visual states corresponds to the region of very high density observed above. It also corresponds to an ordered flock and to the area of high susceptibility in the ordered region. This presents a collapsed flock, trying to get back to the uncollapsed state, but failing as all individuals are in the same area and are heading to the same region of space, as they all compute it to be the least opaque (and thus the least dense).

This is somewhat analogous to the situation where, on a very busy road drivers will decide to look for an alternate route, only for that route to become more congested than the original as many drivers all think of the same strategy. In this model, it is a consequence of the homogeneity of the rule set, and interestingly this effect is therefore more present at low noise, and increasing the noise a little actually helps remedy the situation, although at the cost of a little order too.

Also of interest is a intermediate region of half opacity, where the system has succeeded in its goal, between τ of around 5 to 12. This region covers the whole phase transition region and some part of the ordered phase region too. This is remarkable, as this region of maximal response to external perturbation (say, a predator) corresponds to the region of consistency in visual input, where current

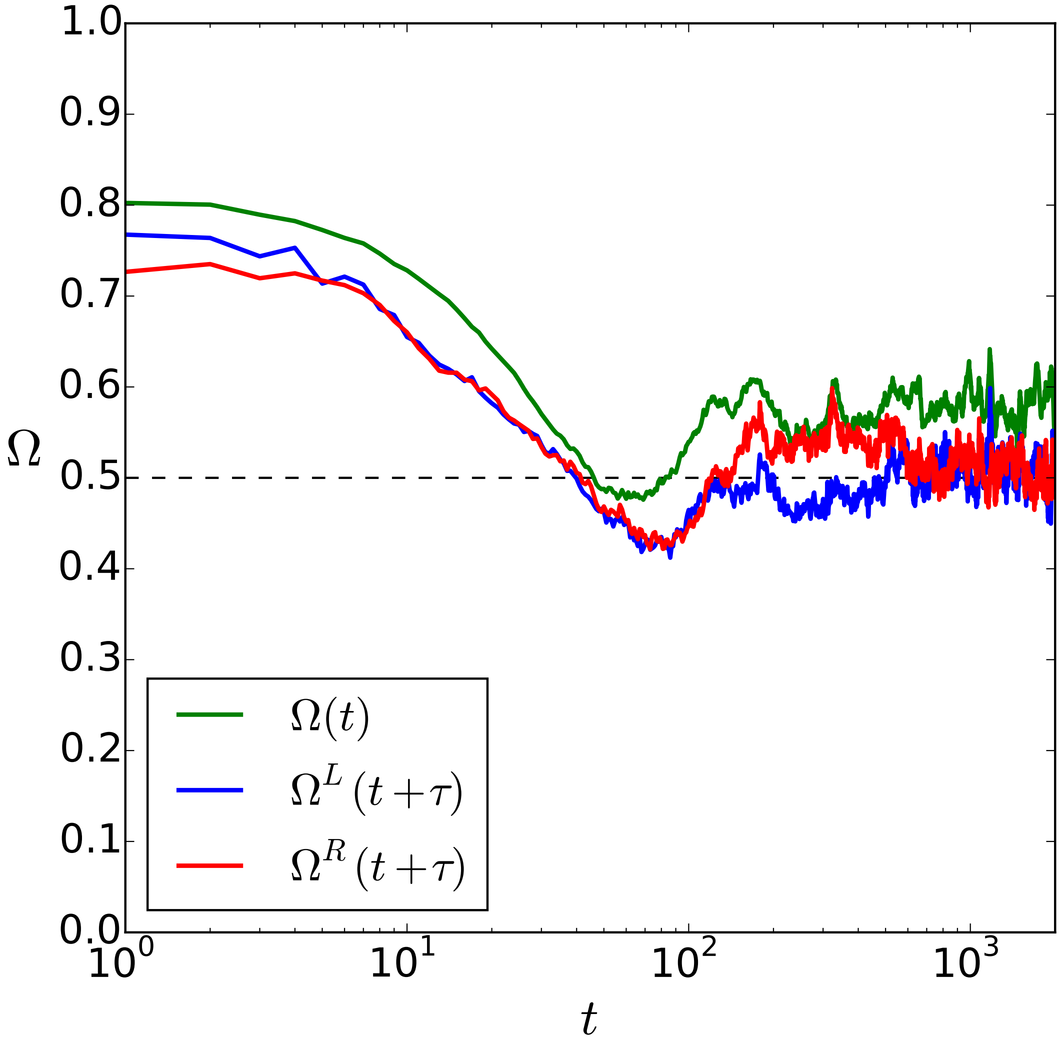

Figure 4.5: Convergence of ensemble-averaged current (black) and future L/R (red/green) local opacities with time horizon $\tau = 10$ over time for a system of $N = 100$ particles without noise $\eta = 0$ and $\rho_{init} = 0.001$. $\Omega^{L/R}(t + \tau)$ achieve desired opacity of $1/2$. Present local opacity converges, but settles on a slightly higher opacity (≈ 0.55).

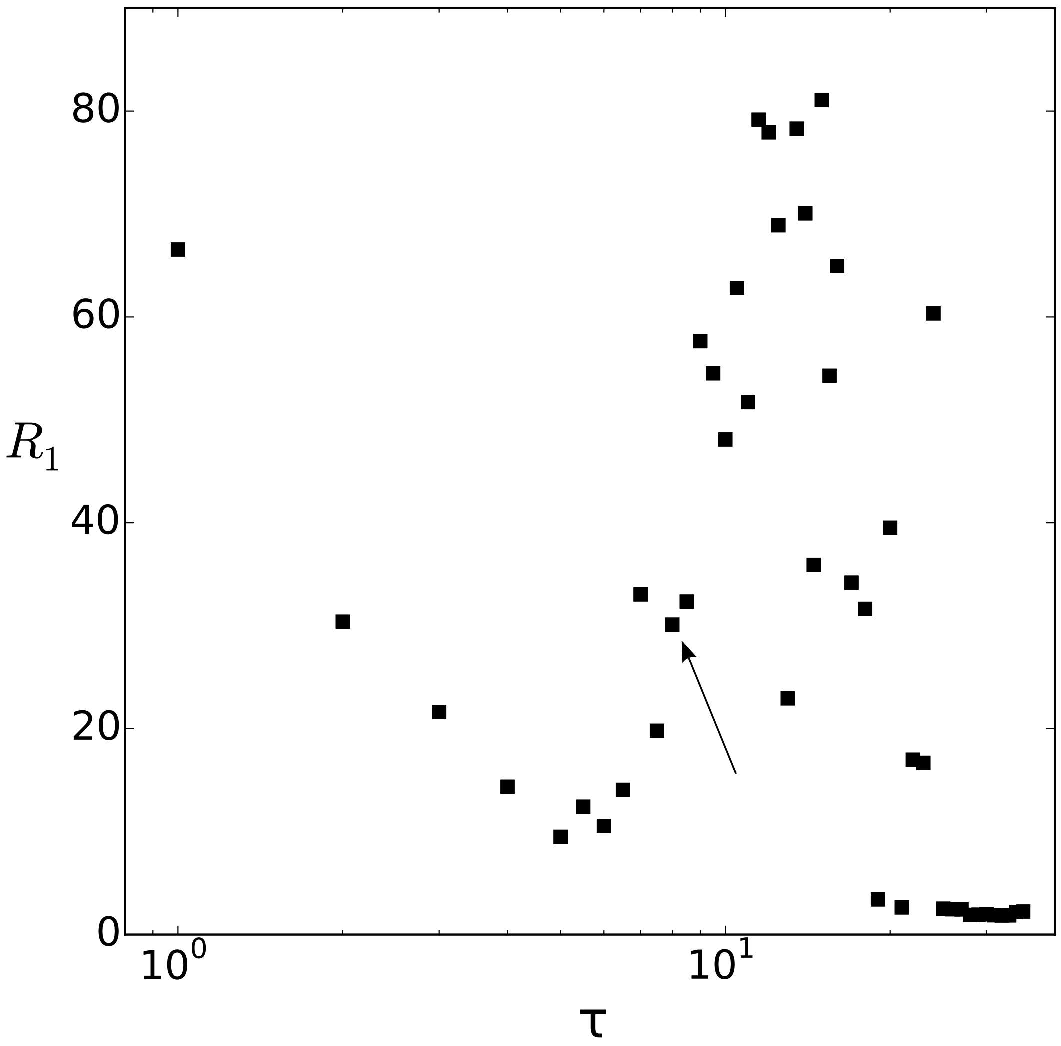

Figure 4.6: Variation of final nearest neighbour distance R_1 with time scale τ for a system of $N = 100$ particles at $\eta = 0.15$ and $\rho_{init} = 0.005$. Simulation performed over $T = 2.4 \cdot 10^4$ time steps. Group is unbounded at low τ before reaching a bound state near $\tau = 5.5$. Size then increases dramatically before becoming very dense at high τ. Arrow indicates point of maximal variance, as determined in figure 4.4.

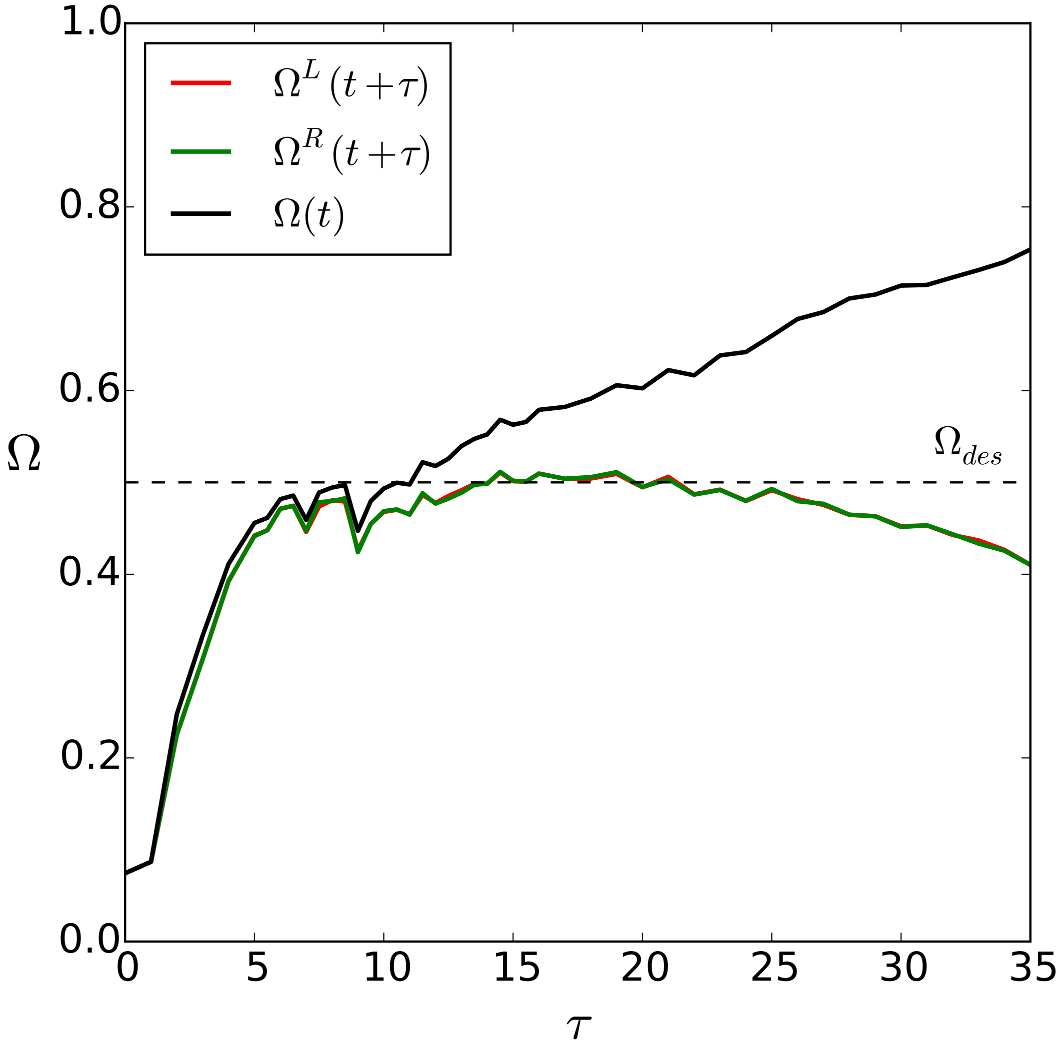

Figure 4.7: Variation of ensemble-averaged current (black) and future L/R (red/green) local opacities with time horizon τ for a system of $N = 100$ particles at $\eta = 0.15$ and $\rho_{init} = 0.005$. If τ is too low, they system cannot reach the desired opacity ($\Omega_{des} = 0.5$). Near and just above the transition inflection point opacities do attain Ω_{des}. Increasing τ past this is eventually detrimental to the convergence of opacity.

states are similar to future states (to zeroth order, i.e. opacity). This could be beneficial from a biological perspective as it could poise a flock to respond optimally to changes in its environment, but also be close to highly polarised and strongly cohesive states.

Finally, in order to gain some intuition about the simulated flocks we are producing, a snapshot of a typical system configuration is shown in figure 4.8, where an arrow corresponds to the heading of an individual and colour to the local opacity $\Omega_i(t)$ it observes at that snapshot in time t.

4.3.3 Robustness of the flock to noise

We have mentioned how in certain states, increasing the noise can actually help the system achieve its goal. This is fairly surprising as in many systems noise can be an inhibiting factor and is typically aimed to be minimised. It can however help a non-ergodic system cover more of its configuration space. It has also be shown that in certain artificial neural systems performance is improved by the effect of noise too [64, 92]. This is interesting as an analogy between systems with collective behaviour and cognitive science and decision making [24]. Therefore we need to consider the impact of noise on order for this system to understand how disruptive it is on the flocks ability to obtain global polarisation.

We begin with a flock which supports an ordered state and has consistency between its current and future visual states (corresponding to $\tau = 10$ for the $N = 100$ size system considered above). Figure 4.9 shows the impact of noise on the ability of the flock to form an ordered state. This puts to mind a continuous transition similar to the sort we have considered throughout this thesis. The monotone nature of the Binder's cumulant [8] across this region suggests this is indeed the case, however to say this definitively one would need to perform a finite size scaling analysis near the transition point. Therefore, it appears we can indeed give a small amount of noise to help the system achieve its goal for opacity and cohesion without sacrificing order.

4.3.4 Short-range correlations from long-range interactions

We have discussed how this model does not have any explicit inter-particle interaction that encourages alignment, however we have shown that alignment can indeed by generated by the requirement of marginal opacity. Therefore, it is of interest to see at what range this order is developed.

We begin by defining the velocity correlation function, similarly as to in

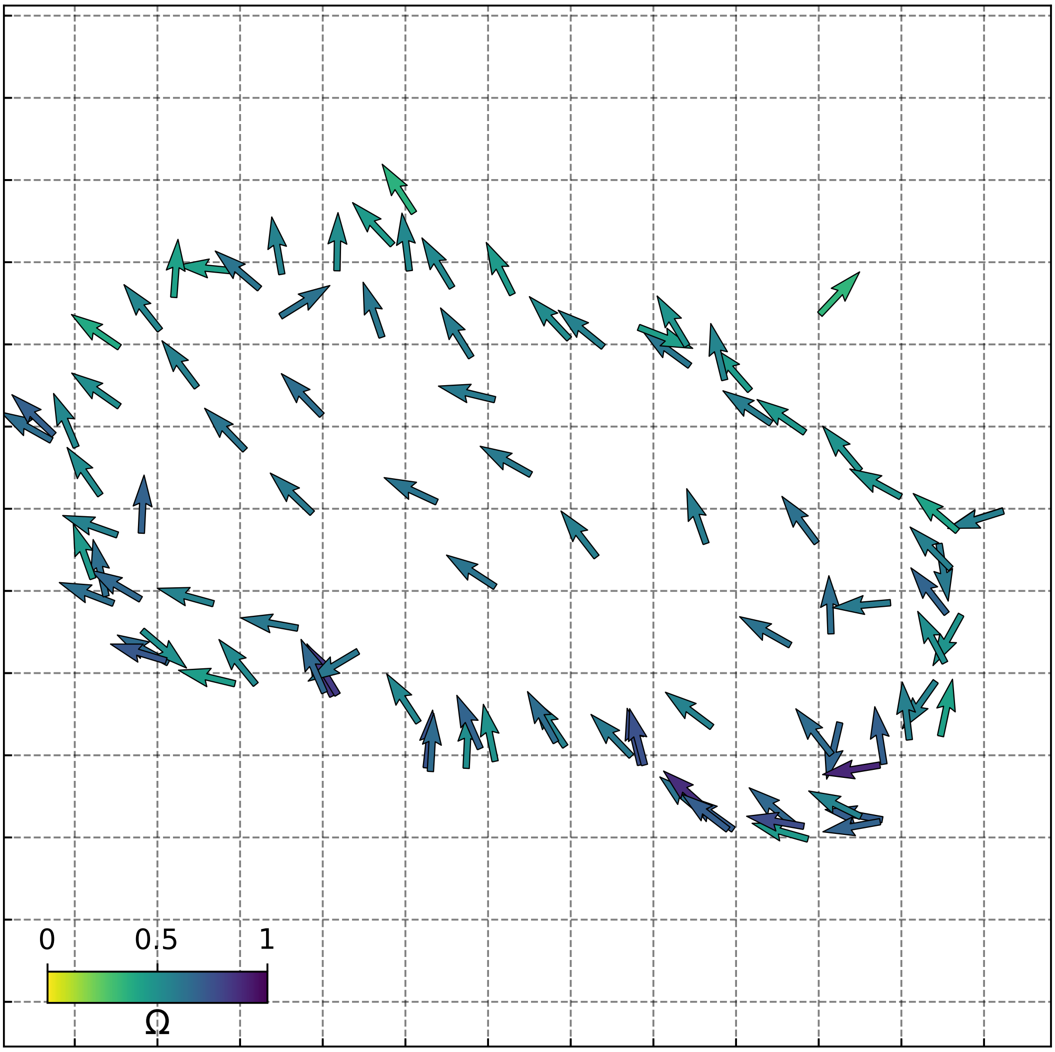

Figure 4.8: Snapshot of a system of $N = 100$ particles at $\eta = 0.15$ and $\rho_{init} = 0.005$ with time horizon $\tau = 10$. Ordered phase with $P(t) = 0.777$ (3 s.f.). Colour scheme denotes local opacity $\Omega(t)$ observed by each individual at this timestep t, which is close to marginal opacity ($= 0.5$) for most group members. Grid is of size 10 in each dimension.

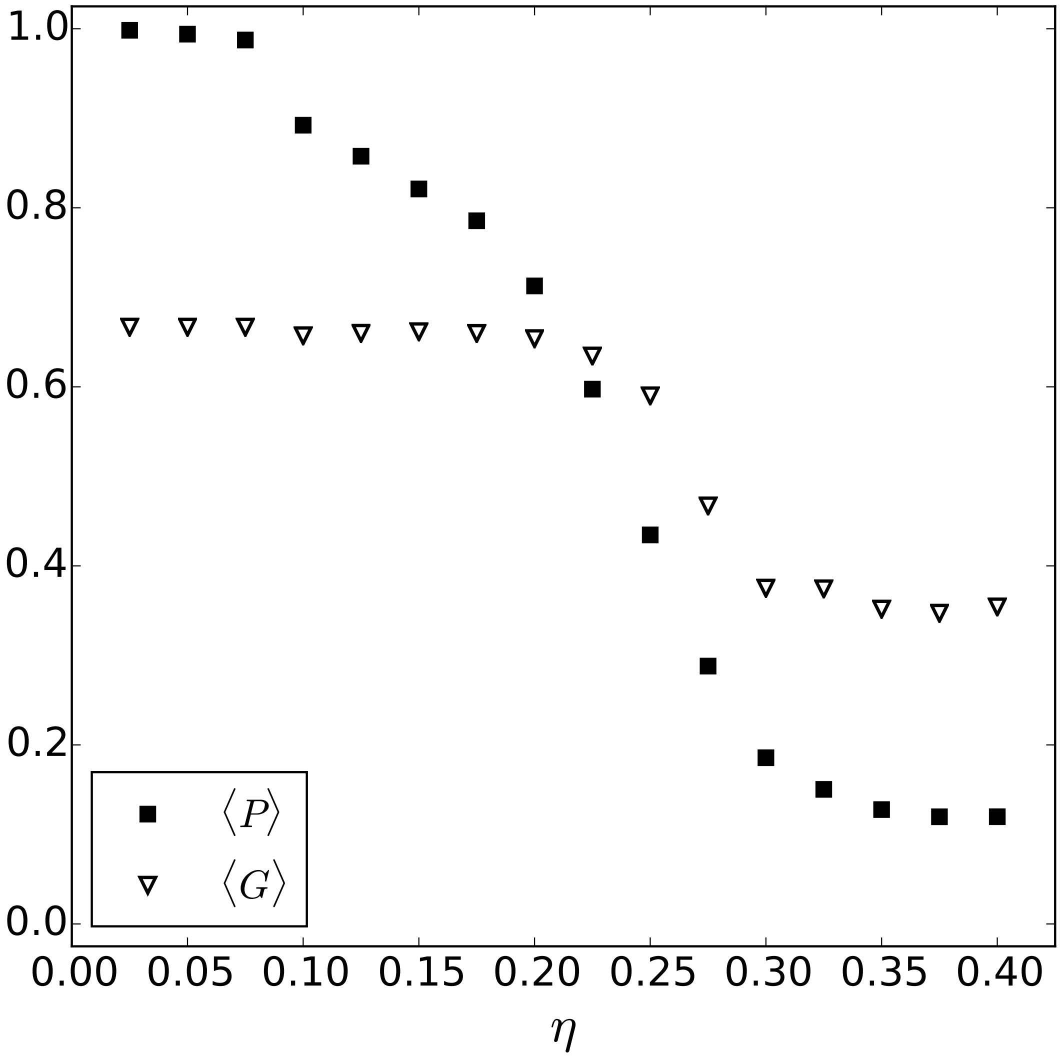

Figure 4.9: Impact of noise on group order. Time-averaged group order P and Binder's cumulant G with respect to noise strength η. Simulation for $N = 100$ at $\tau = 20$ with $\rho_{init} = 0.005$ for $T = 2.5 \cdot 10^4$ and $T_{eq} = T/2$.

Cavagna et al. [18], as:

$$C_v(r) = \frac{1}{c_0} \frac{\sum_{ij} \underline{v_i} \cdot \underline{v_j} \delta(r - r_{ij})}{\sum_{ij} \delta(r - r_{ij})} \tag{4.9}$$

where c_0 normalises the magnitude of $C_v(r)$ so that it has a value of 1 at $r = 0$ and c_0 makes $C_v(r)$ dimensionless, and the δ-function serves to pick out pairs of particles i and j at a specific separation of $r = r_{ij}$. The dot product between their velocities provides the magnitude of the term, which will be large when the pair is heading in a similar direction. We can use this measurement to determine the range of the order in the system.

Figure 4.10 highlights strong correlation in velocity between individuals. This is to be expected considering what we have covered so far, that global alignment is present in this system. We can also define the fluctuations in velocity as $\underline{u_i} = \underline{v_i} - \underline{V}$, where $V = \langle \underline{v_i} \rangle_{i \in S}$ is the group velocity. Note that here V is the same as polarisation due to the fixed movement speed of $v_0 = 1$ for each individual. The magnitude of these fluctuations is much smaller than the magnitude of the velocity (i.e. 1).

We can define a correlation function for velocity fluctuations $C_u(r)$ by replacing $\underline{v}$ with $\underline{u}$ in equation 4.9. The figure 4.10 also shows correlations in this quantity, whose crossing of the $C_u(r = r_c) = 0$ axis determines a correlation length r_c for the system. Defining correlation length in this way allows us to estimate the size of strongly correlated domains within the group [18]. Recalling that this model has no explicit aligning interaction rule placed on nearby individuals, it is notable that $r_c = 41.3$ (3 s.f.) is much larger than the particle size (particle radius $b = 1$ provides an appropriate length scale for the system), indeed it is on the order of half the linear size of the group (configuration shown in figure 4.8).

The structure of the velocity fluctuation correlation function looks very similar to those measured in wild flocks of Starlings [18]. Later theoretical work [6] derives a short-range topological interaction from those observations. However it appears that the explicitly non-short range, and potentially more biologically motivated, model can also produce similar correlations. However, a key finding of the empirical study, that this correlation length scales with the size of the flock, has not yet been produced with this model. This is due to technical limitations of increasing the system size N to an order of magnitude or more higher, in order to confirm their scale-free nature. However, work in this direction is underway and is a key avenue for future investigation.

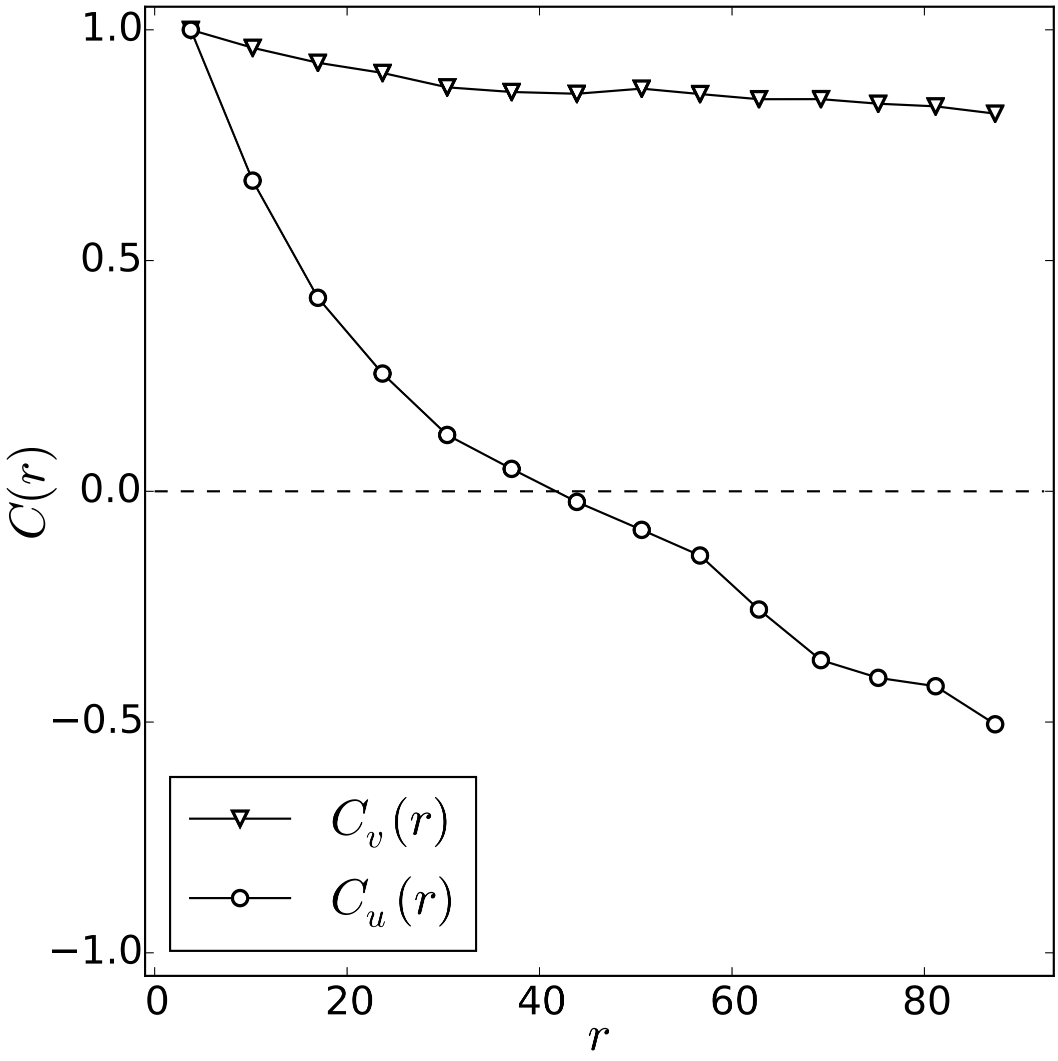

Figure 4.10: Velocity (down-triangles) and velocity fluctuation (circles) correlation functions normalised to the $C(r = 0)$ values. Simulation parameters: $N = 100$, $\eta = 0.15$, $\rho_{init} = 0.005$, $\tau = 10$. Distribution discretised into 15 bins. $C_v(r)$ decays very slowly: long range order present. Crossing point of $C_u(r)$ and $C(r) = 0$ (dotted line) indicates correlation length in system and is 41.3 (3 s.f.).

4.4 Conclusions

We have shown how the requirement of marginal opacity on the individual level can induce alignment and cohesion in flocks. To emphasise, these properties are emerging "for free" based on how an individual navigates its surroundings: there is explicitly no direct interaction between nearby particles, yet they can align and indeed the system correlates in velocity at short ranges. This is surprising and may give pause to question a common assumption that the strong short range correlations observed in real flocks [18] must arise due to a short range interaction. We have shown a counterexample to this, and one which is purely motivated by empirical observed phenomena, specifically the marginal opaque state of Starling swarms [76]. There are similar correlations observed in the model we have presented and this is purely generated by a *cognitive alignment*: two nearby particles undergo similar motion because they observe a similar visual input.

In terms of future direction, the existence of a "sweet-spot" near the transition to order with increased τ suggests a self-consistency condition with respect to the value of opacity (i.e. a condition which prevents the opacity observed in the current state from deviating too much from the anticipated future opacity) could help set its value *independent of choice of* N. This is particularly attractive as it could cause the correlation length, as determined via the velocity fluctuation correlation function, to scale with the size of the flock as observed in real flocks [18].

Additionally, we have discussed the complexity of the numerical implementation of the model presented. Dependent on the state of the group this can be $\mathcal{O}(N^3)$. We wish to make long simulations to improve our estimate of time-averaged quantities, but we also wish to simulate systems of many particles (large N). Not only is this because real-world bird flocks can have thousands of members, but as we have mentioned throughout this work, many of the observations around phase transitions only become visible for large N, going toward the thermodynamic limit ($N \to \infty$). The current state of our implementation can make statistically suitably long simulations for hundreds of individuals. Therefore, a prominent avenue for future investigation would be to improve the implementation. The most direct way to do this would be to parallelise the step of constructing the visual field, since this could be safely done for all individuals at the same time. This should reduce the complexity by a factor of N and should allow systems on the order of thousands of individuals to be investigated.

Chapter 5

Conclusions

In this thesis we have studied the concept of swarming – the collective behaviour of animal aggregations – to gain understanding of its features and mechanisms by simulating swarms using multi-particle models that specify a rule of interaction between the particles in the group, and comparing the resulting models to real-world observations and physical abilities of species to follow the defined rules. We have also introduced a model in which explicit inter-particle interactions are not required to produce collective motion. Such simulations aim to reproduce the main qualities of collective motion: cohesion and co-alignment, while using minimal rule sets, under the biologically motivated constraint of topological interactions.

Swarming behaviour is observed in many different species: birds, fishes and insects, here we focus mainly on bird (Starling) flocks, however our models can be adjusted and applied to other types of swarming. As it has been observed in recent empirical studies that interactions between members within flocks of birds do not have any specific length-scale (interaction radius), we chose to focus on metric-free, topological models of swarming. Topological interactions are important and provide an interesting theoretical challenge due to their inherent lack of a length scale.

We have proposed two topological models of swarming that use topological interactions between particles, which are based on Voronoi tessellation of the group of particles, and the last one on the visual field of the individual.

While the metric-free paradigm grants the absence of group fragmentation as interactions occur at all length scales, cohesion is not guaranteed and dissipation will typically occur. Previous works have shown that bounding metric free models in free-space is challenging. We have proposed a way of achieving aligned and cohesive flocks with topological interactions by introducing temporal information into the interaction between individuals in the form of neighbour anticipation. An individual moves to where it expects its neighbour to be at some point in the future: aligning with its presumed target in space rather that its specific orientation. This homogenous interaction scheme for all particles in the flock takes advantage of the underlying geometric construction defining interacting neighbours to establish the strength and direction of the effective bounding forces.

Another aspect of real world flocks that is challenging to reproduce in simulations of topological models is the density distribution of birds in the flock. For example, for flocks of Starlings a non-homogeneous density variation across the group with a higher density at the border were reported. Existing works either support a zero density steady-state, or produce density distributions that are rather different to the ones observed in nature. We have studied density regulation across flocks of birds via a a fully topological three-dimensional model with a tunable motional bias throughout the swarm and not just on its surface. We have shown that it is able to support behaviour consistent with the empirical observations. We have also described a way that could be used by a member of a flock to determine its depth within the flock via the observed anisotropy of its visual field and discussed its significance.

Having explored group density and density distributions, we considered empirical observations of real-world starling flocks, which appear to avoid states of too high or too low density, termed a “marginally opaque” state. We related the notion of opacity to the visual field of the individual, the portion of field of view that is occupied by other members of the group. We studied the hypothesis that individuals in the flock are trying to reach the state of marginal opacity, i.e. seeing about half of their visual field occupied by other agents. Our results showed that seeking marginal opacity is sufficient to produce alignment in simulated swarms, as when nearby particles have a similar visual field they make similar decisions. This manifests alignment in neighbour headings as a consequence of a “cognitive alignment”. We also studied the correlations in velocity and velocity perturbations between pairs of particles and found a qualitatively similar form to those reported in literature for flocks of Starlings.

This suggests that a future direction for investigation is a more quantitative comparison with real flocks in order to query whether the interaction between birds can be attributed solely to explicit short-range co-aligning interactions, or whether this longer-range *implicitly* locally aligning effect could be involved. Furthermore, it would be of interest to consider whether the implicit alignment effect can occur for biological systems with other types of information input; many systems such as birds and humans use vision as we have studied here, however there are a diverse choice of other biological information streams: many insects use sound to evaluate and respond to their environment, and smell can contain a great deal of information for animals with specialised sensory equipment. If so, it would be interesting to see if these systems could exhibit similar behaviours, such as strong linear response and greater than expected correlation lengths.

Bibliography

[1] Alessandro Attanasi, Andrea Cavagna, Lorenzo Del Castello, Irene Giardina, Tomas S Grigera, Asja Jelić, Stefania Melillo, Leonardo Parisi, Oliver Pohl, Edward Shen, et al. Information transfer and behavioural inertia in starling flocks. *Nature Physics*, 10(9):691, 2014.

[2] Alessandro Attanasi, Andrea Cavagna, Lorenzo Del Castello, Irene Giardina, Stefania Melillo, Leonardo Parisi, Oliver Pohl, Bruno Rossaro, Edward Shen, Edmondo Silvestri, et al. Collective behaviour without collective order in wild swarms of midges. *PLoS Computational Biology*, 10(7):e1003697, 2014.

[3] Michele Ballerini, Nicola Cabibbo, Raphael Candelier, Andrea Cavagna, Evaristo Cisbani, Irene Giardina, Vivien Lecomte, Alberto Orlandi, Giorgio Parisi, Andrea Procaccini, et al. Interaction ruling animal collective behavior depends on topological rather than metric distance: Evidence from a field study. *Proceedings of the National Academy of Sciences*, 105(4):1232–1237, 2008.

[4] Michele Ballerini, Nicola Cabibbo, Raphael Candelier, Andrea Cavagna, Evaristo Cisbani, Irene Giardina, Alberto Orlandi, Giorgio Parisi, Andrea Procaccini, Massimiliano Viale, et al. Empirical investigation of starling flocks: a benchmark study in collective animal behaviour. *Animal Behaviour*, 76(1): 201–215, 2008.

[5] Sepideh Bazazi, Jerome Buhl, Joseph J Hale, Michael L Anstey, Gregory A Sword, Stephen J Simpson, and Iain D Couzin. Collective motion and cannibalism in locust migratory bands. *Current Biology*, 18(10):735–739, 2008.

[6] William Bialek, Andrea Cavagna, Irene Giardina, Thierry Mora, Edmondo Silvestri, Massimiliano Viale, and Aleksandra M Walczak. Statistical mechanics for natural flocks of birds. *Proceedings of the National Academy of Sciences*, 2012.

[7] Kurt Binder. Finite size scaling analysis of ising model block distribution functions. *Zeitschrift für Physik B Condensed Matter*, 43(2):119–140, 1981.

[8] Kurt Binder and Dieter W Heerman. *Monte Carlo Simulation in Statistical Physics*. Springer Berlin Heidelberg, 1988.

[9] Bert Blocken, Thijs van Druenen, Yasin Toparlar, Fabio Malizia, Paul Mannion, Thomas Andrianne, Thierry Marchal, Geert-Jan Maas, and Jan Diepens. Aerodynamic drag in cycling pelotons: New insights by CFD simulation and wind tunnel testing. *Journal of Wind Engineering and Industrial Aerodynamics*, 179:319–337, 2018.

[10] John Buck. Synchronous rhythmic flashing of fireflies. ii. *Quarterly Review of Biology*, pages 265–289, 1988.

[11] Jerome Buhl, David JT Sumpter, Iain D Couzin, Joe J Hale, Emma Despland, Edgar R Miller, and Steve J Simpson. From disorder to order in marching locusts. *Science*, 312(5778):1402–1406, 2006.

[12] Scott Camazine. *Self-Organization in Biological Systems*. Princeton University Press, 2003.

[13] José A Carrillo, Young-Pil Choi, and Sergio P Perez. A review on attractive–repulsive hydrodynamics for consensus in collective behavior. In *Active Particles, Volume 1*, pages 259–298. Springer, 2017.

[14] José Antonio Carrillo, Young-Pil Choi, and Maxime Hauray. The derivation of swarming models: mean-field limit and wasserstein distances. *Collective Dynamics from Bacteria to Crowds*, 553:1–46.

[15] Jean-Baptiste Caussin and Denis Bartolo. Braiding a flock: winding statistics of interacting flying spins. *Physical Review Letters*, 114(25):258101, 2015.

[16] Andrea Cavagna, Irene Giardina, Alberto Orlandi, Giorgio Parisi, and Andrea Procaccini. The starflag handbook on collective animal behaviour: 2. three-dimensional analysis. *Animal Behaviour*, 76(1):237–248, 2008.

[17] Andrea Cavagna, Alessio Cimarelli, Irene Giardina, Giorgio Parisi, Raffaele Santagati, Fabio Stefanini, and Raffaele Tavarone. From empirical data to inter-individual interactions: unveiling the rules of collective animal behavior. *Mathematical Models and Methods in Applied Sciences*, 20(supp01):1491–1510, 2010.

[18] Andrea Cavagna, Alessio Cimarelli, Irene Giardina, Giorgio Parisi, Raffaele Santagati, Fabio Stefanini, and Massimiliano Viale. Scale-free correlations in starling flocks. *Proceedings of the National Academy of Sciences*, 107(26): 11865–11870, 2010.

[19] Andrea Cavagna, Irene Giardina, Francesco Ginelli, Thierry Mora, Duccio Piovani, Raffaele Tavarone, and Aleksandra M Walczak. Dynamical maximum entropy approach to flocking. *Physical Review E*, 89(4):042707, 2014.

[20] Andrea Cavagna, Irene Giardina, Tomas S Grigera, Asja Jelic, Dov Levine, Sriram Ramaswamy, and Massimiliano Viale. Silent flocks: constraints on signal propagation across biological groups. *Physical Review Letters*, 114(21): 218101, 2015.

[21] Paul M Chaikin, Tom C Lubensky, and Thomas A Witten. *Principles of Condensed Matter Physics*, volume 1. Cambridge University Press, 1995.

[22] Hugues Chaté, Francesco Ginelli, Guillaume Grégoire, and Franck Raynaud. Collective motion of self-propelled particles interacting without cohesion. *Physical Review E*, 77(4):046113, 2008.

[23] Wikimedia Commons. Main page — wikimedia commons, the free media repository, 2018. URL `https://commons.wikimedia.org/w/index.php?title=Main_Page`.

[24] Iain D Couzin. Collective cognition in animal groups. *Trends in Cognitive Sciences*, 13(1):36–43, 2009.

[25] Iain D Couzin and Jens Krause. Self-organization and collective behavior in vertebrates. *Advances in the Study of Behavior*, 32(1), 2003.

[26] JA Downes. The swarming and mating flight of diptera. *Annual Review of Entomology*, 14(1):271–298, 1969.

[27] Herbert Edelsbrunner and Ernst P Mücke. Three-dimensional alpha shapes. *ACM Transactions on Graphics (TOG)*, 13(1):43–72, 1994.

[28] John T Emlen. Flocking behavior in birds. *The Auk*, 69(2):160–170, 1952.

[29] Illés Farkas, Dirk Helbing, and Tamás Vicsek. Social behaviour: Mexican waves in an excitable medium. *Nature*, 419(6903):131–132, 2002.

[30] Christopher Feare. *The Starling.* Oxford University Press, 1984.

[31] Étienne Fodor, Cesare Nardini, Michael E Cates, Julien Tailleur, Paolo Visco, and Frédéric van Wijland. How far from equilibrium is active matter? *Physical Review Letters*, 117(3):038103, 2016.

[32] Irene Giardina. Collective behavior in animal groups: theoretical models and empirical studies. *HFSP Journal*, 2(4):205–219, 2008.

[33] Francesco Ginelli. The physics of the Vicsek model. *The European Physical Journal Special Topics*, 225(11-12):2099–2117, 2016.

[34] Francesco Ginelli and Hugues Chaté. Relevance of metric-free interactions in flocking phenomena. *Physical Review Letters*, 105(16):168103, 2010.

[35] Anne E Goodenough, Natasha Little, William S Carpenter, and Adam G Hart. Birds of a feather flock together: Insights into starling murmuration behaviour revealed using citizen science. *PloS One*, 12(6):e0179277, 2017.

[36] Guillaume Grégoire and Hugues Chaté. Onset of collective and cohesive motion. *Physical Review Letters*, 92(2):025702, 2004.

[37] Shay Gueron, Simon A Levin, and Daniel I Rubenstein. The dynamics of herds: from individuals to aggregations. *Journal of Theoretical Biology*, 182 (1):85–98, 1996.

[38] William D Hamilton. Geometry for the selfish herd. *Journal of Theoretical Biology*, 31(2):295–311, 1971.

[39] Nils Olav Handegard, Kevin M Boswell, Christos C Ioannou, Simon P Leblanc, Dag B Tjøstheim, and Iain D Couzin. The dynamics of coordinated group hunting and collective information transfer among schooling prey. *Current Biology*, 22(13):1213–1217, 2012.

[40] Dirk Helbing. Self-organization in pedestrian crowds. In *Social Self-Organization*, pages 71–99. Springer, 2012.

[41] Dirk Helbing and Péter Molnár. Social force model for pedestrian dynamics. *Physical Review E*, 51:4282–4286, May 1995.

[42] Dirk Helbing, Peter Molnar, Illes J Farkas, and Kai Bolay. Self-organizing pedestrian movement. *Environment and Planning B*, 28(3):361–384, 2001.

[43] Charlotte K Hemelrijk and Hanno Hildenbrandt. Self-organized shape and frontal density of fish schools. *Ethology*, 114(3):245–254, 2008.

[44] Charlotte K Hemelrijk, Hanno Hildenbrandt, Jose Reinders, and Eize J Stamhuis. Emergence of oblong school shape: models and empirical data of fish. *Ethology*, 116(11):1099–1112, 2010.

[45] CK Hemelrijk, DAP Reid, H Hildenbrandt, and JT Padding. The increased efficiency of fish swimming in a school. *Fish and Fisheries*, 16(3):511–521, 2015.

[46] Christos C Ioannou, Vishwesha Guttal, and Iain D Couzin. Predatory fish select for coordinated collective motion in virtual prey. *Science*, 337(6099): 1212–1215, 2012.

[47] Yael Katz, Kolbjørn Tunstrøm, Christos C Ioannou, Cristián Huepe, and Iain D Couzin. Inferring the structure and dynamics of interactions in schooling fish. *Proceedings of the National Academy of Sciences*, 108(46):18720–18725, 2011.

[48] Douglas H Kelley and Nicholas T Ouellette. Emergent dynamics of laboratory insect swarms. *Scientific Reports*, 3:1073, 2013.

[49] Andrew J King and David JT Sumpter. Murmurations. *Current Biology*, 22 (4):112–114, 2012.

[50] David C Krakauer. Groups confuse predators by exploiting perceptual bottlenecks: a connectionist model of the confusion effect. *Behavioral Ecology and Sociobiology*, 36(6):421–429, 1995.

[51] J Krause, D Hoare, S Krause, CK Hemelrijk, and DI Rubenstein. Leadership in fish shoals. *Fish and Fisheries*, 1(1):82–89, 2000.

[52] Hanspeter Kunz and Charlotte K Hemelrijk. Artificial fish schools: collective effects of school size, body size, and body form. *Artificial Life*, 9(3):237–253, 2003.

[53] Laurie Landeau and John Terborgh. Oddity and the confusion effect in predation. *Animal Behaviour*, 34(5):1372–1380, 1986.

[54] Der-Tsai Lee and Bruce J Schachter. Two algorithms for constructing a delaunay triangulation. *International Journal of Computer & Information Sciences*, 9(3):219–242, 1980.

[55] Jason M Lewis and Matthew S Turner. (2014). Topological models of swarming (Unpublished Master's dissertation). University of Warwick, Coventry, United Kingdom.

[56] Jason M Lewis and Matthew S Turner. Density distributions and depth in flocks. *Journal of Physics D: Applied Physics*, 50(49):4003, 2017.

[57] Steven L Lima. Back to the basics of anti-predatory vigilance: the group-size effect. *Animal Behaviour*, 49(1):11–20, 1995.

[58] PBS Lissaman and Carl A Shollenberger. Formation flight of birds. *Science*, 168(3934):1003–1005, 1970.

[59] Ryan Lukeman, Yue-Xian Li, and Leah Edelstein-Keshet. Inferring individual rules from collective behavior. *Proceedings of the National Academy of Sciences*, 107(28):12576–12580, 2010.

[60] JL Meijering. Interface area, edge length, and number of vertices in crystal aggregates with random nucleation. *Philips Research Reports*, 8:270–290, 1953.

[61] Roger E Miles. On the homogeneous planar poisson point process. *Mathematical Biosciences*, 6:85–127, 1970.

[62] Adam M Miller. *Simulating Collective Motion from Particles to Birds*. PhD thesis, University of Warwick, 2015.

[63] Michael S Mooring and Benjamin L Hart. Animal grouping for protection from parasites: selfish herd and encounter-dilution effects. *Behaviour*, 123(3): 173–193, 1992.

[64] Arvind Neelakantan, Luke Vilnis, Quoc V Le, Ilya Sutskever, Lukasz Kaiser, Karol Kurach, and James Martens. Adding gradient noise improves learning for very deep networks. *arXiv preprint arXiv:1511.06807*, 2015.

[65] Gregoire Nicolis and Ilya Prigogine. *Self-Organization in Nonequilibrium Systems*, volume 191977. Wiley, New York, 1977.

[66] Nikolai Nikola, Alexandre P Solon, Yariv Kafri, Mehran Kardar, Julien Tailleur, and Raphaël Voituriez. Active particles with soft and curved walls: Equation of state, ratchets, and instabilities. *Physical Review Letters*, 117(9): 098001, 2016.

[67] Géza Ódor. Universality classes in nonequilibrium lattice systems. *Reviews of Modern Physics*, 76(3):663, 2004.

[68] Atsuyuki Okabe, Barry Boots, Kokichi Sugihara, and Sung Nok Chiu. *Spatial Tessellations: Concepts and Applications of Voronoi Diagrams*, volume 501. John Wiley & Sons, 2009.

[69] Akira Okubo. Dynamical aspects of animal grouping: swarms, schools, flocks, and herds. *Advances in Biophysics*, 22:1–94, 1986.

[70] Randal S Olson, Arend Hintze, Fred C Dyer, David B Knoester, and Christoph Adami. Predator confusion is sufficient to evolve swarming behaviour. *Journal of The Royal Society Interface*, 10(85):20130305, 2013.

[71] Julia K Parrish and Leah Edelstein-Keshet. Complexity, pattern, and evolutionary trade-offs in animal aggregation. *Science*, 284(5411):99–101, 1999.

[72] Brian L Partridge, Tony Pitcher, J Michael Cullen, and John Wilson. The three-dimensional structure of fish schools. *Behavioral Ecology and Sociobiology*, 6(4):277–288, 1980.

[73] Brian L Partridge, Jonas Johansson, and John Kalish. The structure of schools of giant bluefin tuna in cape cod bay. *Environmental Biology of Fishes*, 9(3-4): 253–262, 1983.

[74] Daniel JG Pearce. *Swarming.* PhD thesis, University of Warwick, 2014.

[75] Daniel JG Pearce and Matthew S Turner. Density regulation in strictly metric-free swarms. *New Journal of Physics*, 16(8):082002, 2014.

[76] Daniel JG Pearce, Adam M Miller, George Rowlands, and Matthew S Turner. Role of projection in the control of bird flocks. *Proceedings of the National Academy of Sciences*, 111(29):10422–10426, 2014.

[77] Anton Peshkov, Sandrine Ngo, Eric Bertin, Hugues Chaté, and Francesco Ginelli. Continuous theory of active matter systems with metric-free interactions. *Physical Review Letters*, 109(9):098101, 2012.

[78] Anton Peshkov, Eric Bertin, Francesco Ginelli, and Hugues Chaté. Boltzmann-ginzburg-landau approach for continuous descriptions of generic vicsek-like models. *The European Physical Journal Special Topics*, 223(7):1315–1344, 2014.

[79] Tony J Pitcher. Heuristic definitions of fish shoaling behaviour. *Animal Behaviour*, 31(2):611–613, 1983.

[80] Tony J Pitcher. Functions of shoaling behaviour in teleosts. In *The Behaviour of Teleost Fishes*, pages 294–337. Springer, 1986.

[81] Erick Martins Ratamero. Modelling peloton dynamics in competitive cycling: a quantitative approach. In *International Congress on Sports Science Research and Technology Support*, pages 42–56. Springer, 2013.

[82] AM Reynolds. Langevin dynamics encapsulate the microscopic and emergent macroscopic properties of midge swarms. *Journal of The Royal Society Interface*, 15(138):20170806, 2018.

[83] Andrew M Reynolds, Michael Sinhuber, and Nicholas T Ouellette. Are midge swarms bound together by an effective velocity-dependent gravity? *The European Physical Journal E*, 40(4):46, 2017.

[84] Craig W Reynolds. Flocks, herds and schools: A distributed behavioral model. *ACM Siggraph Computer Graphics*, 21(4):25–34, 1987.

[85] Gilbert Roberts. Why individual vigilance declines as group size increases. *Animal Behaviour*, 51(5):1077–1086, 1996.

[86] Jesse L Silverberg, Matthew Bierbaum, James P Sethna, and Itai Cohen. Collective motion of humans in mosh and circle pits at heavy metal concerts. *Physical Review Letters*, 110(22):228701, 2013.

[87] Alexandre P Solon, Y Fily, Aparna Baskaran, Mickael E Cates, Y Kafri, M Kardar, and J Tailleur. Pressure is not a state function for generic active fluids. *Nature Physics*, 11(8):673, 2015.

[88] Alexandre P Solon, Joakim Stenhammar, Raphael Wittkowski, Mehran Kardar, Yariv Kafri, Michael E Cates, and Julien Tailleur. Pressure and phase equilibria in interacting active brownian spheres. *Physical Review Letters*, 114 (19):198301, 2015.

[89] James C Spall. Multivariate stochastic approximation using a simultaneous perturbation gradient approximation. *IEEE Transactions on Automatic Control*, 37(3):332–341, 1992.

[90] James C Spall. Implementation of the simultaneous perturbation algorithm for stochastic optimization. *IEEE Transactions on Aerospace and Electronic Systems*, 34(3):817–823, 1998.

[91] James C Spall. *Introduction to Stochastic Search and Optimization: Estimation, Simulation, and Control*, volume 65. John Wiley & Sons, 2005.

[92] Nitish Srivastava, Geoffrey Hinton, Alex Krizhevsky, Ilya Sutskever, and Ruslan Salakhutdinov. Dropout: a simple way to prevent neural networks from overfitting. *The Journal of Machine Learning Research*, 15(1):1929–1958, 2014.

[93] Ariana Strandburg-Peshkin, Colin R Twomey, Nikolai WF Bode, Albert B Kao, Yael Katz, Christos C Ioannou, Sara B Rosenthal, Colin J Torney, Hai Shan Wu, Simon A Levin, et al. Visual sensory networks and effective information transfer in animal groups. *Current Biology*, 23(17):R709–R711, 2013.

[94] Robert T Sullivan. Insect swarming and mating. *The Florida Entomologist*, 64(1):44–65, 1981.

[95] David JT Sumpter. The principles of collective animal behaviour. *Philosophical Transactions of the Royal Society B: Biological Sciences*, 361(1465):5–22, 2006.

[96] Masaharu Tanemura. Statistical distributions of poisson voronoi cells in two and three dimensions. *FORMA-TOKYO-*, 18(4):221–247, 2003.

[97] John Toner and Yuhai Tu. Flocks, herds, and schools: A quantitative theory of flocking. *Physical Review E*, 58(4):4828, 1998.

[98] Chad M Topaz, Andrew J Bernoff, Sheldon Logan, and Wyatt Toolson. A model for rolling swarms of locusts. *The European Physical Journal Special Topics*, 157(1):93–109, 2008.

[99] Chad M Topaz, Maria R D'Orsogna, Leah Edelstein-Keshet, and Andrew J Bernoff. Locust dynamics: behavioral phase change and swarming. *PLoS Computational Biology*, 8(8):e1002642, 2012.

[100] George F Turner and Tony J Pitcher. Attack abatement: a model for group protection by combined avoidance and dilution. *The American Naturalist*, 128 (2):228–240, 1986.

[101] Siddhartha Verma, Guido Novati, and Petros Koumoutsakos. Efficient collective swimming by harnessing vortices through deep reinforcement learning. *Proceedings of the National Academy of Sciences*, page 201800923, 2018.

[102] Tamás Vicsek and Anna Zafeiris. Collective motion. *Physics Reports*, 517(3): 71–140, 2012.

[103] Tamás Vicsek, András Czirók, Eshel Ben-Jacob, Inon Cohen, and Ofer Shochet. Novel type of phase transition in a system of self-driven particles. *Physical Review Letters*, 75(6):1226, 1995.

[104] Ashley JW Ward, David JT Sumpter, Iain D Couzin, Paul JB Hart, and Jens Krause. Quorum decision-making facilitates information transfer in fish shoals. *Proceedings of the National Academy of Sciences*, 105(19):6948–6953, 2008.

[105] Aaron Waters, François Blanchette, and Arnold D Kim. Modeling huddling penguins. *PLoS One*, 7(11):e50277, 2012.

[106] George F Young, Luca Scardovi, Andrea Cavagna, Irene Giardina, and Naomi E Leonard. Starling flock networks manage uncertainty in consensus at low cost. *PLoS Computational Biology*, 9(1):e1002894, 2013.

[107] B Yuval and A Bouskila. Temporal dynamics of mating and predation in mosquito swarms. *Oecologia*, 95(1):65–69, 1993.

[108] CGAL, Computational Geometry Algorithms Library. https://www.cgal.org/.